The oxidation of iron-chromium alloys at 400-600 degrees C in CO2-based gas.

Cox, M. G. C.

Award date:
1975

Awarding institution:
University of Bath

THE OXIDATION OF IRON-CHROMIUM ALLOYS AT 400-600°C IN CO_2-BASED GAS

submitted by

M.G.C. Cox, B.Sc.

for the degree of PhD

of the University of Bath

1975

M. Cox.

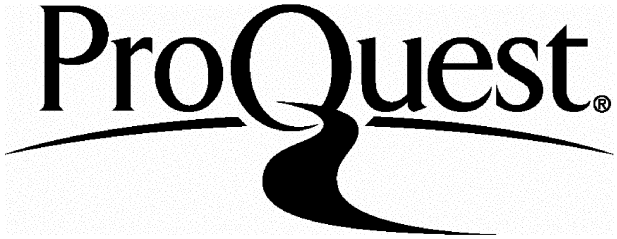

CONTENTS

ACKNOWLEDGMENTS

The author would like to thank the following: Dr. V.D. Scott and Dr. B. McEnaney for their encouragement and supervision throughout the project; the staff of Materials Division, Berkeley Nuclear Laboratories, particularly Dr. W.H. Whitlow, for their help and comments at various stages of the work; Mr. G. Love, Mr. R. Perrott and Mr. B. Chapman for their assistance with the electron optical and X-ray studies. The following organisations are also gratefully acknowledged for providing instrument facilities: Berkeley Nuclear Laboratories (use of Microscan 5, Stereoscan and 1 MeV electron microscope); Cardiff University (Stereoscan and electron probe microanalysis facilities); the Royal Military College of Science and Technology (use of Stereoscan); University of Manchester (use of EMMA 4 analytical electron microscope) and JEOL Ltd. (for use of electron probe microanalysis facilities). I should like to thank Mrs. H. Gott for her patience in typing this thesis.

The work was carried out in the School of Materials Science, the University of Bath, and I am indebted to the Head of School, Professor C.R. Tottle for use of the facilities of the department.

SUMMARY

The oxidation behaviour of a series of iron-chromium binary alloys containing 5%, 9%, 12%, 15% and 20% chromium at 400-600°C has been studied in CO_2-1% CO gas mixtures.

The experimental approach has involved kinetic studies using a microgravimetric method together with detailed characterisation of the oxidation products using optical, X-ray and electron optical techniques.

Several oxides are formed during the initial stages of oxidation. The nature of the oxidation product is shown to depend on both the crystallographic orientation and the initial composition of the substrate. These effects are explained by considering the maximum solubility of chromium in different oxide phases together with interfacial and strain energy factors.

The kinetics of oxidation together with micrographic observations clearly indicate that as the oxidation proceeds spinel oxide, M_3O_4, nucleates at various sites on the substrate surface. Such sites are associated with asperities on the surface. The spinel nuclei grow both laterally and vertically until they impinge and coalesce. The scale subsequently thickens according to a parabolic rate law. Examination of scales reveals a duplex structure. This is interpreted in terms of an outward diffusion of cations together with simultaneous growth of an inner layer in the space created by the outward movement

of metal. Both layers are porous and hence provide a route for gas phase transport of oxidant to support the growth of the inner layer. A series, regularly spaced, of lamellar voids form in the inner layer under certain conditions. This is believed to be associated with a cyclic vacancy condensation process and it is shown that the spacing between lamellar voids is consistent with such considerations. Enrichment of the inner layer in chromium also occurs and a model is proposed to explain this segregation effect based on an analysis of the possible diffusion path networks in close packed oxides.

CHAPTER 1

1.1 Introduction

With the possible exception of gold all metals are thermodynamically unstable with respect to their oxides in air at room temperature. The apparent stability exhibited by most common metals is in reality exceedingly slow oxidation due to a barrier layer of oxidation product on the metal surface which separates the reactants, metal and oxidant gas . The rate of reaction is thus controlled by the rate at which the oxidant and the metal diffuse through this layer of oxide. As the temperature of the system is raised the effectiveness of the barrier layer decreases due to the increase in the rate of diffusion of the reactants in the barrier film.

In recent years there has been an increasing demand for corrosion-resistant alloys which may be used at higher temperatures and in aggressive environments. This is particularly apparent in the electricity generating industry where even a small increase in thermal efficiency of the generating plant can lead to substantial economic benefits. However, it must be recognised that any benefits derived from higher thermal efficiencies may be negated by any consequent decrease in the reliability of the plant. In nuclear power plant it is the latter factor which determines to a large extent the operating temperature of the reactor. Nuclear systems are unique in

that, once the reactor has "gone critical", large parts become completely inaccessible due to radiation hazards. It follows therefore that certain components in the plant must be completely reliable for the design life of the reactor. For example, heat exchangers must be capable of withstanding chemical attack by their environment and retain their integrity for a useful service life of thirty years.

Early MAGNOX reactors used mild steel heat exchangers and this limited the temperature of operation to $\sim$ 425°C. The coolant was CO_2-based and contained 1% CO together with trace amounts of water, hydrogen, nitrogen etc. It was natural for design engineers, in their quest for increased thermal efficiency to increase this operating temperature to $\sim$ 550°C in the second generation of nuclear power stations built in the U.K. These advanced gas cooled reactors (AGR) employ an Fe-9% Cr alloy for the heat exchanger and the gas composition is essentially similar to that of earlier reactors. It is the oxidation behaviour of this alloy system which forms the subject of the present investigation.

Much information is available in the literature on oxidation-resistant steels and this has been recently reviewed by Wood (1971) and Rolls (1973). Wood (1962) has also presented a review of work prior to 1962 which relates particularly to binary iron-chromium alloys. In this chapter only those aspects of direct relevance to the

present work will be described. For a more general review of the field of oxidation the reader is referred to the recent article by Lawless (1974). The present treatment begins with a general discussion of oxidation kinetics and continues with a description of work on iron-chromium alloys, dealing with the effects of alloy composition and gas composition on oxidation behaviour. Work on the structure of oxidation products is presented in two sections, pertaining to thin films and thicker scales respectively. One section of the survey is devoted entirely to a discussion of those properties of oxides belonging to the Fe-Cr-O system which are relevant to the present investigation including their crystal structures, thermodynamic properties and diffusion characteristics. The chapter concludes with a brief outline of the scope of the research programme.

1.2 Oxidation of Metals

Much work has been carried out over the last fifty years to elucidate the practical limits of operation of a range of important commercial metals and alloys in a variety of industrial environments. Although useful practical data may be acquired by this approach, such investigations usually supply little or no knowledge concerning the fundamental mechanisms involved in metal oxidation reactions, knowledge with which long term extrapolations of kinetic data may then be possible. The importance of such mechanistic studies is underlined in the

nuclear energy field where many components of the reactor are required to operate continuously at high temperatures in unusual environments (e.g. CO/CO_2 mixtures, or helium) without attention for periods of the order of thirty years.

The oxidation of pure metals is seldom explicable by a simple mechanism since generally more than one oxide may form, other compounds may be produced (e.g. carbides in CO/CO_2 gas mixtures), stresses may develop and cause scale rupture, pores may form etc. In the case of alloy oxidation the situation is even more complex.

1.3 Oxidation Kinetics

The most general kinetic equation to represent metal oxidation reactions has the form

$$W^n = kt$$

where W is the weight gain and t is the time of oxidation, k is the oxidation rate constant and n is an exponent, where usually $\frac{1}{2} < n < 3$. This equation applies only when the oxidation mechanism does not change as the scale thickens, a situation rarely observed at all stages of oxidation of pure metals as evidenced by abrupt discontinuities in rate curves which are frequently reported. With alloys strict observance of a simple power law is even more rare since the composition of both the oxide scale and the metal changes continuously with time.

The physico-chemical bases of rate laws which can be expressed as simple power functions of time are not well

understood with the exception of the case when $n = 2$. The parabolic rate equation

$$W^2 = k_p t$$

is readily explained on the basis that the rate of oxidation decreases with increasing thickness of the barrier layer as would be expected if the chemical potential of the diffusing species was constant on either side of the barrier layer. Since oxide lattices may be regarded as regular arrangements of metal cations and oxygen anions, it is apparent that the parabolic rate constant, k_p, must be a function of the diffusion coefficients of these species. Assuming that the barrier layer is smooth, homogeneous and uniform and that the oxidation rate is limited solely by lattice diffusion processes (i.e. that reactions occurring at interfaces such as electron transfer or adsorption of the oxidant are not rate-limiting) expressions for k_p may be derived in terms of the defect properties of the film (Wagner 1933). This theory has been validated for cases where these assumptions are met, e.g. oxidation of copper and nickel in oxygen (Wagner and Grunwald, 1938). It is important, however, to realise that rarely, if ever, are the steady state conditions essential to the Wagner approach achieved in long term practical situations.

The oxidation of iron-chromium alloys in CO_2-based gases is complex, the reaction proceeding slowly at first and accelerating with time until parabolic oxidation occurs. (McCoy, 1965; Antill, Peakall and Warburton, 1968.)

1.3.1 Iron-Chromium Alloys

Pure iron oxidises rapidly at high temperature ($>600°C$) in air forming a multilayer scale consisting of haematite, α-Fe_2O_3, at the oxide-gas interface, an intermediate layer of magnetite Fe_3O_4 and an inner layer of wüstite, FeO. The rapid oxidation rate is in part due to the highly defective character of the wüstite phase which allows rapid transport of iron cations across the inner layer (Yearian, Randell and Longo, 1956). Additions of chromium are beneficial since they inhibit the formation of this phase at high temperatures ($>$ 600°C), Seybolt (1960). This classical interpretation of the enhanced corrosion-resistance of iron-chromium is however not relevant to the present study on oxidation in CO_2-1% CO atmospheres at temperatures $<600°C$ since wüstite formation is unimportant, and indeed impossible (at least as a bulk phase) below 570°C. The oxide phase of interest in the current study is magnetite, Fe_3O_4, and its chromium containing homologues, $Fe(Fe,Cr)_2O_4$ which form in the later stages of oxidation and the rhombohedral oxides based on the haematite structure, $(Fe,Cr)_2O_3$, which form in the initial stages.

1.3.2 The Effect of Gaseous Environment on Oxidation Kinetics

McCoy (1965) has studied the behaviour of stainless steels in flowing CO_2 gas in the temperature range 600-1000°C. Parabolic kinetics were in general

observed and the reaction rate was found to be insensitive to pressure above 100 torr ($\sim$ 13 kNm^{-2}). Carburisation reactions may also occur in atmospheres of CO_2/CO. Such reactions have been reported at temperatures $> 600^{o}C$ (Antill et al, 1968; Fujii and Meusner, 1967; McCoy, 1965; Jepson, Antill and Warburton, 1965) and the amount of carbon deposited increases with increase in CO/CO_2 ratio (Surman, 1973).

Two mechanisms have been proposed for the carburisation process. Jepson et al (1965) suggest that carbon is deposited on the surface of the oxide and then diffuses via a solid state diffusion mechanism through the oxide scale to the underlying metal. An alternative mechanism has been proposed for porous oxide scales (McCoy, 1965) in which the CO/CO_2 ratio of the relatively stagnant pockets of gas increase as a result of the oxidation reaction

$$xM + yCO_2 \rightleftharpoons M_xO_y + yCO$$

until it becomes sufficient for the competing carburisation reaction to occur

$$uM + v\ 2CO \rightleftharpoons M_uC_v + vCO_2$$

It should be noted that this latter reaction is accompanied by the removal of gas from the system and hence would result in a pressure gradient across the scale. Carbon deposition or carbide formation is believed to account for only a small fraction ($< 7\%$) of the total weight gain during oxidation (Jepson et al, 1965). However, this figure disguises the potential importance

of carburisation reaction since typical carbides contain only a small weight fraction of carbon (e.g. $Cr_{23}C_6$ ∿ 6% C) compared with the weight fraction of oxygen in typical oxides (e.g. Cr_2O_3 ∿ 30% O).

The role of minor impurities in the gas stream has been discussed by various authors. Some have suggested that water vapour has a deleterious effect on the oxidation rate (Caplan and Cohen, 1959; Yearian, Boren and Warr, 1965) although others disagree (Caplan and Cohen, 1952; Fujii and Meussner, 1960). Explanations of these phenomena usually invoke some modification to the defect structure of the scale caused by either the incorporation of OH^- or H^+ into the lattice. In view of the irreproducible nature of oxidation processes it is possible that the variety of effects reported may have been the result of other minor changes in the oxidation conditions. Surman and Castle (1969) have proposed that a gas phase transport mechanism for certain elements may operate in atmosphere containing water vapour or carbon monoxide; this suggestion is returned to later in connection with metal transport and partitioning effects in oxide scales (see § 4.3).

The effect of other minor impurities in the gas have not been well studied although the possibility of some modification to the oxidation process should not be ignored. The reader is referred to the discussion in Kubaschewski and Hopkins (1962) for a fuller treatment.

Most oxidation studies in CO_2-based gas reported in

the literature were carried out at atmospheric pressure. The effect of gas pressure on both the kinetics and microstructure of the scale has been reported by Antill, Peakall and Warburton (1968). Increase in pressure was found to increase both the rate of oxidation and the amount of carbon deposition. Under high pressure ($\sim$ 20 atmospheres) conditions breakaway oxidation has been observed leading to highly porous non-protective scales. Other work at high pressures on a variety of structural materials has been carried out by Bokros and Wallace (1960).

Little work has been done to establish the possible effects of gas flowrate on the oxidation kinetics or mechanisms in CO_2/CO gas mixtures. It is considered that provided the flowrate is sufficient to ensure that the composition of the gas does not markedly change as a result of the oxidation process, such effects should be minimal.

1.3.3 Effect of Other Alloying Additions

The presence of impurities in metals often profoundly influences the rate of reaction even when present at very low levels. These effects are sometimes attributed to a change in defect structure of the oxide formed and often obey the Wagner-Hauffe rules (Wagner, 1936; Hauffe and Gensch, 1950; Gensch and Hauffe, 1951), When present in sufficiently large concentrations addition elements may also modify the scale structure, e.g. nickel

additions to iron tend to inhibit wüstite formation (Brabers and Birchenall, 1958), or may completely change the oxide formed, e.g. aluminium or chromium additions to iron tend to oxidize preferentially forming Al_2O_3 and Cr_2O_3 respectively. Recent studies (Hales, Hill and Wild, 1973) using Auger electron spectroscopy have also shown that impurities present in very small concentrations in the bulk material, e.g. S in Ni, sometimes diffuse to the surface to form a layer (only a few atom spacings thick) highly enriched in certain elements. This surface enrichment is however sufficient to cause marked changes in the oxidation kinetics. Maldy (1965) has also demonstrated that impurities more noble than iron, e.g. Cu, tend to concentrate in the surface regions of the metal as a consequence of the selective oxidation of the iron matrix. This enrichment is sufficient to cause the transition α-Fe $\longrightarrow$ γ-Fe and is associated with change in the scale structure. The possibility of adventitious impurities should not be overlooked and Hussey, Mitchell, Caplan and Cohen (1972) have recently demonstrated that silicon from silica reaction vessels may be transferred, under reducing conditions, to adjacent metal surfaces. It is apparent that improved oxidation resistance of alloys often results from the formation of a new phase, which is often very thin and is compact, adherent and continuous, with a small defect concentration. For example, it has been suggested that the enhanced resistance to oxidation of silicon-containing alloys may be due to the formation of thin

layers of SiO_2 at the base of the scale (Wood, Richardson, Hobby and Bousted, 1969).

1.4 Oxide Morphology, Structure and Composition

The rate of oxidation of iron-chromium alloys is dependent to a very great extent on the properties of the oxide layer formed. Crystal structure (Gulbransen, Phelps and Hickman, 1946), composition (Caplan and Cohen, 1952), microstructure (e.g. grain size, sub-grain boundaries), (Caplan, Graham and Cohen, 1972) and gross morphology (e.g. density, adherence, continuity) all profoundly influence the degree of protection which the oxide confers to the metal. These parameters are in turn affected by the metallurgical state of the substrate (e.g. annealled, work hardened, texture, grain size) as well as the temperature of oxidation and the gas composition.

1.4.1 Early Stages of Oxidation

Iron-chromium alloys exposed to air are rapidly covered with a thin protective oxide layer $\sim$ 100A thick. This thin film may have a higher chromium to iron ratio than the alloy on which it grows (Vernon, Wormwell and Nurse, 1944). The formation of chromium-rich films is extremely difficult to prevent and it is doubtful whether any oxidation experiments on iron-chromium alloys have ever been conducted without it being present.

Several workers have studied the oxidation of thin ($\sim$1000A) metal foils in the electron microscope (Jannson,

1964; Howes, 1967). Both report the formation of nuclei possessing a "cubic" structure. Howes (1967) however suggests that this cubic oxide may in fact be the tetragonal phase γ-M_2O_3. This oxide has a crystal structure closely related to cubic M_3O_4 and only in exceptional circumstances is it possible to distinguish unambiguously the two structures by electron diffraction. The presence of tetragonal oxide was unexpected, since from thermodynamic arguments the rhombohedral phase α-M_2O_3 would be predicted. The presence of γ-M_2O_3 was explained (Howes, 1967) by assuming that interfacial criteria controlled initial oxidation rather than criteria extrapolated from thermochemical measurements on bulk oxides. With continued oxidation a thin, coherent, rhombohedral oxide, α-M_2O_3, was found to develop. These arguments are developed further in the present work, see § 4.5. Moreau and Bénard (1956) have also studied the initial oxidation of an Fe-18% Cr alloy and report the formation of Cr_2O_3 nuclei. However, the temperatures employed were higher ($\sim$ 1200°C) and the oxygen partial pressure of the gas was lower ($p_{H_2O}/p_{H_2} = 4 \times 10^{-3}$) than that employed in the present work.

The nature of the nucleation site is not well established. Although Howes (1967) found no association of oxide nuclei at the surface with dislocations in the metal, Whitlow (1973) asserted that the number of oxide nuclei corresponded closely to the estimated dislocation density. The initial slow period of oxidation observed

may be associated with the formation of a continuous film of chromium-rich rhombohedral oxide. This is in accord with the low ionic conductivity of this phase (Hoar, 1959; Meadowcroft and Hicks, 1972). Other forms the initial oxide may take have been described by Gulbransen and Copan (1959, 1960). These workers showed that under certain oxidation conditions (low oxygen partial pressure and the presence of water vapour) iron oxidised to form platelets and whiskers of haematite α -Fe_2O_3. The growths are extremely thin ($\sim$ 100A) and were ascribed to stress in the metal substrate.

In addition to the work reported above on the oxidation of iron-chromium alloys and similar systems the following investigations on the initial oxidation of other metals is of particular relevance to the present investigation.

Mehl and McCandless (1937) studied the orientation of oxide films formed on iron and noted that definite epitaxial relationships existed between the cubic oxide and metal such that

(100) oxide // (100) metal

and [110] oxide // [100] metal

The oxidation rate was found to be a function of the orientation of the metal substrate although no simple relationship between rate and orientation was found. Bénard (1960) interpreted the initial reaction as a three stage process. Firstly an invisible film is formed

perhaps only a monolayer or so thick; secondly with continued oxidation nuclei form; thirdly the nuclei grow laterally until the entire surface is covered (see § 4.6). This sequence has been observed on several metals: iron (Bardolle, 1954), nickel (Martius, 1955) and an Fe-18% Cr alloy (Moreau and Bénard, 1956).

On iron the nuclei density varied with orientation, the maximum density being observed on (100) metal planes. In a series of studies on copper single crystals Lawless and Gwathmey (1956) have identified crystal orientation relationships between Cu_2O and the copper metal substrates. These authors considered that the matching of rows of closely packed atoms in the metal and oxide was more important than matching of individual atoms in determining epitaxial relationships and noted that the degree of orientation decreased with increase in film thickness and with decrease in temperature. Young, Cathcart and Gwathmey (1956) have demonstrated the dependence of oxidation rate on crystal orientation of the substrate by means of many striking photographs of oxidised single crystal spheres. The careful work of Borie, Sparks and Cathcart (1962) using X-ray diffraction techniques to study the initial oxidation of copper should be noted. By analysis of line profiles of the diffraction maxima these workers demonstrated the presence of a stress gradient in the oxide and also postulated a detailed model of the dislocation substructure in growing oxide films.

Before leaving the subject of initial oxidation

studies it should be mentioned that recently several elegant studies of composition profiles in thin films have been published. Of particular relevance is the work of Stoddart and Hondros (1972) who have studied the segregation of chromium and other elements in the initial oxide films using Auger electron spectroscopy. Indeed with the increasing availability of new techniques (electron spectrometry, secondary ion mass spectrometry, ion scattering spectrometry and X-ray appearance potential spectrometry) for surface composition analysis many interesting and fundamental studies of the composition of thin oxide films will become possible in the near future which should increase our present scant knowledge in this field.

1.4.2 The Formation of Oxide Scales

Oxide scales are generally assumed to be oxide layers of thickness greater than one micron. The scales are therefore easier to study than thin films and a whole range of established metallographic techniques are available for this purpose. The literature abounds with many fine examples of metallographic studies on both pure metal and alloy systems.

The processes leading to the breakdown of the initial rhombohedral oxide film have been discussed by Yearian, Randell and Longo (1956) and Wood and Whittle (1967). Oxidation in air produces an outer oxide of iron-rich α-M_2O_3 while the inner layer contains less oxygen. Wüstite, MO, formation does not occur unless the chromium

additions are very dilute (Seybolt, 1960) and the inner layer is usually a mixed spinel; on very high chromium steels some Cr_2O_3 may be formed at the base of the scale. The outer layer is probably produced by outward movement of cations (Pfeil, 1929; Dravnicks and McDonald, 1948; Mrowec, 1967). The situation is less clear for oxidation in CO/CO_2 atmospheres although most workers report the formation of a duplex scale consisting of an outer layer of magnetite, Fe_3O_4 (e.g. Antill, Peakall and Warburton, 1960). Carbon deposition as free carbon or carbide also occurs (Antill and Warburton, 1967; McCoy, 1965), although the exact location of carbon in the scale is uncertain. Considerable carbon penetration into the substrate has been noted (Fujii and Meussner, 1967).

Pores in the scale are often observed and have been attributed either to scale cracking or vacancy condensation processes. Cracks may be formed by a variety of processes such as stress generation in the oxide due to the volume change associated with conversion of metal to oxide, temperature cycling (Wood and Whittle, 1964), recrystallisation in the oxide (Yearian, Derbyshire and Radavich, 1957) etc; such stress raising processes have been reviewed in recent articles by Douglass (1969) and Stringer (1970). Evans (1947) has suggested several ways in which stresses may result in cracking of the scale. Pores which are produced by a vacancy condensation process, resulting from the high concentration of vacancies generated as a result of outward movement of metal ions,

are discussed by Dunnington, Beck and Fontana (1952) and further developed in the present work (see § 4.4).

1.4.3 Effect of Other Alloying Elements on the Scale Structure

Oxidation of most ferrous alloys leads to a duplex oxide structure. The outer layer invariably contains not only iron but also manganese if this element is present in the original alloy, while the inner layer contains iron together with most of the other metallic elements present (Pfeil, 1929; Antill, Peakall and Warburton, 1968). This segregation effect is well established and may be related to the relative diffusion rates of metal ions in the close packed oxide lattice (see § 4.3). Surman and Castle (1969) have explained these observations for steels oxidised in H_2O/H_2 or CO_2/CO atmosphere on the basis that iron forms volatile compounds in these gases (and hence is mobile) while for chromium and most other metals no such compounds have been identified. This volatility permits gas phase transport of iron to the outer oxide. Obviously this explanation is hardly tenable for other oxidising environments such as pure oxygen. The effect of various additions to iron-chromium alloys has been examined in some detail. Some additions, e.g. molybdenum and vanadium, are clearly undesirable in high concentrations since the volatility of their oxides can result in a complete loss of protection (Brenner, 1955). Even small additions of carbon may be deleterious since

carbon in steels catalyses further carbon deposition from CO/CO_2 gases and release of carbon monoxide from the metal may cause blistering of an otherwise protective scale under more oxidising conditions (Boggs and Kachich, 1969). Aluminium additions are in general beneficial since very protective Al_2O_3 scales may form. However the response of Al_2O_3 films to thermal cycling is not good and under these conditions Cr_2O_3 films are better. Rare earth additions also are known to be beneficial due, it has been suggested, to the keying action of the acicular M_2O_3 crystals formed at the interface (Francis and Whitlow, 1966) or possibly because the large rare earth atoms in solution in the metal act as vacancy traps and hence prevent void nucleation (Tien and Rand, 1972; Tien and Pettit, 1973).

1.5 Properties of Oxide Materials

It is apparent from the foregoing discussion that the oxidation of metals is determined by the chemical, physical and mechanical properties of the barrier layer of oxide which separates the metal from its oxidising environment. In this section some properties of oxides will be reviewed with special reference to oxides formed on iron-chromium alloys: MO, M_3O_4, γ-M_2O_3 and α-M_2O_3.

1.5.1 Crystal Structures of the Oxides

The oxides of the type MO are typified by Wüstite, FeO. This has the rock-salt structure (Wells,

1962) in which the oxide anions form a cubic close-packed arrangement and the divalent metal cations occupy the octahedral interstices. The maximum chromium solubility in this phase is low ($\sim$ 2% at 1000°C), which is in accord with the predictions of crystal field theory (Dunitz and Orgel, 1957) since it is energetically unfavourable for chromium ions to occupy tetrahedral sites. Wüstite is substantially metal deficient and is best represented as $Fe_{1-x}O$. Some iron cations are thus in the Fe^{3+} state in order to preserve electrical neutrality and some of the octahedral sites are vacant. The high mobility of iron cations in the oxide has been attributed to this defect structure, although recent Mossbauer studies have shown that the defect structure is rather more complicated than this simple description (Greenwood and Howes, 1972). The oxide is a p-type semiconductor.

Oxides of the M_3O_4 type usually possess spinel lattices. The spinel unit cell consists of cubic close-packed arrangements of 32 oxide anions. One half of the octahedral interstices are occupied together with one-eighth of the tetrahedral sites. In a normal spinel the divalent ions occupy the tetrahedral interstices and the trivalent ions occupy the octahedral interstices. Fe_3O_4 is an inverse spinel in which half the trivalent ions now occupy the tetrahedral sites and the octahedral sites contain both trivalent and divalent ions. This is in accord with crystal field theory, since Fe^{3+} ions have no preference for either octahedral or tetrahedral sites while

Fe^{2+} has a small preference for octahedral sites. Fe_3O_4 is a good electrical conductor due to the ease of electron transfer between Fe^{2+} and Fe^{3+} in the octahedral sublattice by an electron hopping mechanism, (Robbins, Wertheim, Sherwood and Buchanan, 1971). Substitution of Cr^{3+} in the spinel lattice causes a variety of changes to occur and these have been investigated by a number of workers. Yearian, Kortright and Langenheim (1954) studied the lattice parameter of the system Fe $(Cr_{2-x}\ Fe_x)\ O_4$ and showed that it initially rises from the value of 8.396 for the unsubstituted spinel Fe_3O_4. This has the inverse structure and this initial rise is in accord with the larger ionic size of Cr^{3+} compared with Fe^{3+} (0.69Å and 0.64Å respectively). The inverse structure is maintained up to $x \backsim 0.3$, after which the lattice parameter decreases with increase in the concentration of substituent. In this range of composition the structure changes gradually to the normal spinel form. The transition is complete when $x \backsim 1.4$ and with continued substitution the lattice parameter again rises at a rate similar to that observed in the initial region ($0 < x < 0.3$), until $x = 2$. These observations are in agreement with the predictions of crystal field theory since chromium, with its high octahedral preference energy, can be substituted for Fe^{3+} in the inverse spinel lattice only up to $x \backsim 1$, while the normal spinel structure can accommodate chromium in all the normally occupied octahedral sites, i.e. up to $x = 2$. This interpretation of the lattice parameter changes is in

complete accord with recent Mossbauer spectroscopic measurements (Robbins et al, 1971). The changes in lattice parameter are also associated with an increasing resistivity of the material as the possibilities for electron hopping become more limited with increasing substitution. Fe_3O_4 is believed to be a metal deficient p-type oxide. It should be noted that pure magnetite, Fe_3O_4, is magnetic while the chromium-rich spinel $FeCr_2O_4$ is non-magnetic. An oxide phase Cr_3O_4 is also known to exist at high temperature as inclusions in chromium steels (Hilty, Forgeng and Folkman, 1955). It is not however a cubic spinel but a tetragonally distorted spinel oxide ($c/a = 0.86$); the distortion is probably caused by the Jahn-Teller effect (Dunitz and Orgel, 1957b) since the d^4 ion, Cr^{2+}, is now present. The Cr_3O_4 phase has not been identified in oxide scales formed on chromium steels and it is possibly only formed at high pressures such as may be found in the interior of chilled ingots.

γ-M_2O_3 oxides are also usually of the spinel type but only γ-Fe_2O_3, maghemite, has been well characterised. It may be formed by the careful oxidation of magnetite or reduction of hematite. The structure is very similar to magnetite but $1/9$ of the metal atoms are replaced by vacancies (Wells, 1962). The unit cell is tetragonal with a c/a ratio of 3 and may be regarded as three modified magnetite unit cells stacked linearly. No references to chromium-containing homologues are known to the author, although a cubic Cr_2O_3 has been described by Laubengayer

and McCune (1952). In view of the similarity of the structures of magnetite and maghemite it is likely that chromium substitution will be governed by similar crystal field considerations to those that apply to the system $Fe(Fe, Cr)_2O_4$. This general similarity of the two structures makes the unambiguous identification of maghemite by electron diffraction extremely difficult since all the diffraction maxima due to magnetite also appear in the pattern from maghemite. Maghemite does have several unique lines but these are either weak or their d-spacings so large that they can be detected only with difficulty. In the author's opinion positive identification is only possible from single-crystal spot patterns where many of the weaker diffractions are strong enough to be detected.

α-M_2O_3 oxide lattices are rhombohedral. They may be regarded as a hexagonal arrangement of anions in which $^2/_3$ of the octahedral interstices contain trivalent cations, the tetrahedral sublattice being unoccupied. A complete range of solid solution of Fe_2O_3 and Cr_2O_3 is possible (Wretblad, 1930), again in accord with the predictions of crystal field theory. The lattice parameters of the end members Fe_2O_3 and Cr_2O_3 are very similar ($a = 5.419$, $\alpha = 55.28°$ and $a = 5.348$, $\alpha = 55.11°$ respectively) and in general the two structures cannot be distinguished by electron diffraction. Fe_2O_3 is believed to be an n-type oxide while Cr_2O_3 is believed to be p-type (Meadowcroft and Hicks, 1972). Hence at some intermediate composition intrinsic conductivity is expected. Footner, Holmes and

Mortimer (1967) have invoked this phenomenon to explain an observed minimum oxidation rate at a chromium composition of $\sim$ 18% for binary alloys oxidised at temperatures from 600° - 900°C.

1.5.2 Thermodynamic Consideration

Thermodynamic principles have often been applied to metal oxidation. In general thermodynamic constants for bulk materials are known only for pure substances. Most oxide scales formed on alloys are however solid solutions. Furthermore data are usually referred to standard state conditions, i.e. pure bulk metal in equilibrium with the corresponding oxide at an oxygen pressure of one atmosphere. In a growing oxide scale the oxygen pressure would vary throughout the scale thickness. In the usual case of oxidation under flowing gas conditions equilibrium can never be attained. Hence oxidation products may form which would not be predicted thermodynamically (Gulbransen, 1965). For example, although Cr_2O_3 and Fe_2O_3 are both completely miscible in one another at equilibrium, they do not commonly form continuous solid solution in oxide scales (Wood, 1962).

The thermodynamic properties of oxides are most conveniently presented in the form of free energy vs. temperature diagrams. The diagram, Fig. 1.1, was taken from the work of Richardson and Jeffes (1948, 1949) and contains information for iron and chromium oxides together with data representing the equilibrium between carbon and its various

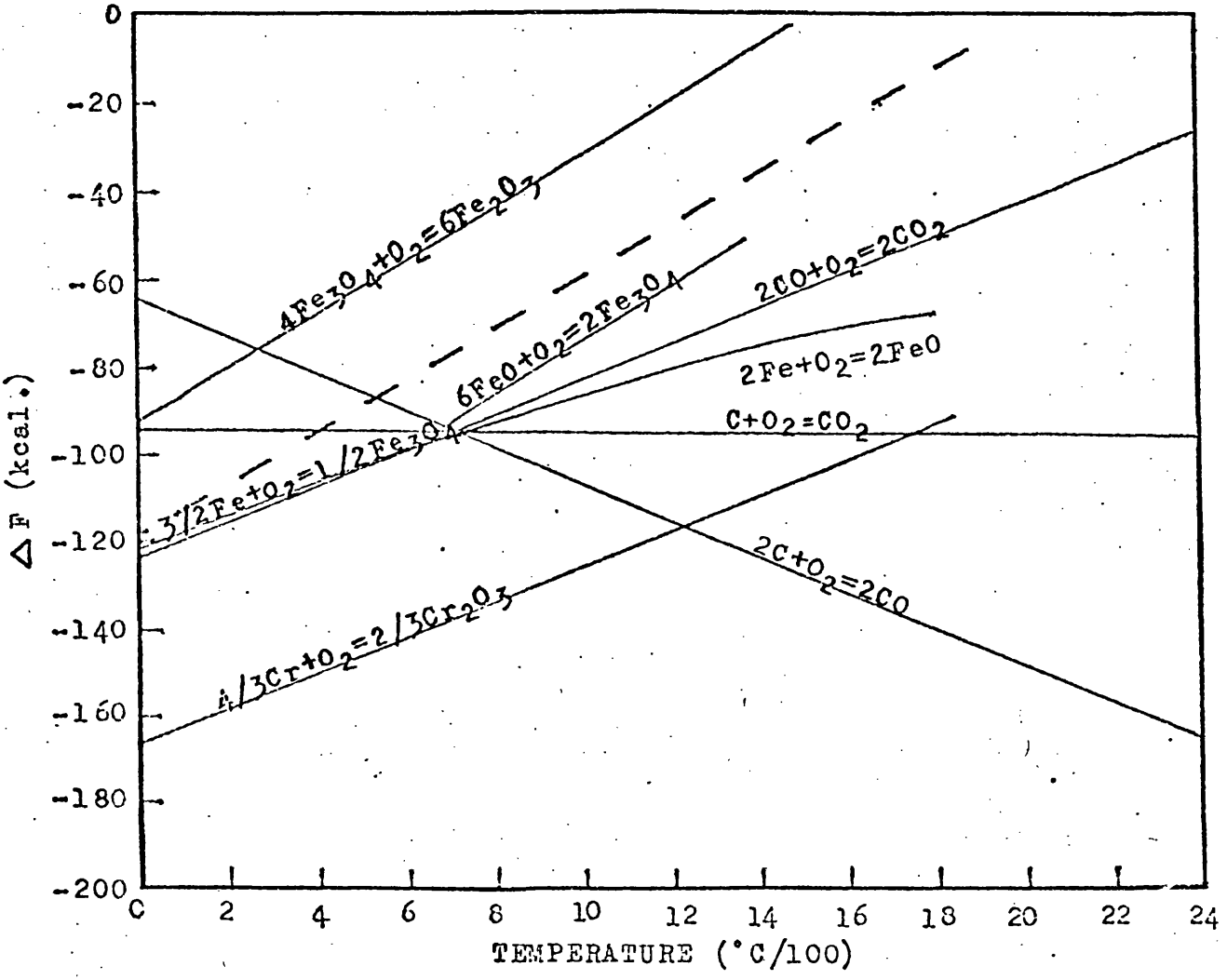

Fig.1.1 Free energy vs temperature plot for some binary oxides relevant to the present work. Dotted line shows the free energy vs temperature relationship for CO_2 - 1% CO gas mixture.

oxides. Relatively little data are available for complex oxides, although Tretjakow and Schmalzried (1965) have estimated that the free energy of formation of most spinels from their parent oxides (i.e. $AO + B_2O_3 \rightleftharpoons A B_2O_4$) is $\sim$ 5-10 k cals/mol ($\sim$ 20-40 k J mol). It can be seen from the diagram that Cr_2O_3 is the most stable oxide while Fe_2O_3 is the least stable. Data for γ-Fe_2O_3 are not available. This oxide is always thermodynamically unstable with respect to α-Fe_2O_3 and Lodding and Hammel (1960) have estimated the enthalpy change associated with this transformation to be 47.5 ± 2.3 cal g^{-1} ($\sim$ 200 k J kg^{-1}).

A further restriction on the applicability of classical thermodynamics to oxidation phenomena arises because in many cases the characteristics of the oxidation products do not correspond to those of bulk material. For example in the initial stages of oxidation the surface to volume ratio of the thin film is very large and interfacial phenomena undoubtedly play an important role in determining the mechanism. Furthermore oxide scales are often microcrystalline or even amorphous and again interfacial effects may assume much importance. Unfortunately values for interfacial energies in solid systems are not well documented, which is not altogether surprising since the interfacial energy is a continuous function of orientation. Jones (1971) has reviewed interfacial energies of pure metal systems and typical values of around 1000 erg cm^{-2} (= 1 J m^{-2}) are quoted. Kelly (1966) gives values

for a few ceramic systems and values of $\sim$ 1000 erg cm^{-2} ($\sim$ 1 K m^{-2}) would seem typical. Little information is available concerning metal-ceramic interfaces but a value of 400 erg cm^{-2} (0.4 J m^{-2}) is given for the interfacial energy between iron and wüstite by Turpin and Elliot (1966). Values of interfacial energy would be expected to vary considerably from one system to another and with orientation. Simple arguments suggest that they are a function of the degree of mismatch between atoms on either side of the interfacial plane and of the atomic population of these planes (Kelly, 1966).

1.5.3 Atomic Transport Properties

The mobile species in metal oxide systems are usually ions. Since the metal cation M^{n+} is usually much smaller than the oxygen anion O^{2-} ($\sim$ 0.7A and 1.4Å respectively) cation transport is usually dominant.

As discussed in section 1.5.1 cations may be regarded as occupying the interstices in a close packed array of oxide ions, the interstices being of two types according to the local disposition of oxide ions. Octahedral sites, which are surrounded by six oxide ions all equidistant one from another can easily accommodate ions up to $\sim$ 1Å without much lattice distortion. Tetrahedral sites lie at the centre of four equidistant oxide ion and being smaller can only accommodate ions up to $\sim$ 0.7Å without strain. Various workers (Azaroff, 1961; Tilley and Stone, 1972) have considered the possible paths that a

cation may take in moving through a close packed array of anions. For cubic anion arrangements the easiest route is via alternate, adjacent octahedral and tetrahedral sites while for hexagonal anion arrangements an alternative route via octahedral sites only is also available. The latter route runs parallel to the C-axis and has led Tilley and Stone (1972) to postulate a diffusion anistropy in hexagonal oxides. Various values for the diffusion coefficient are available in the literature (e.g. Askill, 1971) but in general the data are inconsistent and in most cases far outside the temperature range of interest (400-600°C) in the present study.

In addition to the importance of bulk diffusion processes to oxidation mechanisms it is probable that both grain-boundary and surface diffusion play a significant role in determining the rate of reaction. Their contributions will be most marked for materials with a high surface or interfacial area to volume ratio. It has been shown (Shewmon, 1963; Kofstad, 1966) that the activation energy for grain boundary diffusion and surface diffusion is less than that for bulk diffusion, i.e. $E_{\text{grain boundary}} \backsim \frac{1}{2} E_{\text{bulk}}$ and $E_{\text{surface}} \backsim \frac{1}{3} E_{\text{bulk}}$. It can be seen that the importance of grain boundary and surface diffusion increases rapidly as the temperature is reduced.

1.5.4 Oxide-Oxide Reactions

The rate of formation of complex oxides from pure oxide materials has been studied by several workers.

While, however, most of these studies are of great academic interest, since they enable detail mechanisms for the interdiffusion of the atoms to be postulated, they are not directly applicable to the present investigation. Recent work of Whitlow (1973) on the reaction of a wide range of oxides of importance to stainless steel oxidation is more relevant. This study showed that FeO and Cr_2O_3 react readily at 1000°C to form the spinel $FeCr_2O_4$. A number of other reactions involving other oxides (e.g. NiO, MnO, SiO_2 etc.) were also discussed. Unfortunately no studies were made of reactions at low temperatures ($<$ 800°C).

1.6 The Present Investigation

In the previous sections the literature on the oxidation of iron-chromium alloys has been reviewed with particular reference to CO_2/CO atmospheres. Some important properties of oxide materials have also been discussed. It is apparent from this survey that the mechanism of oxidation is by no means well understood. In the present work attention is focussed particularly on:

(a) mechanisms involved in formation and breakdown of the thin protective films (§ 4.5 and § 4.6);

(b) atom transport processes associated with the production of the inner oxide layer in thicker duplex scales together with observed element partitioning effects (§ 4.2, § 4.3 and § 4.4);

(c) formation of voids within the scale and their subsequent effect on the oxidation reaction (§ 4.4).

The experimental work has involved two complementary lines of approach to the problems: a thermogravimetric study of the reaction kinetics and a detailed investigation of the morphology, structure and composition of the oxidation products. New information is presented from which mechanisms have been proposed to account for the structure and properties of oxide films formed in the initial stages of oxidation on alloys of different chromium content. A model is proposed to interpret the formation of duplex scales on iron-chromium alloys and the distribution of elements in the scale. Special attention is given to the presence of pores and a periodic vacancy condensation process is invoked to explain the distribution of pores in the inner layer. The importance of voids in relation to oxidant transport through the scale is also considered.

CHAPTER 2

EXPERIMENTAL PROCEDURES

2.1 Fe-Cr alloys used in the investigation

Most of the experiments were performed on polycrystalline material supplied by the Fulmer Technical Services. The alloys were prepared by vacuum melting electrolytic chromium and carbonyl iron together in the required proportions and casting into 500g billets. These were cold rolled down to 1mm thickness sheet using interstage anneals and cut into coupons approximately 50mm x 10mm x 1mm. Nominal compositions of the alloys are given in Table 2.1.

Table 2.1

Nominal composition of the polycrystalline iron-chromium alloys

	C	N	S	P	Mn	O
Grade 1 Chromium Carbonyl Iron	50 0.02	20 0.02	0.003	0.0015	0.01	120 ppm low %

Cast No.	Chromium Content Wt %	Comments
J 109	5	Uneven thickness
J 110	9	
J 111	12	
J 112	15	
J 113	20	
J 115	5	

As-received specimens of each composition were mounted in bakelite, sectioned and polished for examination under the optical microscope. Etching the specimens with acidic ferric chloride revealed a typical cold worked structure of elongated grains. The high chromium alloys (J 112 and J 113) contained a few small inclusions ($<0.1mm^{-2}$) and the remaining alloys were almost inclusion free. Portions of the original alloy castings were also supplied by the Fulmer Technical Services and these were subsequently cold rolled to produce a few specimens of thickness greater than 1mm.

In addition to polycrystalline metal oxidation experiments were carried out on two single crystals of iron-chromium alloys. The single crystals, supplied by Metals Research Ltd. as randomly oriented bar 10mm diameter, had nominal compositions of Fe-15% Cr and Fe-70% Cr respectively and were prepared from 5N purity starting materials. The Fe-70% Cr material was relatively inclusion free while the Fe-15% Cr alloys contained inclusions of two types: large inclusions, visible on polished sections under the optical microscope, which has a rosette habit and thin ($\sim$100nm) platelets, seen on subsequent etching, up to 1mm long and almost always aligned parallel to the [110] directions in the crystal. Examination in the electron probe microanalyser showed both types of inclusions to be chromium rich, no depletion of chromium in the

surrounding matrix was detected.

2.2 Specimen preparation

Polycrystalline specimens were firstly etched in a hot solution containing 30% nitric acid , 15% hydrochloric acid, 10% hydrofluoric acid and 45% water to remove surface contamination. They were then annealed in deoxygenated, dry (dew point -196°C) hydrogen at 1000°C for 2 hours and then allowed to cool slowly in the furnace to stabilise their metallurgical structure. Although no visual evidence of oxide formation was apparent after this operation a further etch was carried out to ensure an uncontaminated surface just prior to oxidation. A few polycrystalline specimens were electropolished in a solution of 20% perchloric acid in glacial acetic acid at 30V instead of the final etching treatment. Optical microscopy of polished sections showed the grains to have a wide distribution of sizes and the mean grain size increased from some tens of microns for the low chromium alloys to several hundred microns on the Fe-20% Cr alloy. A scanning electron micrograph of a typical etched surface is shown in Fig.2.1.

The orientation of the single crystal bars were determined using the back reflection Laue technique. Approximately parallel sided slabs corresponding to (100), (110) and (111) faces were then cut from each single crystal using a high speed silicon carbide slitting disc. Surfaces were ground using increasingly

Fig.2.1 Etched metal surface prior to oxidation.
Scanning electron micrographs X 1000.

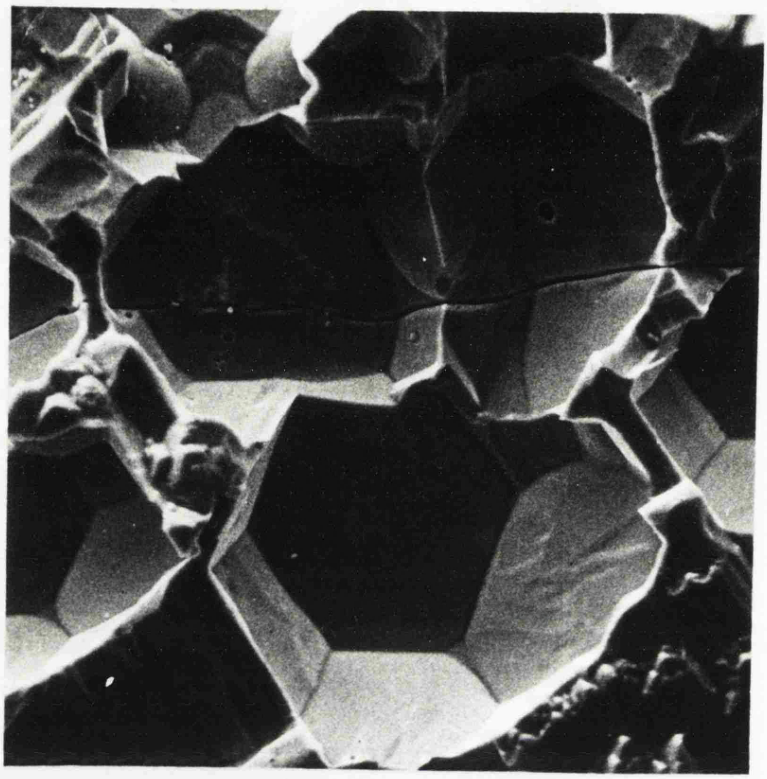

Fig 2.1

finer grades of silicon carbide paper, polished on 6μm and 1μm diamond impregnated cloths and finally electro-polished as described above. Each surface orientation was checked by electron diffraction and if necessary reprepared until it was within ± 3° of the required crystal plane. The principle directions in the plane were also noted. Surfaces prepared in this way gave elongated spot patterns superimposed on a sharp Kikuchi pattern, indicating that the surfaces were smooth and free from both contamination and mechanical disturbance. Some oxidation experiments were performed on single crystals given a similar etch treatment to that employed for the majority of the polycrystalline specimens. The etched surfaces were faceted on a fine scale, the dominant facets were (111) and (100) on all surfaces. Reflection of a fine beam of light from a He-Ne laser from these surfaces produced broad spots indicating some curvature ($\sim 5°$) of the facets.

2.3 Oxidation apparatus

The apparatus used in this study consisted of two oxidation reaction systems sharing common vacuum and gas supply services. In the first system twelve specimens may be oxidised simultaneously to provide samples for microstructural characterisation; four specimens may be removed individually without disturbing the other specimens, the temperature or the gas flow. In the other system a single specimen was suspended from a

sensitive microbalance enabling the kinetics of oxide formation to be followed gravimetrically; these specimens were also studied metallographically.

The apparatus is illustrated in Fig. 2.2. In the centre may be seen the vacuum trolley, consisting of a rotary pump backing a 1" air cooled oil diffusion pump. A vacuum manifold connects the two oxidation systems to the vacuum trolley. The vacuum pumping apparatus enables a pressure of 5×10^{-5} torr (6.6×10^{-3} Nm^{-2}) to be attained just above the baffle valve after 16 hours pumping. The microbalance (Sartorius, Model 4104) is positioned to the right; it will be discussed in more detail later. To the left of the vacuum trolley is the furnace containing the metallographic specimens; the extraction mechanism for removing these specimens will be dealt with below.

To the left of the metallographic furnace is the gas mixing and humidification equipment.

2.3.1 Temperature measurement and control

The nichrome wound furnaces were controlled by two Ether "Mini" controllers capable of maintaining the temperature within $\pm$ 2°C of the set value. The sensing elements were chromel-alumel thermocouples positioned in silica sheaths close to the furnace walls.

The microbalance furnace had two coaxial heating elements wound in opposite directions, the ratio of

Fig.2.2 The oxidation apparatus. Note the microbalance rig (right), the vacuum pumps and guages (middle), the metallographic furnace (left) and the gas control equipment (extreme left).

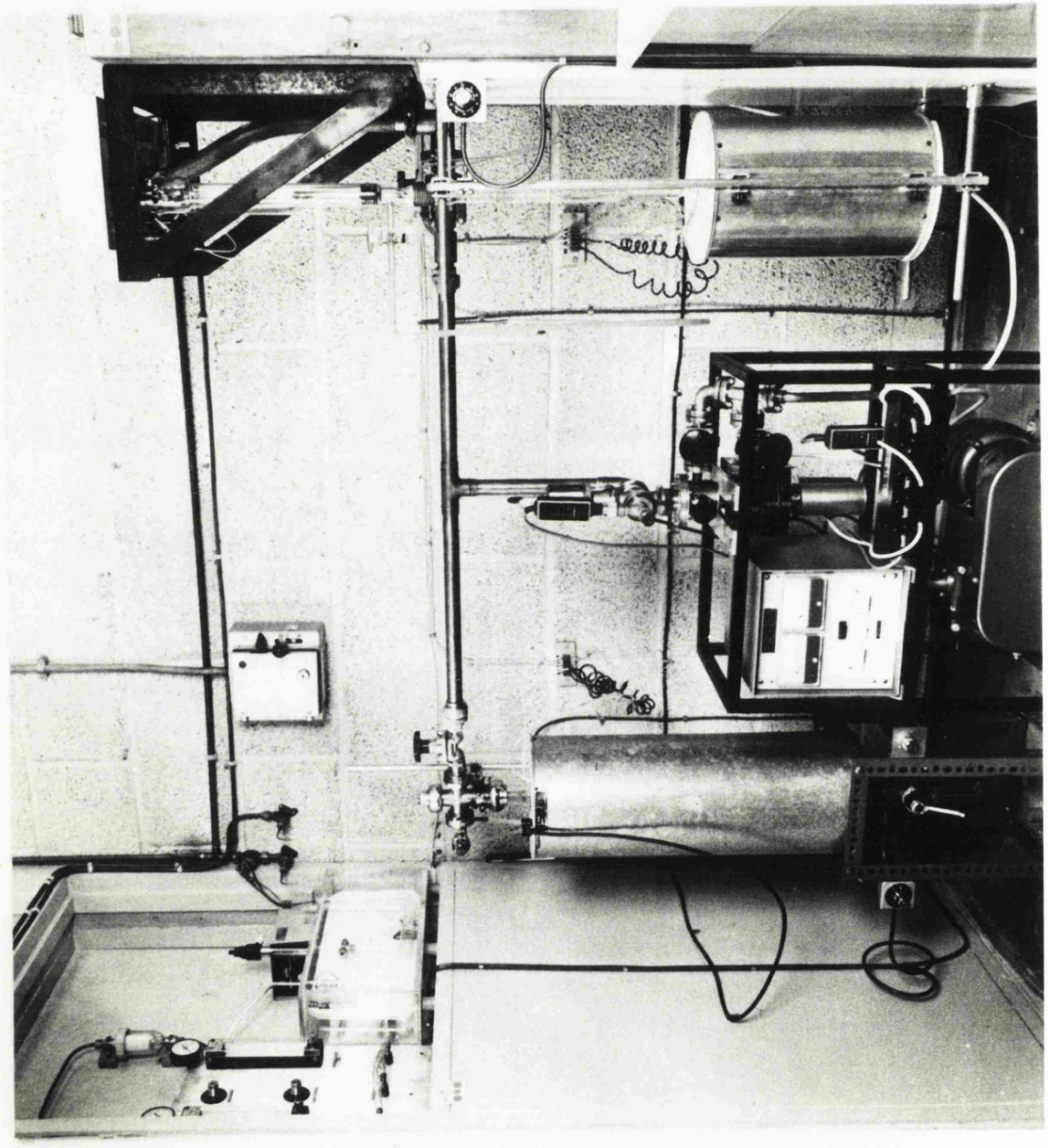

Fig. 2.2

the currents in the two windings being adjusted using a variable resistance to give no resultant force on the ferromagnetic specimens. This arrangement was necessary to prevent oscillations of the microbalance readings in sympathy with the switching of the furnace controller.

The temperature of the furnaces was monitored using chromel-alumel thermocouples adjacent to the silica reaction tubes. Thermocouple outputs were recorded on a 5mV Ether "X actline" sixpoint recorder; excess output voltage from the thermocouples was backed off using a high stability voltage source. The overall sensitivity of the system was 2.5°C/division. The reference junction for the thermocouples was maintained at a constant known temperature using a thermostatic water bath.

2.3.2 Gas composition

Initial studies were made using gas of nominal composition CO_2-1% CO supplied by Air Products Ltd. in cylinders at 260 p ig. The oxygen and water content were specified by the manufacturers as $<$3ppm and $<$5ppm respectively. For later studies a dynamic mixing system was employed in which a nominal CO_2-10% CO blend was diluted to the required concentration (CO_2-1% CO) using high purity CO_2. A schematic diagram of the gas control system is shown in Fig. 2.3

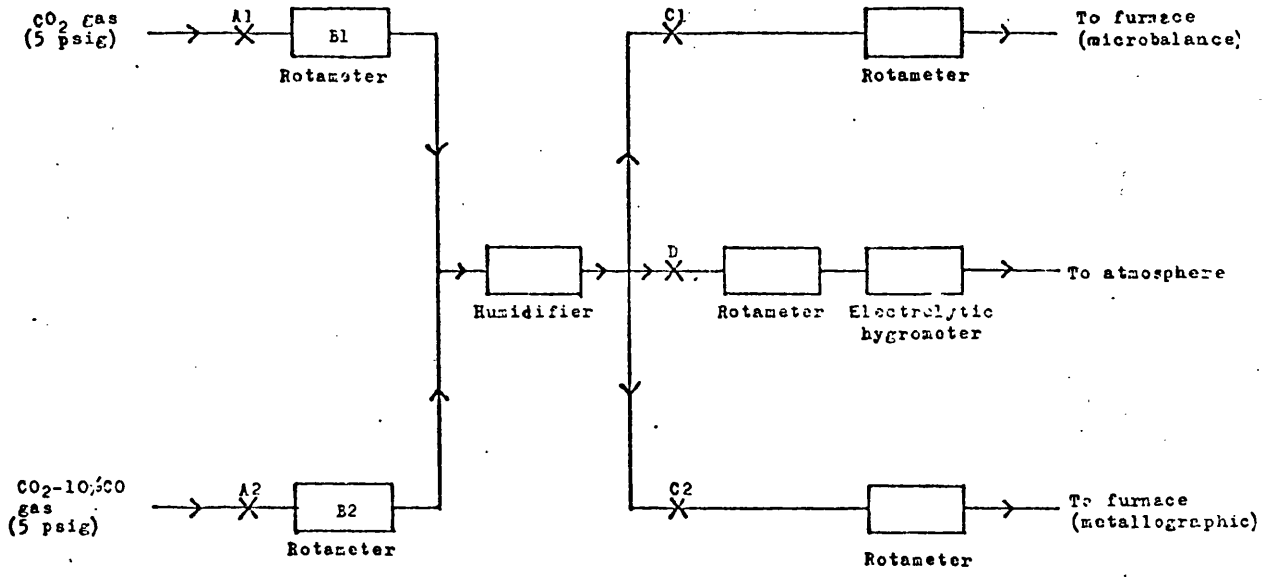

Fig.2.3 Schematic diagram of the gas control apparatus.
A1, A2, C1, C2, D Needle valves (see text).

The gases from the storage cylinders were first regulated to a constant pressure (5psig) and then each metered using needle valves A1 and A2 and the rotameters B1 and B2 in the proportions necessary for the required gas mixture. The two gas streams were combined in a manifold and passed through a humidifier prior to being distributed via needle valve (C1, C2 and D) and rotameters to the two furnaces.

The composition of the gas entering the two furnaces was shown by gas chromatography to be identical indicating that efficient mixing occurred. A small bleed of gas (10ml min^{-1}) could be diverted through a coulometric hygrometer to check the water content. The stability of the flowrates was ± 20% of the set value over a 24 hour period. The gas was humidified by allowing water vapour to diffuse through a tube into the gas stream using the apparatus shown in Fig. 2.4.

The entire humidification apparatus was maintained at a constant temperature in a thermostatic water bath. It can be shown that provided the partial pressure of water vapour in the exit gas is very much less than the saturated vapour pressure of the water in the reservoir the rate of mass transport of water is given by:

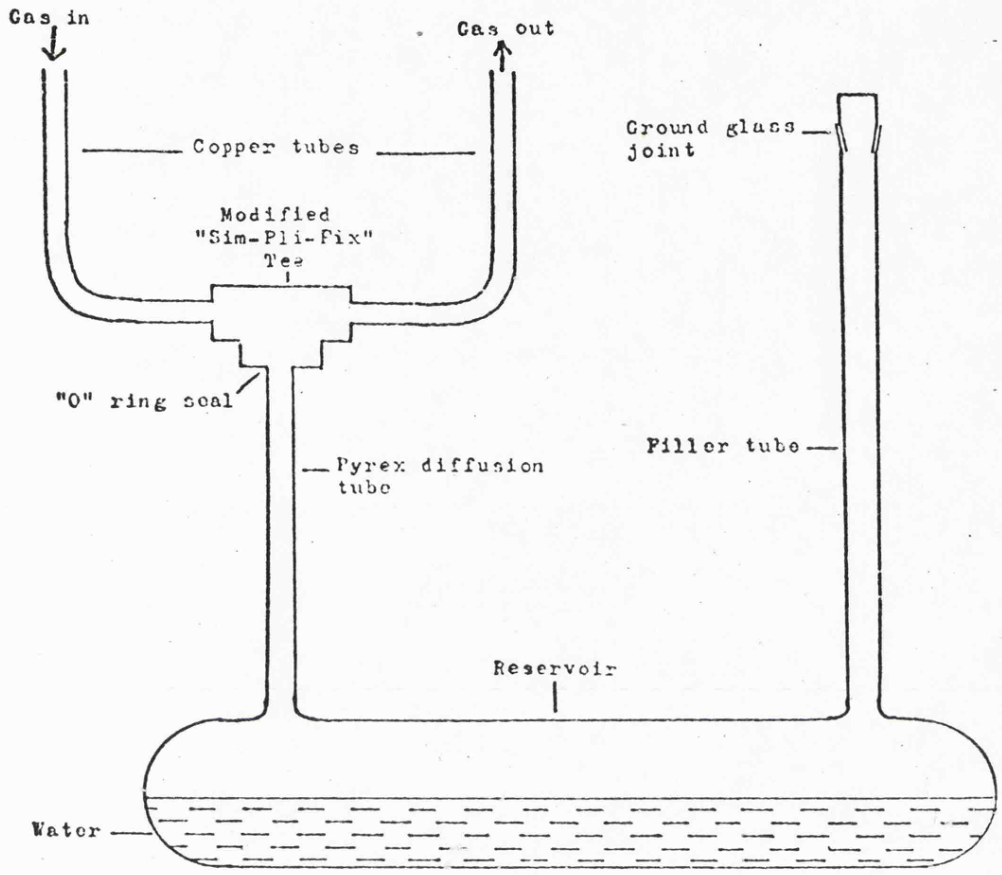

Fig.2.4 Apparatus for addition of water vapour to the gas stream.

$$\frac{dm}{dt} = \frac{D\ d^2\ PoM}{4\ RT\ l}$$

where D = diffusion coefficient of water vapour in CO_2-1% CO at the temperature and pressure of the system

d = diameter of the diffusion tube

Po = the saturated vapour pressure of water

M = molecular weight of water

R = gas constant

T = temperature

l = length of diffusion tube.

For a given geometry the rate of mass transport can be easily adjusted by altering the temperature of the apparatus. Using a 90mm x 5mm tube and a flowrate of 100ml min^{-1} the water concentration of the gas leaving the humidifier could be maintained at 200ppm with the apparatus at 26°C. However the water content of the gas streams as they entered the furnaces were found to vary with time due to the sorption and desorption of water from the walls of the connecting tubing with changes in ambient temperature; this could be as much as ± 150ppm for large changes over short periods of time.

2.3.3 Metallographic furnace

Specimens were supported by a stainless steel assembly fitted inside a 32mm silica reaction tube, Fig. 2.5. This assembly consisted of four $^1/_{16}$" rods

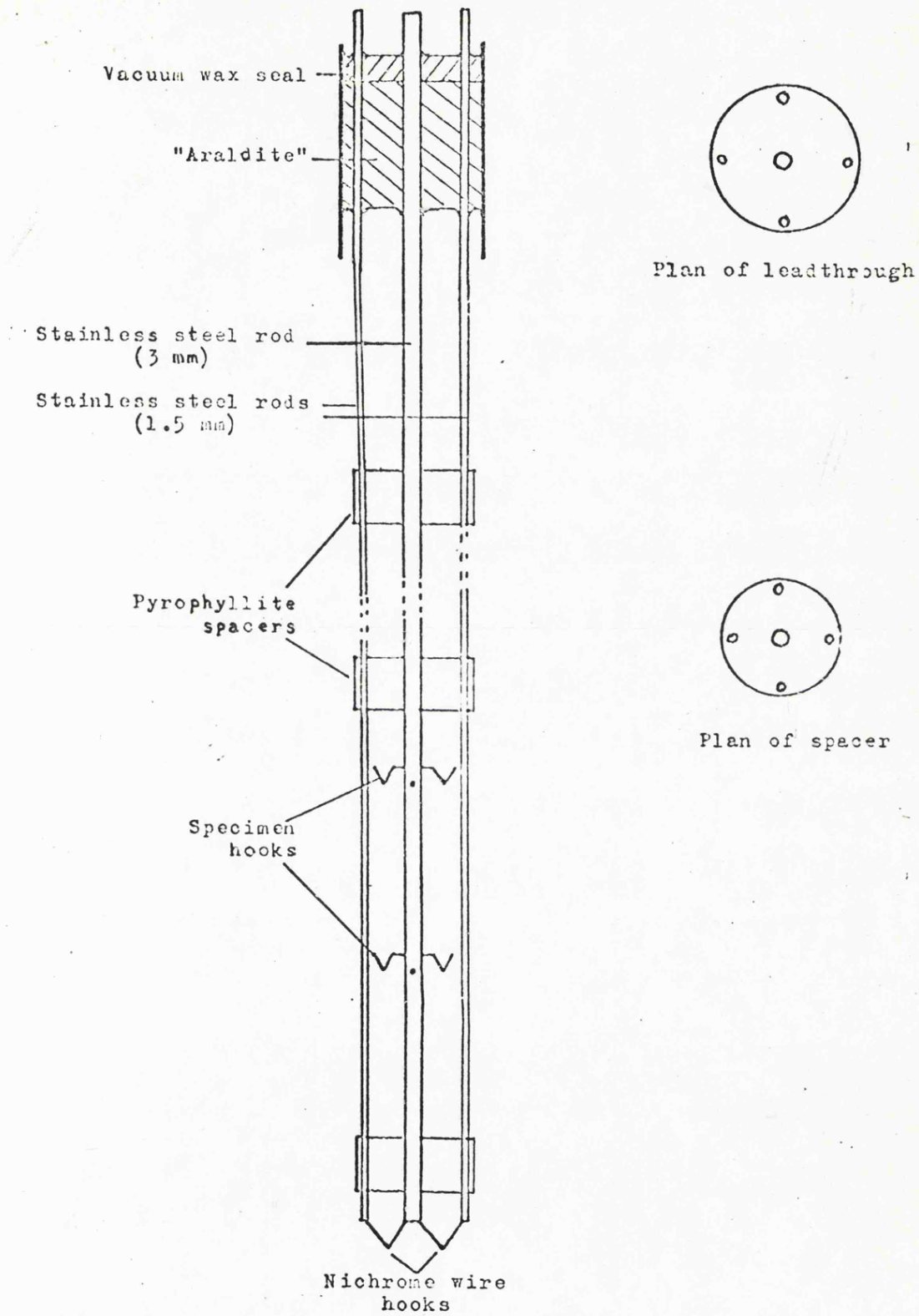

Fig. 2.5 Specimen holder for metallographic studies. Eight specimens may be accommodated on the specimen hooks and a further four may be suspended from the lower fusible nichrome hooks. These latter specimens may be removed during an oxidation experiment without perturbing the oxidation conditions of those remaining.

symmetrically surrounding a central $^{1}/_{8}$" rod mounted in Araldite and vacuum sealed with blackwax. This coaxial geometry was maintained by pyrophyllite insulating spacers at intervals along the rods. Twelve specimens could be accommodated, eight suspended from small hooks attached to the central support rod and the remaining four from short pieces of nichrome wire (32swg) spot welded from the central rod to the outer rods. Any of these four specimens could be removed individually from the reaction zone by passing a current of approximately 2.5A between the appropriate outer conductor and the central rod. This fused the suspension wire and allowed the specimen to fall through a ball valve (1" bore) into a pyrex collecting tube. After allowing the specimen to cool, the collecting tube was isolated from the reaction tube and the specimen removed. The pyrex tube was re-evacuated before reopening the ball valve. The other eight specimens could be removed at the end of the experiment after allowing the furnace to cool.

2.3.4 The microbalance

The microbalance used was a Sartorius model 4104 with a maximum sensitivity of 1μg; it is based on a design by T. Gast. The beam comprises two quartz tubes supported by a torsion band suspension. Deviations of the beam from its equilibrium position are detected electromagnetically and the derived error

signal is used to generate a current in a coil which acts to restore the beam to its original position. This current is thus proportional to the force acting on the beam and hence to the specimen weight. The balance is equiped with an automatic weight compensation mechanism such that when full scale deflection on the indicating meter is reached an electromagnetic force is applied to the beam to reset the meter at zero. In this way it is possible to expand the working range of the balance by a factor of 100 times without compromising its ability to resolve small weight changes. The balance output was continuously measured on a chart recorder running at constant speed. The balance head is enclosed in a massive stainless steel case to ensure good thermal stability.

2.4 Evaluation of the oxidation apparatus

Initial experiments with the apparatus were designed firstly to evaluate its performance and secondly to establish a suitable standard surface finish for specimens in the oxidation study. These experiments were carried out on the microbalance using a simple reaction tube of the type shown in Fig. 2.6a. The results showed that an excessive amount of noise was generated even at 400°C. For example the peak to peak noise level was $\sim$200μg, a figure which when compared with the weight gain of $\sim$500μg on the Fe-20% Cr alloy at 400°C after 16 hours exposure was obviously

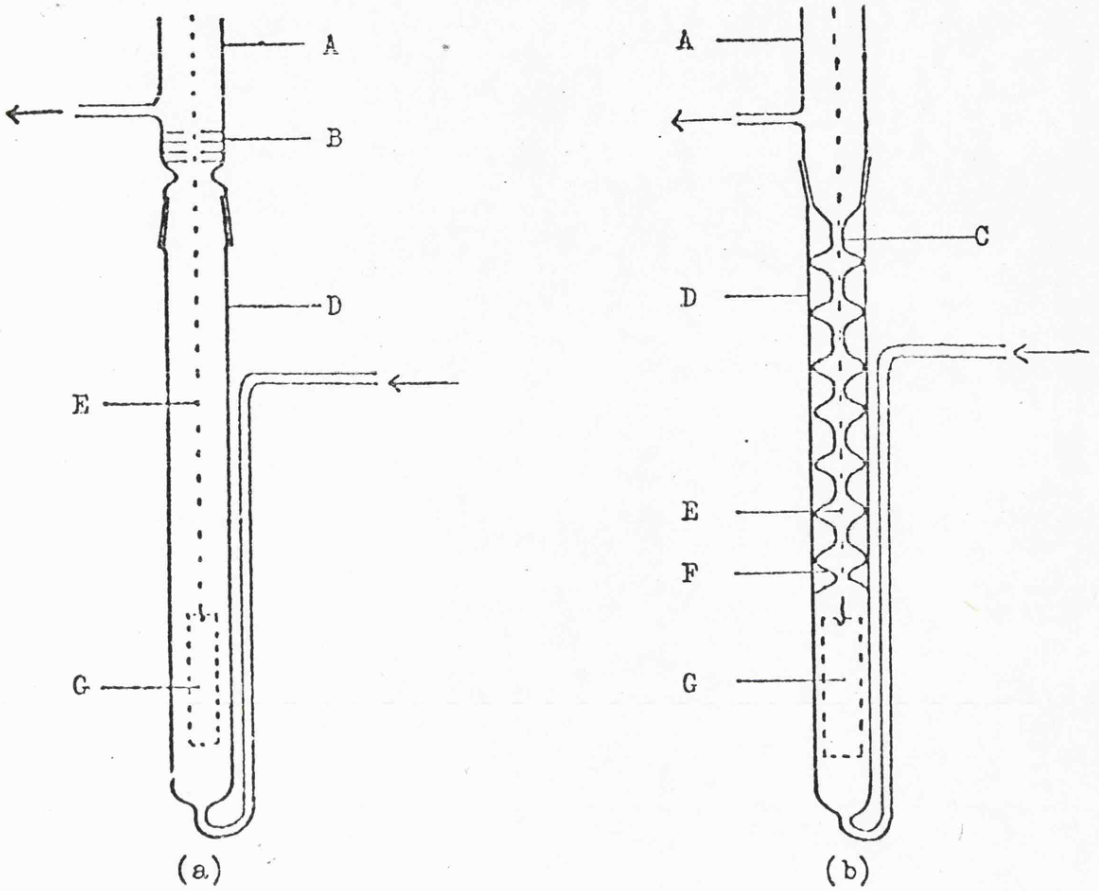

A - hangdown tube from microbalance (pyrex)
B - metal baffle system
C - graded glass seal
D - specimen tube (silica)
E - hangdown wire from microbalance (platinum)
F - silica baffle system
G - specimen

Fig.2.6 Diagram of specimen tube for microbalance
(a) Original specimen tube
(b) Modified specimen tube incorporating an efficient baffle system.

unsatisfactory. Since noise was negligible when the specimen was not heated or when it was removed from the microbalance suspension it was clearly due to convection turbulence in the hot zone. A number of unsuccessful attempts were made to reduce the noise to an acceptable level which involved altering the flowrates and inserting crude baffle systems. It was then found that purging the microbalance head with helium reduced the noise to $\sim 10\mu g$, presumably by inverting the unstable density gradient that caused the convection. An investigation of the important variables producing convection lead to a simple theory outlined in Appendix 1. On the basis of this analysis the baffle system illustrated in Fig. 2.6b was constructed which reduced the noise to an acceptable level of about $0.5\mu g$ at 400°C. Using the modified system a slow drift in the microbalance reading was then detected. This was caused by streamline convection currents in the tare tube due to the differential rate of heating (or cooling) of the various parts of the apparatus in response to changes in ambient temperature. The effect was eliminated by using a vacuum-jacketed, silvered tare tube to ensure that the counterweight and its surroundings were maintained in thermal equilibrium with the massive stainless steel balance case.

The oxidised specimens from these early tests at 400°C were found to be covered with two types of oxide. The bottom half of the specimen (the leading edge to the gas flow) was covered with a bright red oxide with a

velvety sheen which in the scanning electron microscope was seen to consist of myriads of small whiskers, Fig. 2.7. Reflection electron diffraction, Fig. 2.8, showed only the presence of α-M_2O_3 and since no chromium (<1%) was detected by electron probe micro-analysis, the whiskers were essentially haematite, α-Fe_2O_3. Transmission electron diffraction patterns from individual whiskers showed the whisker axis to be $[11\bar{2}0]$ in agreement with the observed arcing in the reflection pattern. The top half of the specimen was covered with a compact faceted cubic oxide which was shown to be a spinel. No whiskers were found on specimens oxidised at higher temperatures. Thermo-dynamic calculations show that α-Fe_2O_3 is unstable in a CO_2-1% CO atmosphere at 400°C, indicating that the oxygen partial pressure of the gas is higher than that predicted from the equilibrium

$$2\ CO_2 \rightleftharpoons 2\ CO + O_2$$

This together with the fact that whiskers were only formed on the leading edge of the specimen indicated that an appreciable amount of oxygen was present in the incoming gas. Further experiments showed that oxygen was diffusing into the system via plastic tubing used to connect the humidifier to the gas stream and after replacement with copper tubing the formation of whiskers was virtually surpressed. The presence of whiskers thus proved to be a fairly sensitive qualitative test of the oxygen impurity level of the gas stream.

Fig.2.7 Fe-5% Cr alloy oxidised at 400°C showing whisker oxide growth. Scanning electron micrograph, X 2500.

Fig.2.8 Reflection electron diffraction pattern from specimen oxidised as Fig.2.7.
Note pronounced arcing of rings indicating $\langle 11\bar{2}0 \rangle$ is normal to the specimen surface.

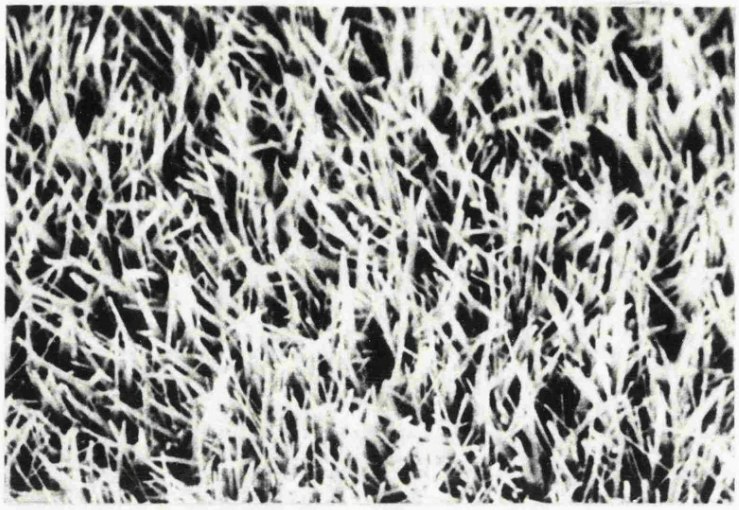

Fig. 2.7

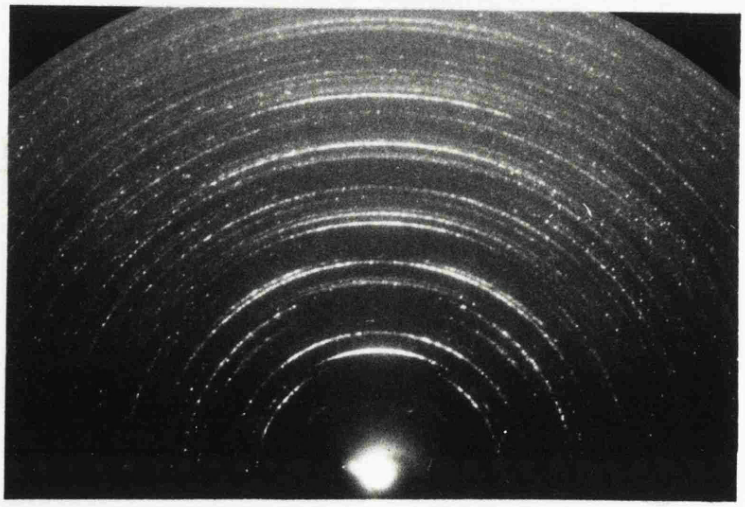

Fig. 2.8

2.5 Oxidation procedures

2.5.1 Microbalance experiments

After suitably preparing the surface (section 2.2) specimens were weighed on an analytical balance. They were then transferred to the microbalance, the reaction tube evacuated to $\sim 5 \times 10^{-5}$ torr (6.6×10^{-3} Nm^{-2}) and the cold furnace raised into position. The reaction tube was slowly heated taking care that the pressure never increased above 5×10^{-5} torr (6.6×10^{-3} Nm^{-2}) in order to minimise specimen oxidation by the out-gassing atmosphere. A small weight loss ($\sim 100\mu g$) from the specimens was usually noted during this operation. When the oxidation temperature was reached gas was admitted via a needle valve until the pressure was slightly greater than atmospheric. The outlet stop cock of the microbalance was then opened and the time was noted, this being taken as the start of the oxidation experiment. At the end of the experiment the furnace was lowered in order to cool the specimen rapidly, the specimen removed from the apparatus and reweighed on an analytical balance. The total weight gain calculated from the initial and final weighings was always within 0.1mg of the value obtained from the continuous microbalance record.

Some experiments were also carried out by raising the hot furnace at the desired oxidation temperature around the specimen suspended in the already flowing

gas. The reaction tube took about 3 minutes to reach the oxidation temperature under these conditions.

2.5.2 Oxidation of specimens in the metallographic furnace

The operations leading to the commencement of an oxidation run were essentially similar to those outlined in the first paragraph above. The specimens suspended from nichrome fuses were removed rapidly from the hot zone by blowing the fuse as described previously. The remaining specimens were allowed to cool slowly in the gas stream by switching off the furnace. The furnace took ∿10 hours to cool to room temperature and the oxidation time was arbitrarily assumed to have elapsed 1 hour after the furnace was switched off. In most experiments the metallographic specimens were weighed before and after oxidation and the weight gain compared with the microgravimetric record.

2.6 Examination of oxidised specimens

The morphology, composition and crystal structure of the oxidation products has been investigated using a variety of techniques on many types of specimens.

Most oxide scales formed on the alloy were layered structures and, while the outer surface may be examined easily, information from the lower layers in the oxide can only be gained by either sectioning or successive removal of the outer surface. Polished sections have

been prepared by a variety of techniques. Normal hot mounting in Bakelite or allyl phthalate resins was satisfactory for oxidised specimens when both oxide layers were fairly compact and had the advantage that very good contact between the specimen and mount were obtained. On more fragile specimens, where the oxide is porous and easily fragmented, methacrylate cold mounting resins or vacuum impregnation with a low viscosity polyester resin had to be employed. In these cold mounting processes and particularly with polyester resins considerable contraction occurs on curing causing the oxide to become detached from the metal. This effect can be avoided by mounting the specimen between mild steel plates and using iron filings as a filler for the resin. When an electrically conducting mount was required, as for electron probe microanalysis, sections were prepared using a silver-filled epoxy resin or solder. Mounted specimens were ground on successively finer grades of silicon carbide paper and polished using diamond impregnated cloths. Care was taken during grinding and polishing to maintain the specimen edge transverse to the direction of abrasion and to use the minimum possible load consistent with a reasonable rate of polishing. This was necessary to minimise "tear out" of the fragile and brittle oxide, and to prevent excessive rounding of the specimen edge. A few minutes on a vibratory polishing machine often

improved the surface finish. Sections were also prepared by fracturing the specimen at liquid nitrogen temperatures. Again this method worked well for compact oxides, but it failed for the more fragile oxides. On many specimens the outer oxide layer could be detached simply by lifting it carefully with a needle, an operation often assisted by first quenching the specimen in liquid nitrogen. The underlying oxide could then be readily studied using many techniques. The detached outer oxide could also be characterised in isolation. Characterisation of the oxide layer adjacent to the metal was accomplished by dissolving the metal in an anhydrous, saturated solution of iodine in methanol (Vernon, Wormwell and Nurse, 1944) and examining the detached film. It was unnecessary to completely dissolve the metal; once sufficient metal had been removed the oxide could be teased off with a needle. It was also possible to sample individual oxide layers observed on polished sections by making a scratch in the selected oxide layer using a microhardness indentor. The debris produced by the cutting action of the diamond indentor was then removed using a two stage extraction replica technique (Adams Silva and Spiers, 1960). The scratch mark is readily visible on the replica in the transmission electron microscope with the debris particles on either side. Particles may then be characterised by selected area electron diffraction. Extraction replicas have also

been used to study friable oxide layers and oxide surfaces with weakly adherent oxide particles, whiskers etc. attached.

The examination of thin oxide films $\lesssim$100nm is much more restricted, at least with the equipment available for the present study. Oxide surfaces may be examined either attached to the metal or after removal by dissolution of the substrate in an anhydrous, saturated solution of iodine in methanol. These stripped films may be picked up on electron microscope grids for examination. Extraction replicas taken from the outer surface have also been examined.

2.6.1 Optical microscopy

Using a low power stereomicroscope with oblique illumination the oxidised specimen surface was examined. This gave information on the gross surface topography of the specimens, the extent of lateral growth of different oxide phases and, on specimens with very thin oxide films, any variation in interference tint from one grain to another caused by differences in oxide thickness and optical properties. Many of the surfaces were very rough and studies were limited by the small depth of focus of the optical microscope restricting the magnification to a maximum of about X100 if all parts of the surface were to remain focussed.

Polished sections through the oxide scales were examined in a normal metallurgical microscope in both

the unetched condition and after various etching treatments. In the unetched condition image contrast derived mainly from the pore structure of the material and from polishing artefacts such as "tear out" of the brittle porous oxides. Some contrast from the various layers was also evident as colour variations. It was difficult to draw quantitative conclusions regarding the pore structure of the various layers due to artefacts although the total scale thickness and the relative thickness of the different layers could be estimated as well as grain boundary and internal oxidation effects. Taper sections were occasionally employed but gave unreliable results due to differential polishing of the various layers.

A number of different etchants were used, each selected to enhance a particular micro-structural feature. Etching in 50% hydrochloric acid in methylated spirit delineated the various scale layers by rapidly dissolving magnetite, Fe_3O_4, and leaving the iron-chromium mixed oxides, $(Fe, Cr)_3O_4$ and $(Fe, Cr)_2O_3$, and the metal relatively unattached. The grain structure of the underlying metal was best revealed using nital etch (5% nitric acid in methylated spirit) for the lower chromium alloys and a mixture 2.5% nitric acid and 7.5% hydrochloric acid in water was effective for the higher chromium alloys.

2.6.2 Scanning electron microscopy

In the scanning electron microscope (SEM) a fine electron beam ($\sim$10nm minimum spot diameter) is formed and is scanned across the specimen in a raster. The incident electrons interact with the specimen in several ways, electrons and electromagnetic radiation of various energies being emitted. Either the emitted radiations or the electrons absorbed may be used to form the image. Electrons leaving the specimen are detected using a scintillator and the resultant light signal passed down a light pipe to a photomultiplier. The photocurrent generated is used to modulate the intensity of an electron beam synchronously scanning a similar but larger raster on the fluorescent screen of a cathode ray tube. By controlling the current through the scanning coils in the electron optical column the area of the raster on the specimen surface may be altered. The magnification is simply the ratio of the raster dimensions on the display tube and on the specimen. The resolution is controlled by the spot size and the characteristics of the detected signal. A more detailed account of the SEM is given in Amerlinckx and Hearle, Sparrow and Cross (Booker, 1970, Hearle, Sparrow and Cross, 1972).

The SEM is most commonly used in the emissive mode which utilises secondary electrons. These have a low energy ($<$50eV) and hence originate very close to the

surface (<5nm), their small escape volume enabling a high spatial resolution to be achieved (≃10nm minimum). A positively-biased grid (+200V) in front of the scintillator is used to attract these low energy electrons into the detector. High energy electrons are hardly deviated by the low potential applied to the grid. This mode of operation has been extensively used in the present investigation, using Cambridge Instruments S2 and S4 Stereoscan instruments and a JEOL JXA 50A electron probe microanalyser, to study the detailed morphology of oxidised surfaces attached to the substrate as well as stripped and cleaved oxide surfaces. The high resolution enables small particles to be located and, since little or no specimen preparation is required, few artefacts are present. This is a great advantage of the technique over replica studies in the transmission electron microscope where it is often difficult to be certain that an observed feature is the result of the oxidation process or merely adventitious matter introduced during lengthy specimen preparation. Very little information on the crystal structure of fine particles can be obtained in the SEM however. In this study the SEM has been found extremely useful for locating features of interest prior to making detailed microstructural analysis using extraction replica techniques in the transmission electron microscope.

The emissive mode has also been used to study fracture sections through oxide scales. In this way

information on pore sizes, shapes and distribution may be obtained without the artefacts introduced by mechanical polishing procedures. Unfortunately, since accurately plane sections are not produced and because fracture always occurs along planes of weakness (such as a plane containing many voids) quantitative interpretation of void structure is impossible. Polished sections have also been studied in the SEM. Usually this examination was carried out in conjunction with electron probe microanalysis, using the X-ray detection systems on the Cambridge Instruments S2 and S4 and the JEOL JXA 50A. Information on composition variations in the specimens could be obtained using either the absorbed or the reflected electron image. In the former mode the beam induced current in the specimen is used to form the image while in the latter case high energy electrons reflected from the surface are utilised. The use of two reflected electron detectors mounted symmetrically at a high angle with respect to the specimen surface has been found to be particularly useful since the effect of surface topography may be minimised by using the sum of the signals from the two detectors or the effect of composition variations may be minimised by using the difference signal to form the image (Kimoto and Hashimoto, 1966). This facility for forming images showing essentially composition or topographic contrast is available on the JXA 50A electron probe microanalyser.

Extraction replicas and stripped oxide films have also been examined by forming images from electrons transmitted through the thin specimen. This scanning transmission electron microscopy (STEM) has several advantages over the conventional direct imaging electron microscope (DIEM). In the DIEM the electrons after interacting with the specimen have to be focused onto a screen to form the image. As the specimen thickness increases the amount of inelastic scattering of the beam by the specimen increases. The resultant large energy spread of the electrons transmitted reduces the resolution of the image formed due to chromatic aberrations in the final lenses. Furthermore because most of these scattered electrons are not used for forming the image a great loss of intensity results. In STEM these disadvantages are not present since there is no requirement for an electron lens after the specimen. There are other advantages to the STEM system: the high gain of the scintillator/photomultiplier type of detector fitted to the instrument enables images to be obtained using smaller beam currents and thicker specimens while the ability to process the signal (e.g. by non linear amplification, differentiation etc.) enables information to be extracted which is not always apparent in the images obtained in the DIEM. Three basic modes of STEM are available on the JXA 50A electron probe microanalyser. Firstly only the undeviated electrons from the incident beam may be

utilised resulting in contrast analogous to a normal bright field image of a DIEM. Secondly, a single diffracted beam may be used to produce an image similar to a normal dark field image in the conventional electron microscope. Thirdly, all the scattered radiation may be used to form an image. There is no direct counterpart of the latter type of image in the DIEM; it is particularly useful for studying thick specimens, since most of the electrons which are transmitted will have been inelastically scattered by the specimen. Interpretation of contrast obtained in this mode is sometimes difficult. In the present study it has been found that bright field STEM images may be produced at 50kV from specimens which are opaque to 100kV electrons in the DIEM.

2.6.3 Electron probe microanalysis

Electron probe microanalysis provides a means of obtaining chemical composition data from micro-volumes of material and has been usefully employed in a number of aspects of the present work. The electron optics of the electron probe microanalyser are basically similar to those of the scanning electron microscope (frequently the two instruments are combined as in the JXA-50A electron probe microanalyser) but here X-rays produced by electron bombardment are detected and analysed. The X-ray spectrum produced contains lines of discrete wavelength characteristic of the elements

within the exited volume superimposed on a background of continuous bremsstrahlung ("white") radiation. Analysis of the X-rays is usually achieved by crystal spectrometry (wave-length dispersion) or by pulse height analysis techniques (energy dispersion). The intensity of a characteristic X-ray line gives a measure of the concentration of the element in the exited volume. The technique may be used to study any element in the periodic table from beryllium upwards. The size of the electron spot on the specimen depends on the electron optics and the required beam currents. Beam currents commonly employed for microanalysis by crystal spectrometry are in the range 1-100nA which gives spot sizes typically between 0.1 and 2μm. Due to the higher efficiency of energy dispersive systems much lower beam currents (1pA-1nA) may be employed enabling spot sizes down to 10nm to be employed. The spatial resolution of electron probe microanalysis is determined in part by the electron spot size and also by the dimensions of the X-ray source which are determined by the extent of electron diffusion and the penetration of the exited X-rays (Anderson, 1967). Typically the X-ray source is ∿0.5μm but it may vary considerably depending on the element analysed, the beam potential, the substrate, the electron spot size etc. Detection sensitivity again depends on many factors; values of 100ppm have been reported in favourable cases. Qualitative analysis of specimens is performed by examination of

the X-ray spectrum and comparing the peak positions with those tabulated by the instrument manufacturer for each element. The spectrometer may then be set to a particular X-ray line for quantitative studies.

The electron probe may be positioned on a selected point on the specimen and the intensity of the line recorded using a scaler. The distribution of a given element along a line in the specimen surface may be determined by either translating the specimen mechanically beneath the static probe or by sweeping the probe across the surface using scanning coils located in the electron optical column, and monitoring the intensity of the X-ray signal on a rate meter. A two dimensional X-ray image may also be obtained by using the X-ray signal to modulate the intensity of a cathode ray tube display while the probe is scanned in a raster on the specimen surface.

Studies have been made of the distribution of alloying elements in sections through oxide scales on metals and the composition of particles and thin oxide films detached from the substrate by mechanical or chemical means (section 2.6) have been estimated. Sometimes it proved difficult or impossible to strip oxides from the metal surface, particularly when the substrate was very smooth. In some of these cases microanalysis was possible with the oxide attached to the metal. In order to improve the spatial resolution

soft X-ray spectra were used for the analysis, at low beam potentials to minimise electron penetration.

In general, X-ray intensities are not directly proportional tc the concentration of the emitting element. The electron and X-ray interaction processes taking place within the sample may give rise to significant X-ray absorbsion, fluorescence and atomic number effects which have to be taken into account in quantitative work. These effects together with proposed correction procedures have been discussed by many workers (Martin and Poole, 1969. Bishop, 1968).

However these effects are fairly small ($\sim$10% error) for the K lines of iron and chromium in the Fe-Cr-O system for take off angles $>20^{o}$ and at the commonly used beam potentials. Much of the raw X-ray intensity data on polished sections through the oxide scale has been converted to element concentrations simply by using the substrate metal as a reference standard and assuming a linear proportionality. This crude procedure works fairly well because either the chromium/iron ratio is similar in oxide and metal or the oxide is essentially iron oxide. Hence absorption and fluorescence corrections tend to be small and the largest source of error is due to the change in atomic number on going from the substrate to the oxide. The total errors are unlikely to exceed 5% relative for the beam energies normally used (15-25kV). In many cases

greater accuracy than this would have been unwarranted since the oxides were never smooth, compact and flat as required for accurate quantitative analysis. In a few instances where the data was obtained at high X-ray take off angles (which tends to minimise errors due to unfavourable surface topography) and with good counting statistics the more refined correction procedure of Ziebold and Ogilvie (Ziebold and Ogilvie, 1964) has been applied.

Electron probe microanalysis of stripped oxide films and extraction replicas is much more difficult than the examination of bulk specimens since thin specimens may be damaged by large incident beam currents. In addition the electron optical resolution must be sufficient to locate fine particles and other areas of interest. The use of low beam currents ($<$1nA) enables high resolution secondary electron images to be obtained and also minimises specimen damage but results in low X-ray count rates. Some compromise is necessary and the best working conditions vary from specimen to specimen and from instrument to instrument; generally specimen currents in the range 1-10nA were used. Some analysis was carried out on an AEI EMMA4 instrument (Cooke and Duncumb, 1968) which is a transmission electron microscope designed also for micro-analysis of thin specimens. Conversion of microanalysis data from thin films into specimen composition is complicated by the unknown fraction of electrons lost from the sample by transmission

and backscattering. This fraction is a function of the specimen thickness which will in general be unknown (at least on a localised scale). The technique adopted in the present study has been to measure chromium to iron ratios rather than attempt to determine absolute concentrations. Firstly a ratio was obtained from the measured CrK intensity from the thin specimen and a bulk chromium standard; a similar ratio was also determined using FeKα from the specimen and a pure iron bulk standard. Now for thin films, absorption and fluorescence corrections are usually negligible while for the pure metal standards the corrections are usually small. Hence the ratio of the two intensity quotients is to a first approximation the ratio of the concentrations of elements in the specimen. The result of this procedure is probably accurate to within $\sim$5% of the true concentration ratio. Further refinement of the correction procedure would be unwarranted since the statistical accuracy of the measured intensity ratios is often worse than this at the low count rates involved.

2.6.4 Reflection electron diffraction

Electron diffraction studies on oxidised metal have been carried out using a high resolution diffraction stage fitted tc a JEOL JEM 6A electron microscope. In this technique the electron optics are used to produce a fine beam of electrons which are brought to a

focus on the fluorescent viewing screen. The beam strikes the specimen at glancing incidence and the diffraction pattern produced is recorded on a photographic plate located beneath the screen. Due to the limited penetration of electrons through solids (several 100nm at 100kV) the glancing incidence technique provides diffraction patterns only from the immediate surface regions of the substrate. With a smooth specimen electron penetration may be limited to a depth of approximately 1nm, which makes the method ideally suited for studying thin oxide films and for assessing the quality of the metal substrate (perfection of single crystal surfaces, presence of mechanically deformed layers and contaminant films produced during preparation, etc.). It has been extremely valuable for investigating early stages of the oxidation process, particularly the growth of oriented oxides on single crystals of metal. With rougher specimen surfaces, as may be produced by etching the metal or by continued oxidation, the electron diffraction pattern is related mainly to the surface asperities projecting into the electron beam. Hence sensitivity to the presence of thin surface films is reduced but features such as enhanced grain boundary oxidation may be examined.

Identification of oxide phases was achieved by comparing d-spacing measurements from the ASTM powder diffraction file. Values of d-spacings were calculated

using the simple formula $d_{hkl} = \frac{\lambda L}{r_{hkl}}$ where r_{hkl} is the distance between the centre spot (000) and the diffracted position (hkl), L is the distance from the specimen to the photographic plate and λ is the electron wavelength (Andrews, Keown and Dyson, 1971). Errors involved in these measurements were usually less than 2% for r≈20mm. Orientation analysis of single crystal patterns was carried out using the reciprocal lattice/Ewald sphere construction (Andrews et al, 1971; Hirsch, Howie, Nicholson, Pashley and Whelan, 1965). The interpretation was confirmed by comparing observed interplanar angle with calculated values (Andrews et al, 1971) for the particular Bravais lattice.

2.6.5 Transmission electron microscopy

The transmission electron microscope is essentially analagous to the optical microscope except that an electron source replaces the light source and glass lenses are replaced by magnetic electron lenses. The principal advantage of using electrons is that their short wavelength (∿0.004nm at 100kV) enables a much higher resolution to be attained (typically ∿0.3nm for modern electron microscopes operating at 100kV). Since electrons interact very strongly with matter only very thin (<100nm) specimens may be examined in transmission. Detailed descriptions of the operation of the transmission electron microscope (TEM) and interpretation of

data have been given by Hirsch et al, 1965; Kay, 1965.

A complementary technique, selected area diffraction (SAD), is available on most electron microscopes. This facility may be used to characterise the crystal structures of small volumes of material located in the electron microscope image. In the present study an AEI EM802 has been used to analyse small particles <50nm diameter extracted from the specimen surface. Information obtained on stripped oxide films includes crystallite size and shape, phase identification and distributions in polyphase, structures, orientation relationships etc.

2.6.6 X-ray diffraction

Three X-ray methods have been used to study oxidised metal surfaces. Fragments of oxide detached from the metal surface may be ground and examined using ordinary X-ray powder photography. A Debye-Scherrer camera of 11.46cm diameter (Straumanis geometry) was used in these studies with either CrKα or CoKα radiations. Comparison of the observed d-spacings with the ASTM powder diffraction file was used for identifying the oxide phases. Accurate lattice constants were determined by plotting the apparent lattice parameter against the Nelson-Reilly function (Azaroff and Buerger, 1958)

$\frac{1}{2}\left(\frac{\cos^2\theta}{\sin\theta} + \frac{\cos^2\theta}{\theta}\right)$, where θ is the Bragg angle, and extrapolating to $\theta = \pi/2$. Information on the composition

of spinel solid solution could be obtained by comparison of the lattice parameter with published data (Yearian, Kortwright and Langenheim, 1954).

The second X-ray method used was the glancing-angle-edge-irradiated technique (Isherwood and Quinn 1967). Oxidised specimens were mounted in a Debye-Scherrer camera (5.73cm diameter, Straumanis geometry) with the specimen inclined 30°-45° to the X-ray beam so that only the edge of the specimen was irradiated. Sharp diffraction lines are produced by this technique and, since usually diffraction arcs at low and high angles may be observed on both sides of the beam collimator and the beam trap, the $\theta = 0$ and $\theta = \pi/2$ positions may be accurately established. This together with the use of the substrate metal as a calibration standard enables fairly accurate d-spacings to be deduced. The technique enabled small specimens to be examined and by removing successive layers from the substrate, the variation of specimen properties with depth could be studied. Additional information about the specimens could often be gained by close examination of the patterns. For example cobalt Kα radiation causes chromium to fluoresce but not iron. Hence if chromium is present in significant quantities within the X-ray penetration volume a high background on the film will be evident due to the fluorescent radiation. Spotty rings indicate a fairly large crystallite size (>10μm typically) in the specimen whilst line broadening

may be attributed to a number of factors including crystallite size, microstrains and composition gradients. Oxidised materials with a coarse grain structure (>100μm) often show many Laue spots from the substrate superimposed on the film. Deformation of the metal causes curvature of the diffracting crystal planes and this leads to an elongation of these Laue spots. Although this additional information is largely qualitative in nature it was often used to direct the course of subsequent investigations using more powerful techniques. Because of the large amount of information to be gained by the use of a glancing angle X-ray beam, most oxides of thicknesses greater than about 1μm were examined by this method.

A powder diffractometer has also been employed to study oxidised metal specimens. Again removal of successive layers provided a means for investigating variation of structure with depth. The diffractometer was equipped with an argon proportional counter and a pulse height analyser. Using this arrangement almost any incident X-radiation may be used since the effects of unwanted X-ray fluorescence in the specimen could be eliminated by suitable adjustment of the pulse height analyser. By choosing different energy radiations the depth of oxide sampled could be altered since penetration depth is a function of X-ray wavelength. For the diffractometer geometry it may be shown (Cullity, 1956) that 50% of the diffracted intensity occurs from a layer

of thickness $\frac{0.69\ \mathrm{Sin}\theta}{2\mu}$, where θ is the Bragg angle, and μ is the mass absorption coefficient of the substrate. It can be seen that the sampled depth depends on μ and θ and it will be a maximum for a given specimen when $\mathrm{Sin}\theta = 1$. Typical values of $\frac{0.69}{2\mu}$ for the common crystallographic X-radiations in iron are given below:

Radiation	CrK	CoK	CuK	MoK
t 50% max. μm	3.9	7.5	1.4	11.6

Hence CuK is the most useful for thin films while thick scales are best examined using MoKα X-rays. In the present work oxide films as thin as 100nm have been detected. The presence of diffractions from the substrate was sometimes a useful indication that the whole of the oxide film was being sampled. MoKα radiation has not been used in the diffractometer method since the argon proportional counter is very inefficient for this wavelength.

CHAPTER 3

EXPERIMENTAL RESULTS

3.1 Oxidation kinetics

The observed oxidation kinetics for the whole range of alloys investigated may be divided into two types of behaviour related to alloy composition.

Alloys belonging to the first group (5, 9 and 12% Cr) showed an initial region in which the oxidation rate approximated to a linear rate law

$$w = k't$$

This linear region was of comparatively short duration ($\sim$10 hours). The oxidation rate soon began to decrease with increasing scale thickness, the rate eventually approximating closely to the parabolic rate law

$$w^2 = k''t$$

This behaviour was typical of the lower chromium alloys at all temperatures. Fig. 3.1 shows the weight gain-time curve of an Fe-5% Cr alloy oxidised at 600°C characteristic of this type of oxidation. The transition from linear to parabolic kinetics did not occur after a reproduceable time or weight gain.

Alloys containing larger amounts of chromium (15 and 20% Cr) exhibited a more complex kinetic behaviour. After an initial rapid weight gain the oxidation rate decreased markedly with time until the thickness of oxide was sufficient to give interference colours. The reaction

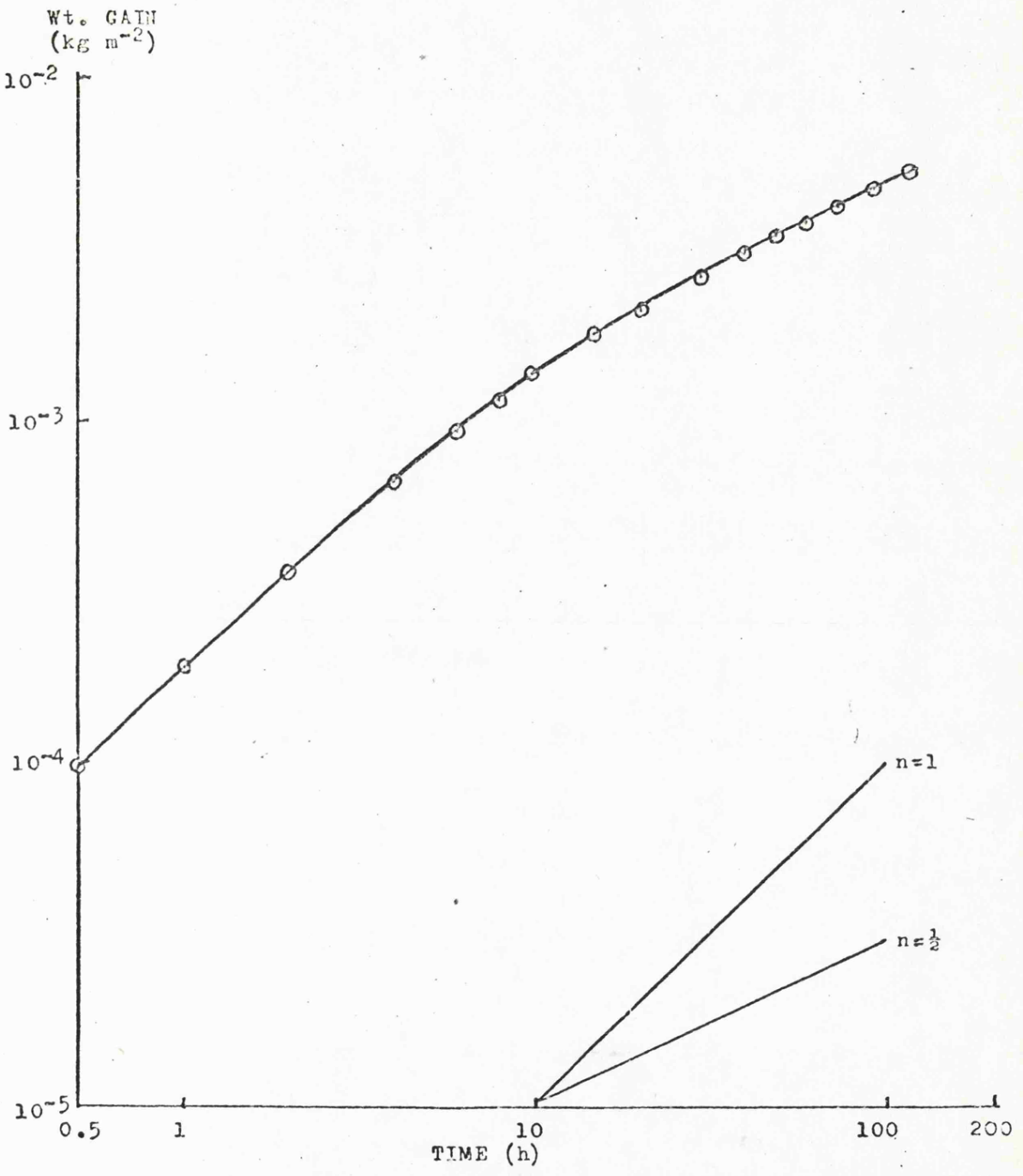

Fig.3.1 Weight gain vs time curve for typical Fe-5% Cr alloy oxidised at 500°C. Note the slow transition from linear to parabolic oxidation kinetics.

subsequently proceeded very slowly (too slow to permit accurate weight gain data to be obtained) and then increased rapidly with time according to a rate law of the form

$$w = k''' t^n \quad \text{where} \quad n > 2$$

During this period of increasing oxidation rate, thick oxide nucleated on the initial thin film and grew until it covered the entire surface. Once coverage of the surface by this thicker oxide was complete the kinetics became parabolic. The time required for the onset of parabolic oxidation was very variable; a range of times from 0.5 - 150 hours was recorded for several specimens of the same alloy. Fig. 3.2, the weight gain vs. time curve for a 15% Cr alloys at 600°C is typical of this kinetic behaviour. The three regions discussed above will be referred to as the primary, transitional and secondary oxidation stages in this investigation and are designated I, II and III in Fig. 3.2. Some specimens gave a stepwise transition from the primary to the secondary stages, see Fig. 3.3. Note that these steps occur at roughly equal weight gain intervals.

A complete summary of the kinetic data for the whole alloy series at 400°C, 500°C and 600°C is given in Tables 3.1a - 3.1c, respectively. It should be noted that the final parabolic oxidation constants for all the alloys are very similar for any given temperature and that they closely parallel the parabolic rate constants for pure iron. Experiments on pure iron were performed at one

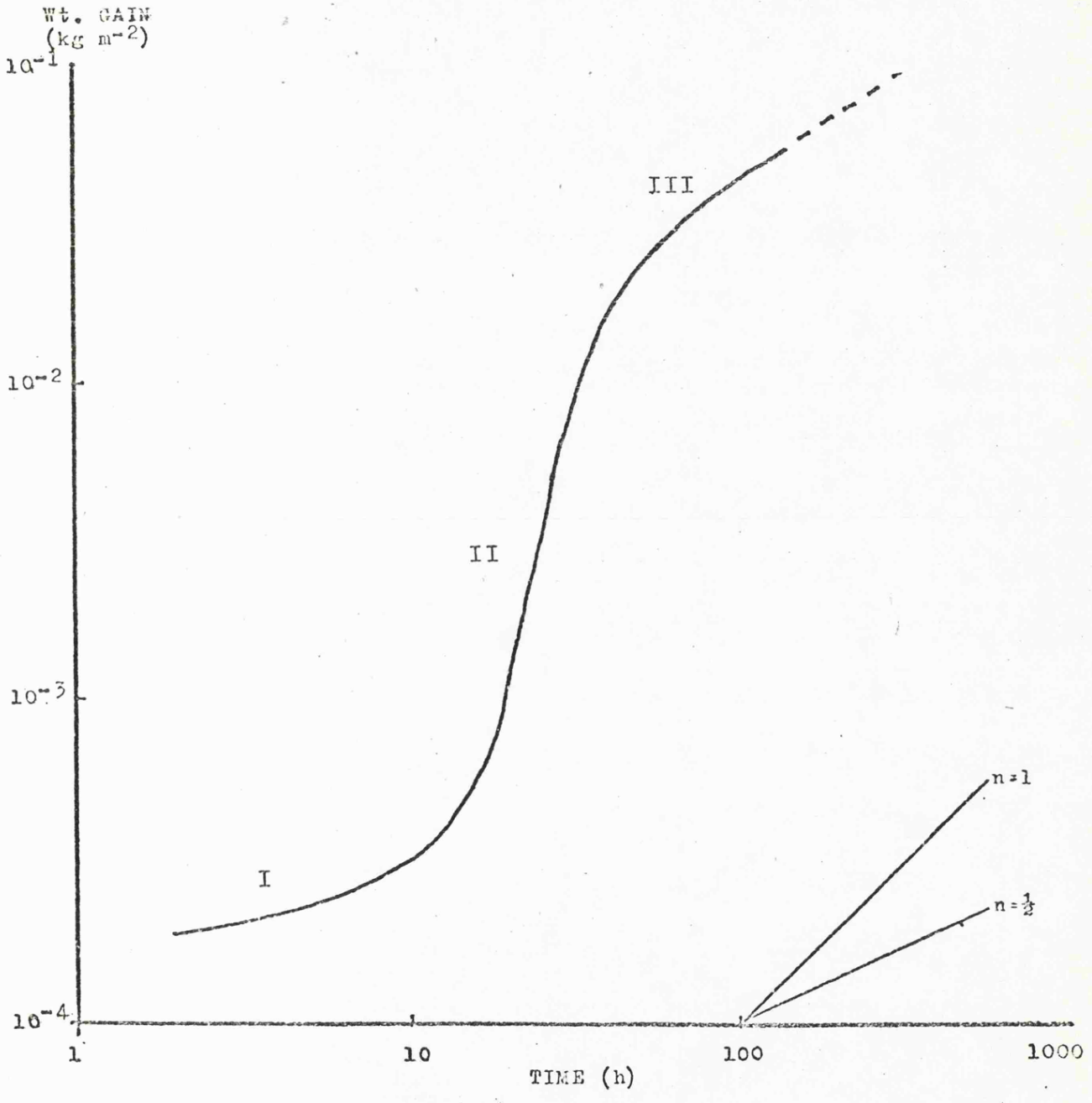

Fig.3.2 Weight gain vs time curve for typical Fe-15% Cr alloy at 600°C. Note the three separate types of kinetic behaviour: type I the primary oxidation stage, type II the transitional oxidation stage, and type III the secondary oxidation stage.

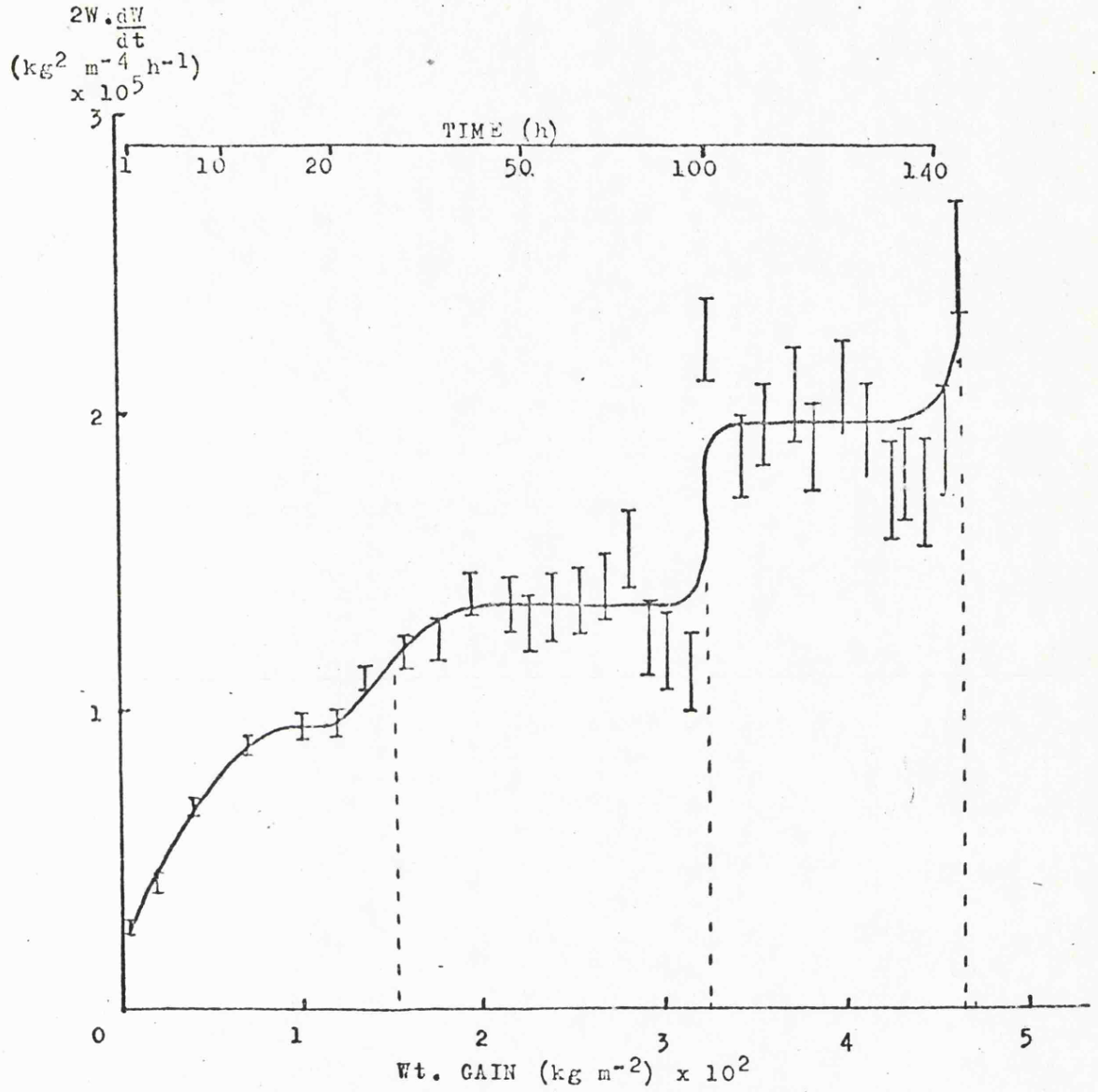

Fig.3.3 Plot of the instantaneous parabolic rate constant $2W\frac{dW}{dt}$ vs weight gain for an Fe-20% Cr alloy oxidised at 600°C. Note the change in behaviour occurs at equal weight gain increments.

TABLE 3.1 - Summary of kinetic results for Fe-Cr alloys

(a) 400°C results:

Cr in alloy (wt %)	Parabolic rate constant $kg^2\ m^{-4}\ sec^{-1} \times 10^{10} \pm 0.3$	Comments
0	1.1	No linear to parabolic transition observed
5	0.7	
9	0.9	
12	-	Variable - not parabolic
15	-	) Not parabolic oxide
20	-	) thickness tends to a) limiting value 1000A

(b) 500°C results:

Cr in alloy (wt %)	Parabolic rate constant $kg^2\ m^{-4}\ sec^{-1} \times 10^{9} \pm 0.5$	Comments
5	1.5	
9	1.2	
12	1.1	
15	-	) Variable -
20	-	) not parabolic

(c) 600°C results:

Cr in alloy (wt %)	Parabolic rate constant $kg^2\ m^{-4}\ sec^{-1} \times 10^{8} \pm 0.3$	Comments
5	1.2	
9	0.9	
12	0.7	
15	0.7	) Primary oxidation may
20	1.2	) occur for several hrs.

temperature only, 400°C, and it was interesting to note that no initial linear region was observed, parabolic kinetics being obeyed from the start of the oxidation. A plot of the log. parabolic rate constant for all alloy compositions versus the reciprocal temperature is given in Fig. 3.4. It can be seen that the points for each temperature studied lie close to a straight line. The activation energy calculated from the slope of this line was found to be 120 kJ $mole^{-1}$.

3.2 Observations of the structure of oxidised specimens

In the previous section it was shown that the oxidation kinetics of iron-chromium alloys may, in general, be divided into three stages, each stage being associated with a different characteristic reaction rate which was dependent on temperature. Microstructural examination of the oxidised specimens showed that the nature of the solid oxidation products could also be related to the three oxidation stages. In this section the microstructure of the oxide formed at the three temperatures studied (400°C, 500°C and 600°C) will be described for each alloy in turn. In some cases it has proved convenient to group together information on several alloy compositions and to describe in detail the behaviour of a single alloy in that group together with important distinctions between this alloy and the remainder of the group.

The general survey of etched Fe-Cr alloys is followed

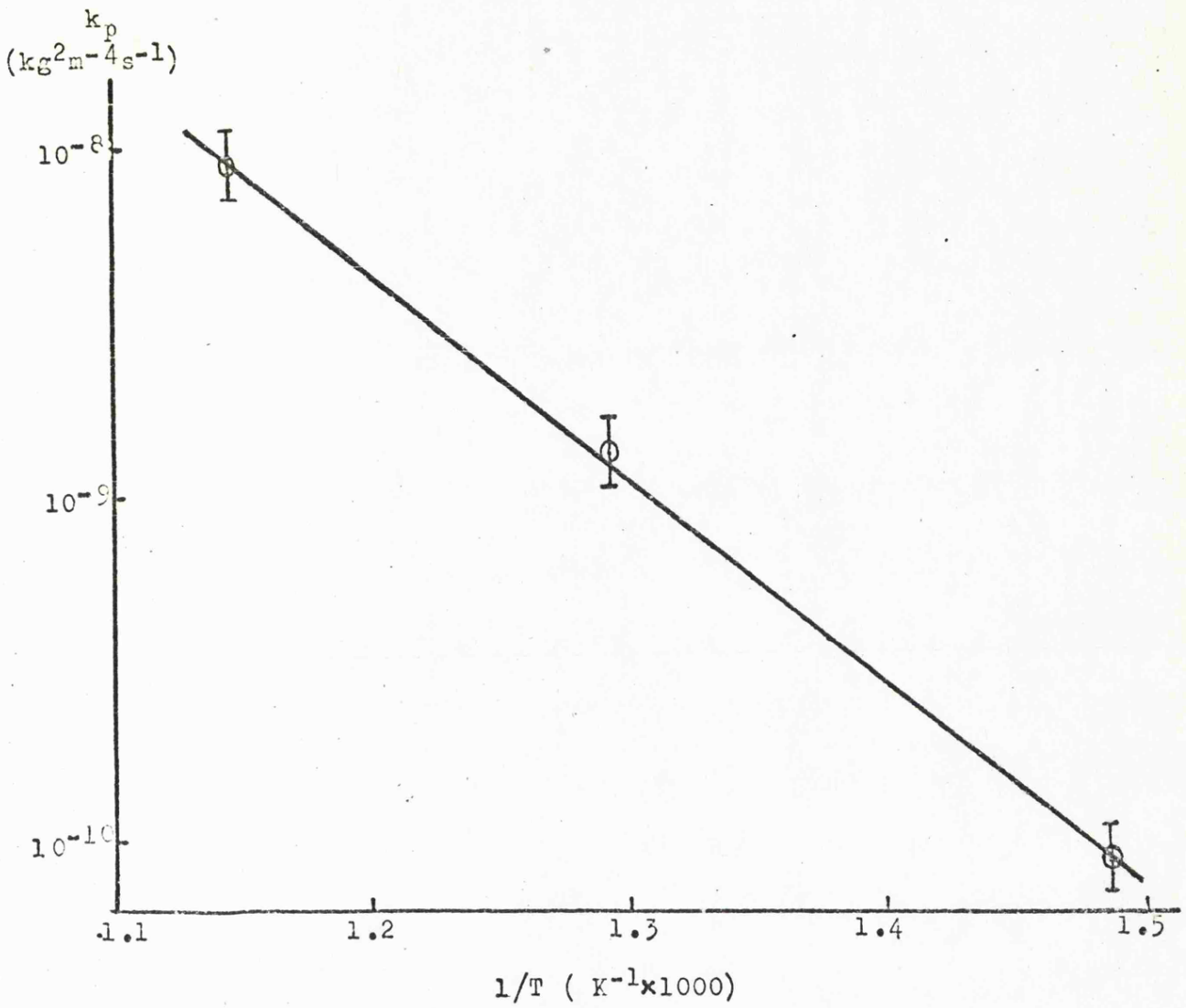

Fig.3.4 Plot of log kp vs $^1/_T$ for secondary oxidation.

by some observations of the effect of specimen thickness on the oxide scale morphology; this part of the study has been carried out on the Fe-9% Cr alloy. The final section is concerned with studied on alloy single crystals of Fe-15% Cr and Fe-70% Cr composition oxidised for times up to 2 hours, the main interest here being in the structure and growth sequence of thin oxide films formed during the early stages of reaction.

3.3 Etched polycrystalline specimens oxidised at 600°C

3.3.1 Fe-5% Cr alloy

Scanning electron microscopy showed that after the initial oxidation period the outer surface of the oxidised specimens was rough and faceted, Fig. 3.5.

An optical micrograph of a polished section cut perpendicular to the specimen surface is shown in Fig. 3.6. A two-layer oxide is clearly revealed containing coarse pores in the outer layer concentrated at the oxide-oxide interface. The two layers were of comparable thickness. The inner layer was also porous and the pores were elongated parallel to the specimen surface. Some evidence of grain-boundary penetration of the oxide was apparent.

Fracture sections examined in the SEM showed that the two oxide layers were readily detached from one another and from the substrate metal. Scratches on the substrate surface introduced by abrasion of a normal

etched surface prior to oxidation were found replicated at the oxide-oxide interface, Fig. 3.7a. The inner layer, Fig. 3.7b, consisted of several regularly spaced lamellae separated by fine pores.

Glancing angle X-ray diffraction patterns from the oxidised metal specimens could be indexed on the basis of a spinel structure. Mechanical removal of the outer oxide layer enabled similar X-ray studies to be carried on the inner layer, the patterns containing diffractions from a spinel structure together with diffractions from the alloy substrate. Element profiles through the oxide scale were measured using the microanalysis attachment of a Stereoscan S2 SEM. Using Fe Kα and Cr Kα X-radiations the chromium was shown, Fig. 3.8a and Fig. 3.8b, to be segregated in the inner layer. The distribution of chromium in the inner layer was uniform and comparison of the X-ray emission intensities from both the oxide and the substrate gave a value of 7.5 wt % Cr in the inner layer.

The apparent low chromium content of the outer layer decreasing from the oxide-oxide interface may be due to a fluorescence effect, or smearing during specimen preparation.

3.3.2 Fe-9% Cr and Fe-12% Cr alloys

After 120 hours oxidation the outer surface of the Fe-9% Cr alloy was faceted in a similar manner to the oxidised Fe-5% Cr alloy.

Fig.3.5 Fe-5% Cr alloy oxidised at 600°C. Outer surface. Scanning electron micrograph X 5500.

Fig.3.6 Section through oxidised Fe-5% Cr alloy showing large pores in both inner and outer oxide layers. Note elongation of pore in inner layer. Optical micrographs X 550.

Fig.3.7 Fracture sections through oxide scale. Scanning electron micrographs. Note (a) polishing marks on inner oxide surface X 300 and (b) lamellar structure of inner oxide associated with pores X 1300.

Fig.3.8 Section through oxide scale. Scanning electron micrographs X 600 with superimposed X-ray line scans along X Y for (a) iron and (b) chromium. Note particularly the depletion of chromium in the outer oxide.

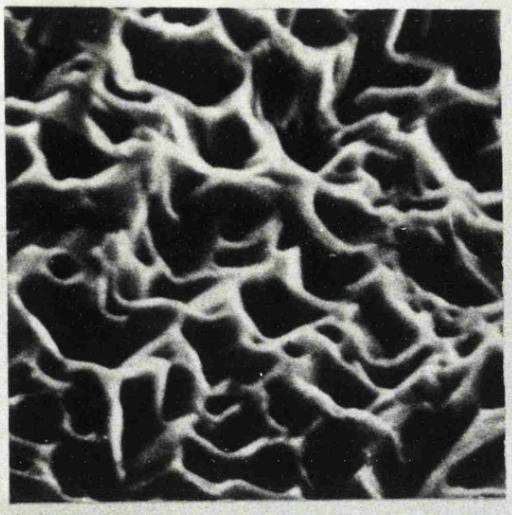

Fig. 3.5

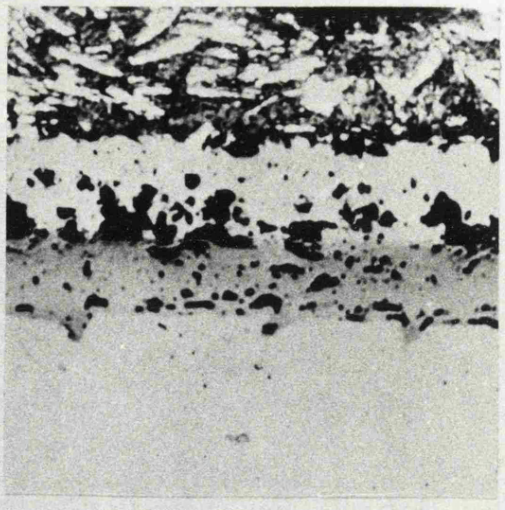

Fig. 3.6

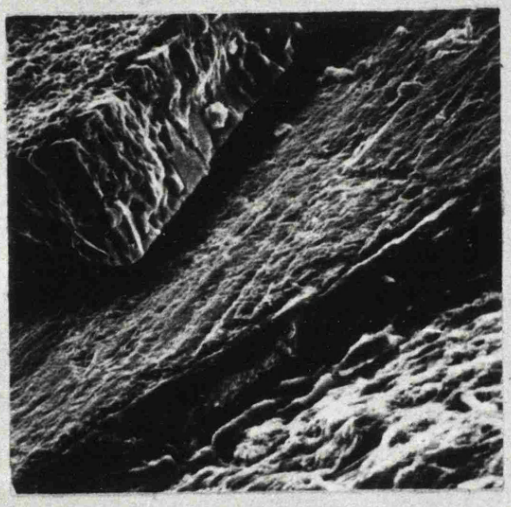

Fig. 3.7(a)

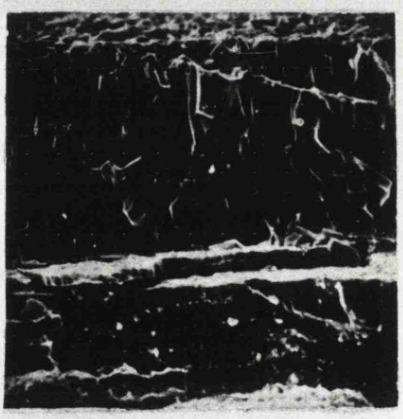

Fig. 3.7(b)

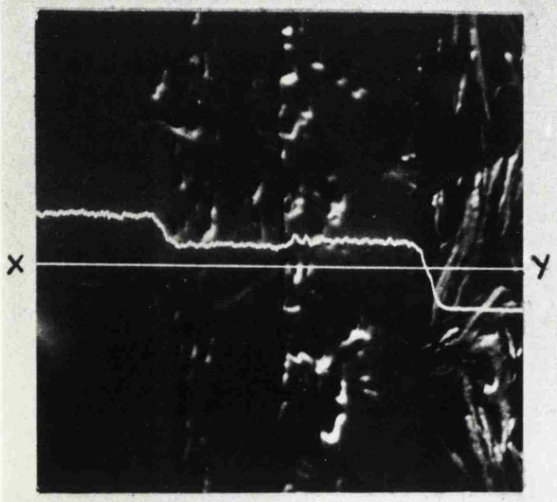

Fig. 3.8(a)

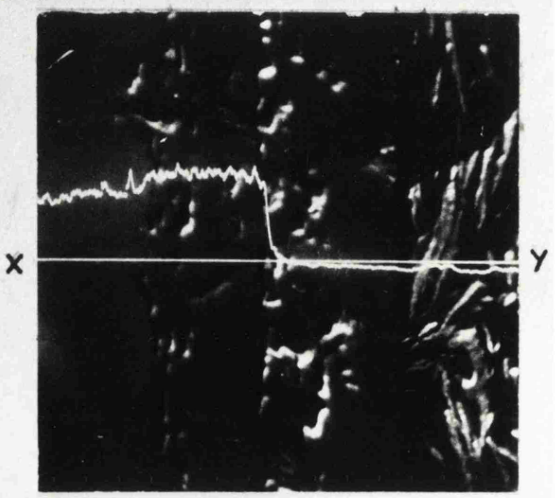

Fig. 3.8(b)

Glancing-angle X-ray diffraction from the as-oxidised surface of an Fe-9% alloy showed that spinel oxide was present, the sharpness of the diffraction lines indicating that the oxide was of uniform composition, stress free and of particle size $>2000\text{Å}$. The outer oxide was hard and brittle and it was readily detached to reveal a friable, brown-coloured underlying oxide layer which "ghosted" the grain structure of the underlying metal. X-ray diffraction studies from the inner layer also indicated the presence of a spinel oxide. Considerable line broadening in the back-reflection region was evident together with some diffractions from the underlying metal substrate. The X-ray film appeared fogged when compared with the pattern obtained from the outer layer; this was associated with a high chromium content in the inner layer which fluoresced when excited by the incident Co Kα radiation used in this work.

Extraction replicas were prepared from the exposed inner oxide layer and examined in the transmission electron microscope. The extracted particles were mostly rods of diameter $<1000\text{A}$, the fine particle size explaining the observed X-ray line broadening. Rods several μm in length were occasionally found aligned together in clusters but most were much shorter, $\sim 1\,\mu$m in length. Selected area electron diffraction showed that the filamentary microcrystals had a spinel structure with [111] parallel to the rod axis. In addition small ($<500\text{A}$) platelets were present most of which could not be identified

positively by SAD. A few patterns could be indexed on the basis of a carbide structure of the type M_7C_3 although since only one orientation was observed the identification must be regarded as tentative. Electron probe micro-analysis showed that the chromium distribution in the scale was similar to that observed on previous specimens although the concentration of chromium in the inner layer was higher. Careful measurements indicated a chromium content of 13 wt % in the inner layer on the Fe-9% Cr alloy as compared with the corresponding value of 7.5 wt % for the Fe-5% Cr alloy.

A sequence of optical micrographs taken from polished sections through the Fe-9% Cr alloy after different oxidation times are shown in Fig. 3.9a-e. It can be seen that initially the oxide forms in patches on the metal surface and then spreads laterally, eventually forming a continuous duplex layer. The two layer structure is apparent even after only 30 minutes growth. A complementary series of X-ray diffraction patterns from these specimens showed that a rhombohedral phase was present together with spinel in the early stages but with increasing coverage of the surface by the duplex layer, the rhombohedral phase disappeared. Even in the initial stages ($<$30 minutes) the rhombohedral oxide was only a minor component of the scale compared with the spinel phase.

After 50 hours oxidation, a regularly spaced lamella void structure was formed within the inner layer, more

Fig.3.9 Sections through oxidised Fe-9% Cr alloy. Optical micrographs X 500.

(a) Oxidation time 0.5 hr. Note duplex structure al already starting to form.

(b) Oxidation time 20 hrs. Note absence in porosity from inner scale.

(c) Oxidation time 45 hrs. Note porosity in inner layer.

(d) Oxidation time 53 hrs. Note detachment of oxide from metal.

(e) Oxidation time 142 hrs. Note lamellar pore distribution in inner layer.

(f) As (e) but etched. Note internal oxidation layer in the metal.

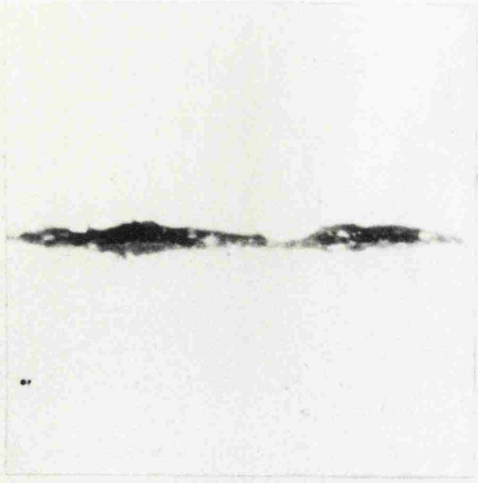

Fig. 3.9(a)

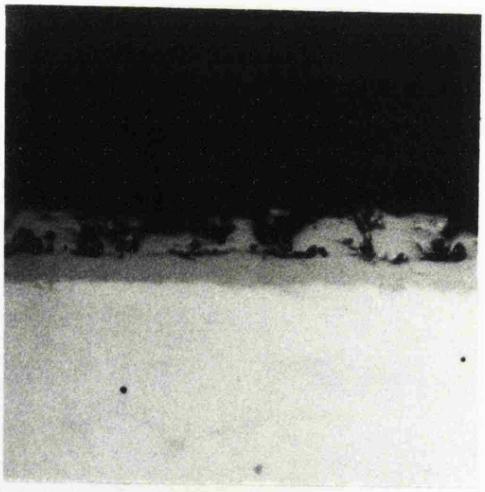

Fig. 3.9(b)

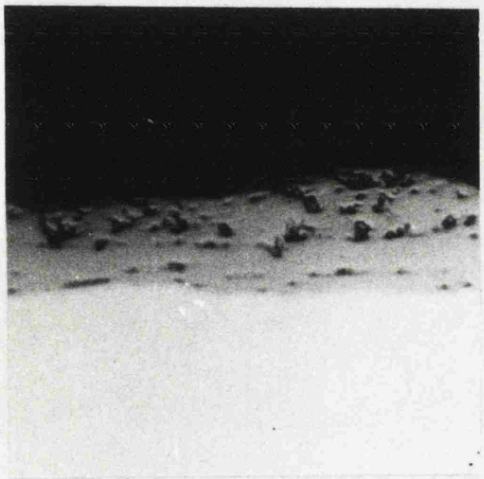

Fig. 3.9(c)

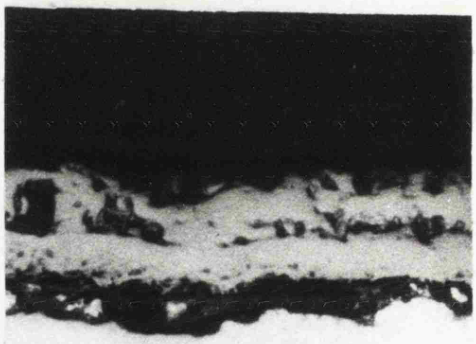

Fig. 3.9(d)

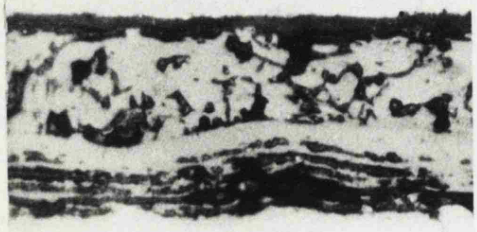

Fig. 3.9(e)

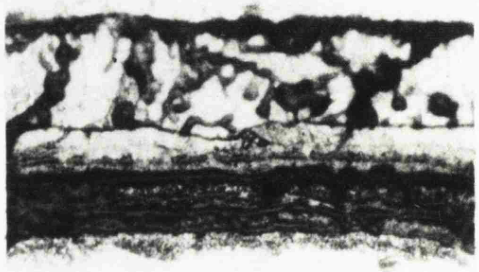

Fig. 3.9(f)

pronounced than that formed on the Fe-5% Cr alloy. Transverse cracks through the scale were occasionally observed which may be due to thermal stresses developed during cooling. A narrow zone of internal oxidation was apparent in the metal adjacent to the oxide, Fig. 3.9f, after etching the section in 50% hydrochloric acid in methylated spirit.

The Fe-12% Cr alloy behaved in an entirely analogous fashion to the Fe-9% Cr alloy. The measured chromium content of the inner layer was found to be 18% and the internal oxide zone was more extensive for this alloy.

3.3.3 Fe-15% Cr alloy

Specimens oxidised under these conditions exhibited very variable kinetic behaviour, often showing a very prolonged primary oxidation stage (up to 100 hours). After the transitional stage the final parabolic rate constant ($0.7 \times 10^{-12} kg^2\ m^{-4}\ sec^{-1}$) was similar to that of other compositions at this temperature (see Table 3.1).

During the primary oxidation stage the specimens were covered with a thin film of variable thickness as shown by the variation of the interference colours from one grain to another. Reflection electron diffraction from the oxidised surface showed the presence of a rhombohedral phase of the type α-M_2O_3. Scanning electron microscopy of oxidised specimens removed from the furnace during the transitional stage of oxidation, Fig. 3.10a, clearly indicated that the oxide growth was non-uniform.

The thicker oxide areas appeared to grow preferentially in regions close to grain boundaries and its surface morphology closely resembled that observed on the lower chromium alloys when covered by the duplex scale. The oxide nuclei may be seen, Fig. 3.10b, to form at the tips of asperities on the etched substrate.

The oxide films were chemically stripped and the underside of the oxide flakes examined in the SEM. The thin areas clearly replicate the original etched structure of the metal substrate, Fig. 3.10c, while in thicker areas a nodular type growth habit was evident. Examination of these thin films in the transmission electron microscope by selected area electron diffraction indicated that the crystal structure of thin areas was rhombohedral α-M_2O_3. Single crystals of thin oxide often extended over large areas, of the order of the metal grain size, and contained sub-boundary networks. Some evidence of the tetragonal phase γ-M_2O_3 was also found. In thicker areas spinel oxide was identified; a typical pattern from these areas is shown in Fig. 3.11a together with its indexed diagram, Fig. 3.11b. Analysis of a large number of diffraction patterns established the following crystal orientation relationships between the different oxide phases.

$$(0001)_{M_2O_3} // (111)_{M_3O_4} \quad \text{and} \quad [10\bar{1}0]_{M_2O_3} // [0\bar{1}1]_{M_3O_4}$$

As oxidation proceeded a small fraction of the spinel oxide nuclei grew laterally and thickened; polished

sections, Fig. 3.12, showed the typical duplex oxide structure in the thicker spinel regions. The oxide-oxide interface is clearly seen to be located at the position of the original metal surface as inferred previously from the surface marker studies on the Fe-5% Cr alloy, see Fig. 3.7a. The absence of lamella voids in the inner layer was typical of specimens with a low surface coverage of spinel. Eventually as oxidation continued the entire surface was covered with a continuous spinel film and from this point in time, the kinetics obeyed a parabolic rate law.

Specimens examined during the secondary oxidation stage showed the development of lamella voids in the inner layer. Also noticeable was a marked increase in the extent of the internal oxidation zone. Microanalysis of the oxide scale gave a value of 23% for the chromium content of the inner layer, the outer layer being magnetite, Fe_3O_4.

3.3.4 Fe-20% Cr alloy

The general structure and morphology of the oxide growth during the primary and transitional oxidation was similar to the oxidation products on the Fe-15% Cr alloy, a marked variability of the primary oxidation period again being found. During the transitional period two features were located on the specimen surface not found on other oxidised alloys. Firstly, near grain boundaries clusters of spherical particles $<5\mu m$ diameter

Fig.3.10 Fe-15% Cr alloy oxidised at 600°C. Scanning electron micrographs. Note (a) the non uniform growth of oxide on the surface X 75, (b) the preferential nucleation of oxide at asperites X 1000. The underside of the stripped oxide film (C) shows the finer structure of the inwardly growing oxide X 500.

Fog.3.11 Fe-15% Cr alloy oxidised at 600°C. Transmission electron diffraction pattern from stripped oxide film. (a) typical diffraction pattern and (b) indexed diagram of this pattern showing orientation relationship found between α-M_2O_3 and Fe_3O_4. o represents a diffraction from Fe_3O_4 and x represents a diffraction from the α-M_2O_3.

Fig.3.12 Section through oxide formed on Fe-15% Cr alloy at 600°C. Optical micrograph X 350. Note that the oxide-oxide interface corresponds to the original metal surface.

Fig. 3.10(a)

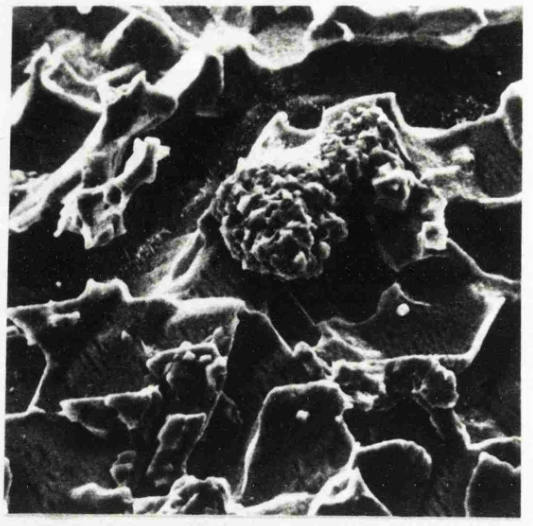

Fig. 3.10(b)

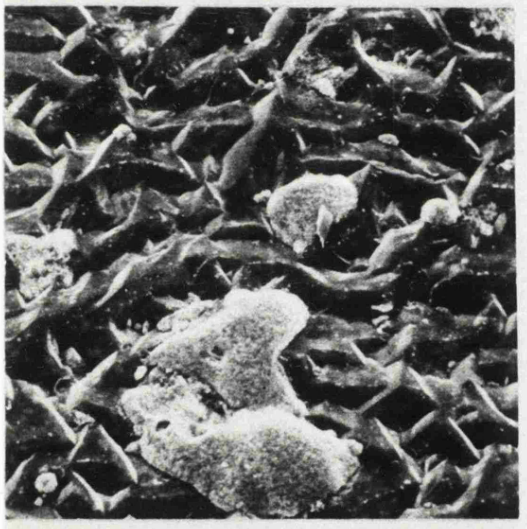

Fig. 3.10(c)

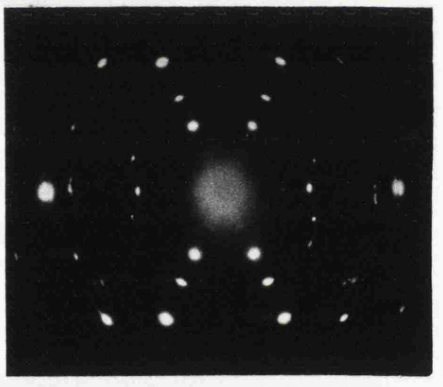

Fig. 3.11(a)

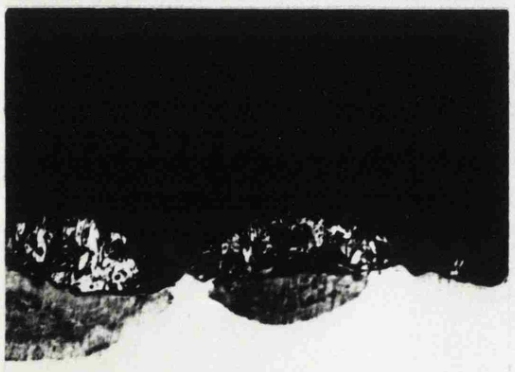

Fig. 3.12

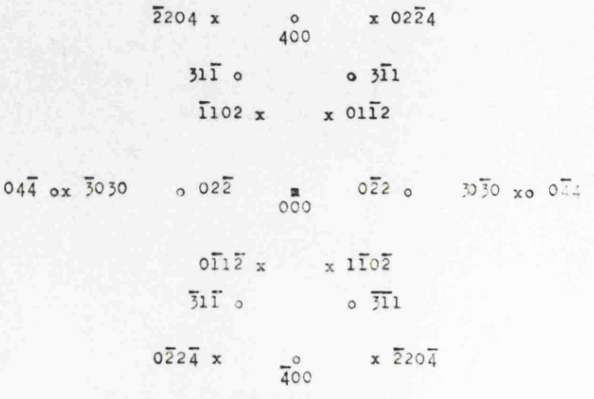

Fig. 3.11(b)

were found, Fig. 3.13. Secondly, whisker particles were located within the grain boundary groove, Fig. 3.14. Both types of particles were extracted from the surface using a replica technique and examined in the transmission electron microscope. The whiskers were found to have a rhombohedral structure with $[11\bar{2}0]$ parallel to the whisker axis. The spherical particles were however too opaque to 100 keV electrons to record a diffraction pattern. These particles were therefore examined in a high voltage electron microscope using 1 MeV electrons but again no diffraction patterns could be obtained, from which it was concluded that these particles must be amorphous. This lack of crystallinity is consistent with the high electron absorption and the spherical growth habit of the particles. Both types of particles were examined in an EMMA-4 instrument and analysis of the data showed that the grain-boundary whiskers were chromium rich and that the spherical particles contained little or no chromium but were rich in iron. Further microanalysis using a JXA 50A instrument showed that the spherical particles contained oxygen.

The structure developed during the secondary stage of oxidation of this alloy was significantly different from those described previously. Scanning electron microscopy showed that the surface of the oxide scale had a faceted surface similar to specimens of other compositions. Polished sections examined under the optical microscope, Fig. 3.15a, showed a two-layer scale with a very porous

outer layer. The inner layer was very compact and featureless and the interface with the metal was smooth except for the occasional step which was shown, by etching, to be associated with grain boundaries in the metal. A fine structure in the inner layer could just be resolved in the optical microscope, Fig. 3.15b. Examination of polished sections in the SEM using the reflective mode, Fig. 3.16, showed the presence of three layers. The outer layer ($\sim$15μm thick) was porous, particularly at the oxide-oxide interface; beneath this was a thinner ($\sim$5μm thick) intermediate layer of fine-grained oxide and adjacent to the metal was another thick ($\sim$11μm thick) layer. Removal of successive layers of oxide followed by X-ray diffraction examination showed only spinel was present. The innermost layer was very adherent and could not be removed mechanically or chemically from the metal. It was therefore sampled using the scratch technique outlined earlier (Section 2.6). Oxide debris from this scratched layer was examined in the transmission electron microscope and shown by SAD to be a mixture of oxide and metal. To confirm this conclusion accurate microanalysis across the oxide section was performed by point counting at 2μm intervals using a Microscan 5 instrument. The high X-ray take off angle of this instrument (75°) minimises the effects of specimen topography and the results obtained were corrected using the procedure of Ziebold and Ogilvie for absorption, fluorescence and atomic number effects. The corrected results are shown in Fig. 3.17.

Fig.3.13 Fe-20% Cr alloy oxidised at 600°C.
Note spherical particles often associated with grain boundaries. Scanning electron micrograph X 2000.

Fig.3.14 Fe-20% Cr alloy oxidised at 600°C.
The area shown corresponds to a grain boundary groove in the metal. Note the fine whisker-like particles. Scanning electron micrograph X 5000.

Fig.3.15 Section through Fe-20% Cr alloy oxidised at 600°C. (a) Optical micrograph X 1000.
Note the very porous outer layer. The inner layer (grey band to the right of the outer oxide) is slightly out of focus.
(b) Optical micrograph X 2500 of inner scale layer. Note the fine granular appearance.

Fig.3.16 Section through Fe-20% Cr alloy oxidised at 600°C. Note the three layer scale.
Scanning electron micrograph (reflective mode) X 1800.

Fig. 3.13

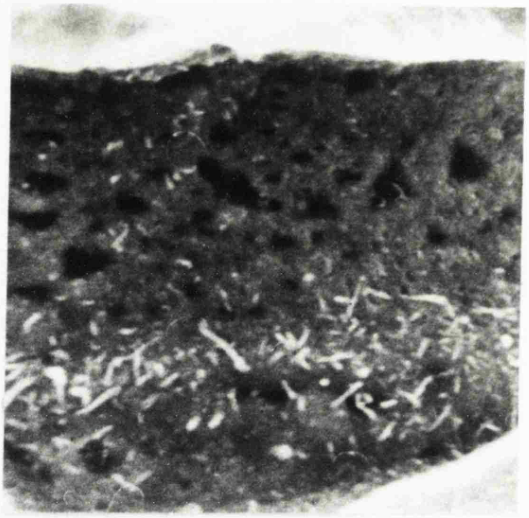

Fig. 3.14

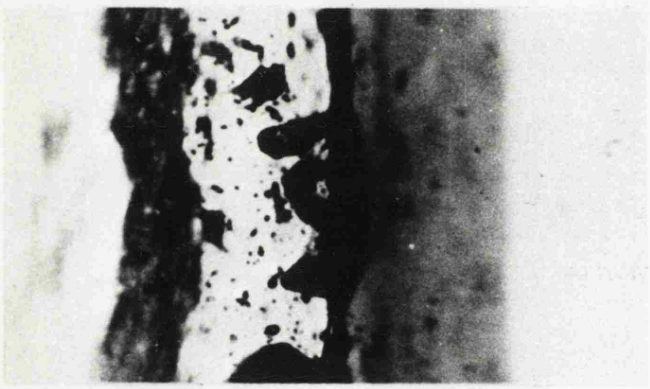

Fig. 3.15(a)

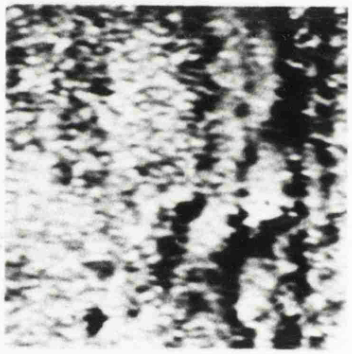

Fig. 3.15(b)

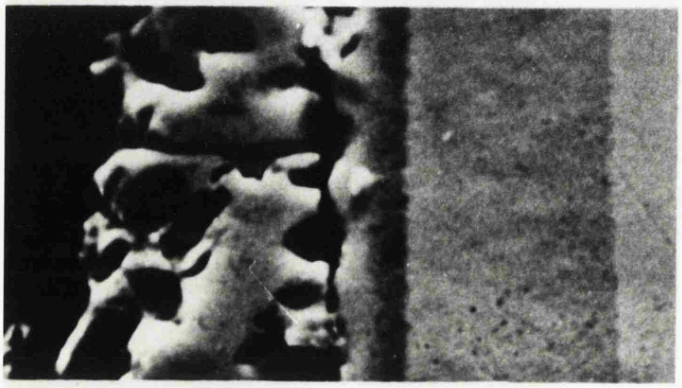

Fig. 3.16

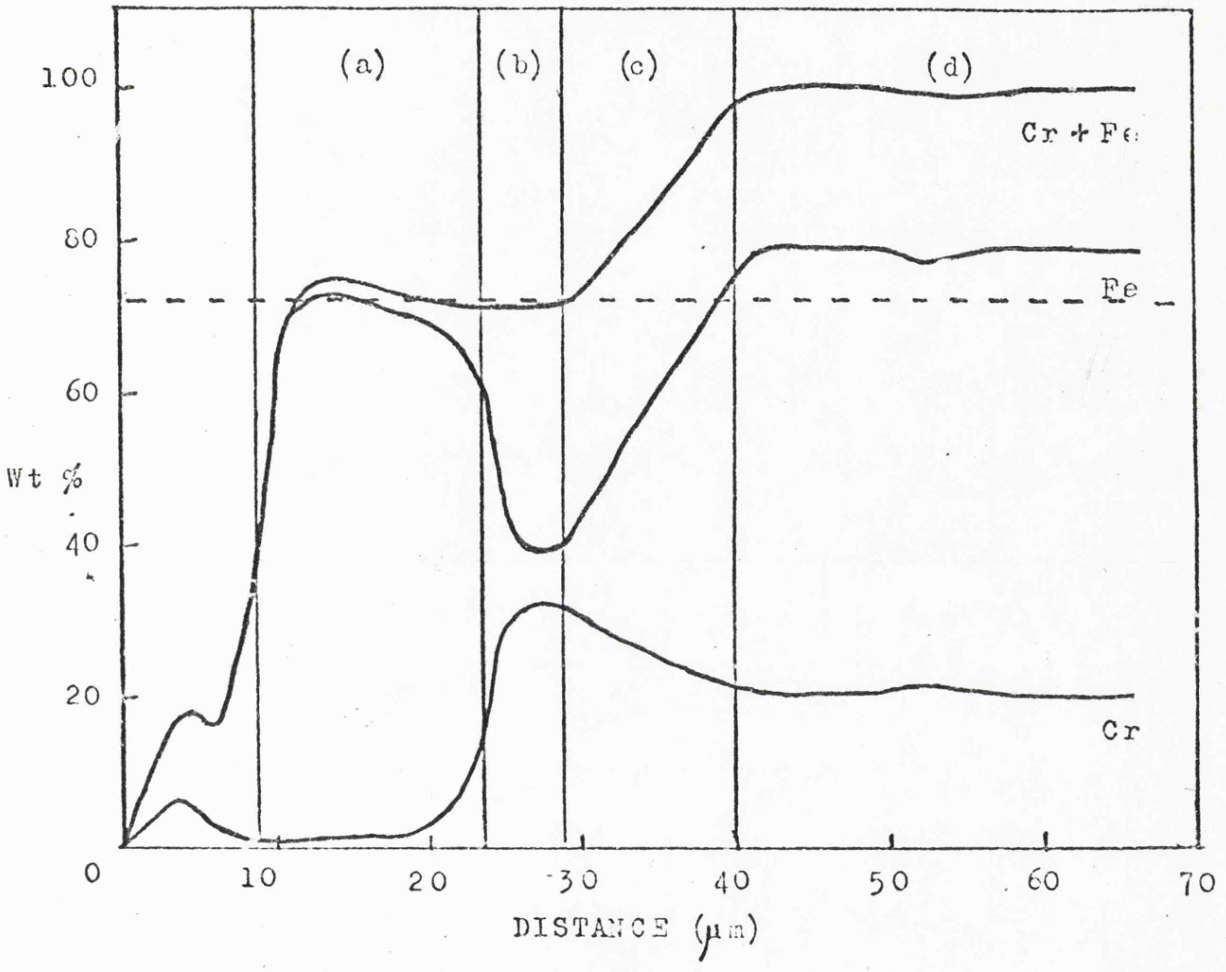

Fig.3.17 Corrected electron probe microanalysis data for an Fe-20% Cr alloy oxidised at 600°C. Regions (a), (b), (c), (d) correspond to the outer oxide, inner oxide, internal oxide and alloy respectively. The dotted line indicates the approximate metal composition (Fe + Cr) of $(Fe, Cr)_3O_4$ spinels.

The outer oxide is virtually chromium-free (the small amount of chromium detected may be due to the iron radiation emitted in the outer layer exciting the nearby chromium rich layer; a more complete discussion of these fluorescent effects has been given by Reed and Long, (1963). The intermediate layer is chromium rich (Cr = 32 wt %) and the total metal content of the oxide corresponds closely to the theoretical value (≃72 wt %) for iron-chromium spinel. In the innermost layer the total metal content increases in a linear fashion from 72 wt % at the intermediate oxide-innermost oxide interface to 100 wt % in agreement with diffraction results from the sampled layer. This innermost layer is clearly an extensive zone of internal oxidation.

3.4 Etched polycrystalline specimens oxidised at 500°C

3.4.1 Fe-5% Cr and Fe-9% Cr alloys

Scanning electron microscopy of specimens oxidised at 500°C showed a similar surface topography to that found on samples oxidised at 600°C although the roughness of the oxide surface was on a finer scale. A taper section, Fig. 3.18, through the oxide again showed a duplex scale structure with some porosity in both layers. A scanning electron micrograph, Fig. 3.19, taken from fracture sections shows clearly that the porosity is concentrated at the oxide-oxide interface. The inner oxide layer is somewhat thinner than the outer layer at this stage of the oxidation (100 hours) although

Fig.3.18 Taper section (≃ 4:1) through Fe-5% Cr alloy oxidised at 500°C. Optical micrograph X 1000.

Fig.3.19 Fracture section through Fe-5% alloy oxidised at 500°C showing porosity at the oxide-oxide interface. Note the shape of these voids. Scanning electron micrograph X 4500.

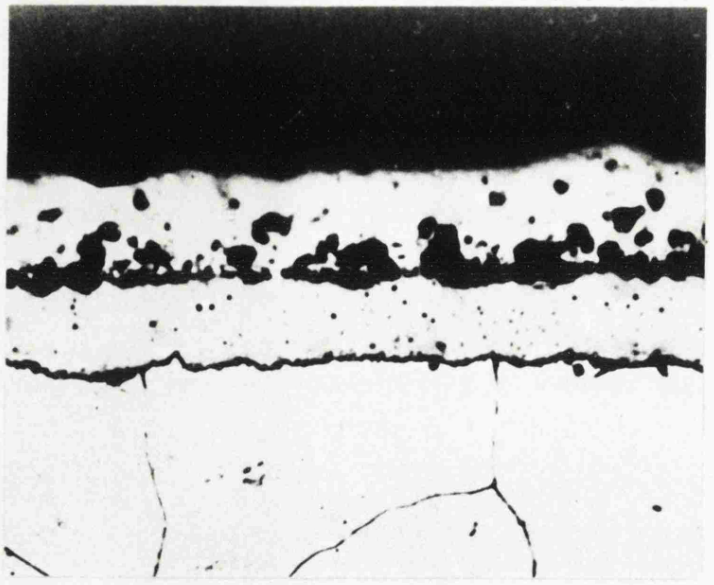

Fig. 3.18

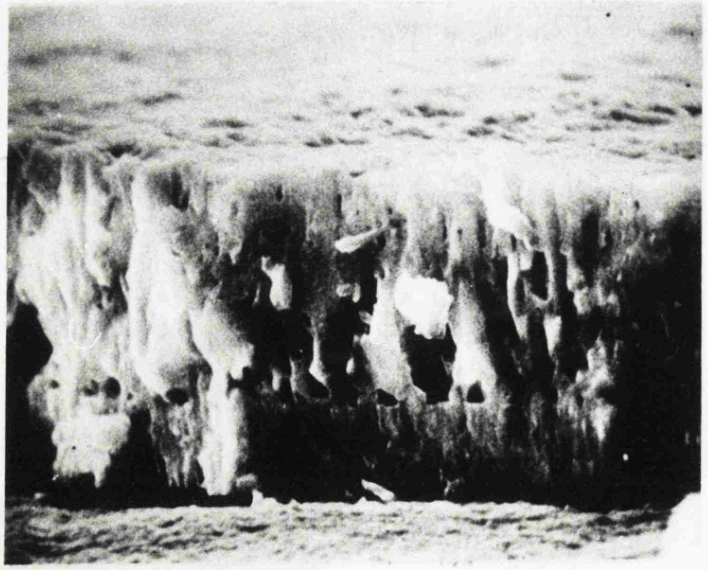

Fig. 3.19

with continued oxide growth their thicknesses tended to become equal. Electron probe microanalysis through the polished taper section showed that the inner layer is enriched in chromium compared with the metal and that the outer layer is virtually pure iron oxide, but due to the thinness of the oxide layers quantitative information could not be obtained. X-ray diffraction studies showed only the presence of spinel oxide.

3.4.2 Fe-12% Cr, Fe-15% Cr and Fe-20% Cr alloys

Oxidation of these specimens occurred very rapidly up to a film thickness of 0.3μm, subsequent oxidation proceeding extremely slowly, <5 μg/hr. Reflection electron diffraction from the oxidised surfaces gave patterns which could be indexed on the basis of spinel oxide. Electron diffraction analysis in the transmission electron microscope of films chemically stripped from the substrate metal showed that finely-polycrystalline and randomly-oriented rhombohedral oxide covered most of the surface. Some areas of spinel oxide were found which were also finely polycrystalline and showed no marked texture.

3.5 Polycrystalline specimens oxidised at 400°C

3.5.1 Fe-5% Cr and Fe-9% Cr alloys

The oxidised specimens had a similar surface topography to 5% and 9% Cr alloys oxidised at 500°C. A polished taper section through the oxide scale formed on

the Fe-5% Cr alloy showed the scale to consist of a single oxide layer, Fig. 3.20a, with a columnar growth habit, Fig. 3.20b. X-ray diffraction studies carried out with the oxide layer attached to the metal showed only spinel was present. Flakes of oxide mechanically detached from the metal were examined on both sides in a scanning electron microscope with a microanalysis attachment and were shown to contain virtually no chromium ($<0.5\%$). Examination of the substrate metal with some pieces of scale still attached confirmed that no chromium was present in the scale; in areas where the scale was absent, however, the chromium concentrate was found to be higher than that from the unoxidised metal used as a standard. Fig. 3.21 shows a Cr Kα line scan across an oxide flake resting on the substrate. This enhanced chromium content in the substrate was attributed to either the presence of a thin chromium-rich rhombohedral layer or to enrichment of chromium in the metal phase. To decide between these two possibilities the substrate was scraped clean of the spinel layer, lightly polished on a 1μm diamond impregnated cloth for a few seconds to remove any protruding particles and thoroughly cleaned. Reflection electron diffraction of the surface showed the presence of a rhombohedral phase of the type α-M_2O_3 indicating that a layer of chromium-rich rhombohedral oxide had formed between metal and spinel. This layer was not visible on a taper section in the optical microscope, Fig. 3.22. Since diffractions from the metal were also present in the

pattern the rhombohedral oxide was either very thin or dispersed in an internal oxidation layer. The spotty nature of the observed diffraction arcs, however, is considered more consistent with the former interpretation since internal oxidation layers observed at higher temperatures were very fine grained.

3.5.2 Fe-12% Cr, Fe-15% Cr and Fe-20% Cr alloys

These alloys oxidised rapidly at first to form thin oxide layers exhibiting interference colours. Subsequent oxidation was then very slow < 5 ug hr^{-1} Optical microscopy revealed colour differences from grain to grain, indicating some dependence of the growth kinetics and/or optical properties of the film upon the crystallographic orientation of the substrate.

Reflection electron diffraction patterns from different parts of the Fe-20% Cr specimen surfaces showed the presence of both spinel and rhombohedral oxide phases, most patterns, however, conforming to the former structure. Using next the glancing angle X-ray technique Laue spots together with diffraction lines from the metal were observed but no oxide was detected. Since unoxidised specimens gave only Laue spots due to the large grain size of the material (of the order of several hundred microns) the presence of ferrite lines indicated a reduction of grain size in the surface regions. No such reduction was apparent under the optical microscope possibly because it was beyond the resolution of this technique.

Oxide flakes chemically stripped from the substrate tended to curl into tight rolls indicating a stress gradient within the oxide film. Examination in the transmission electron microscope showed the very fine grained nature of the oxide, Fig. 3.23. Selected area electron diffraction confirmed the presence of both rhombohedral and spinel oxide, the latter existing as patches on the substrate surface. The mean grain size was less than 1000A. The small amount of oxide present together with the X-ray line broadening associated with the fine particle size probably accounts for the absence of any oxide lines in the X-ray diffraction pattern.

Electron probe microanalysis of the stripped films indicated that the Cr/Fe ratio was approximately 2:1 on the Fe-20% Cr alloy. However, the specimens tended to disintegrate under the electron beam, which made analysis very difficult and would account for the wide scatter of the results $\pm$ 100%.

Similar results showing chromium enrichment in the oxide film were obtained on the other alloys although scatter in the microanalysis data prevented determination of significant differences in film composition.

3.6 Further observations on lamella void formation and the effect of specimen thickness

The presence of sheets of oxide separated by voids was a common feature of all continuous duplex oxide scale structures formed upon specimens oxidised at 600°C.

Fig.3.20(a) Taper section ($\sim$ 6:1) through Fe-5% alloy oxidised at 400°c. Note apparent absence of inner layer. Optical micrograph X 500.

Fig.3.20(b) As (a): fracture section. Note columnar habit of scale. Scanning electron micrograph X 16000.

Fig.3.21 Fe-Cr alloy oxidised at 400°C. Flake of oxide lying on substrate. Scanning electron micrograph with superimposed chromium K line scan X 50. Note depletion of chromium in the oxide flake.

Fig.3.22 Taper section ($\sim$10:1) of metal-oxide interface. Optical micrograph X 1500.

Fig.3.23 Oxide film stripped from oxidised Fe-20% Cr alloy oxidised at 400°C. Note non-uniform growth. Transmission electron micrograph X 40000.

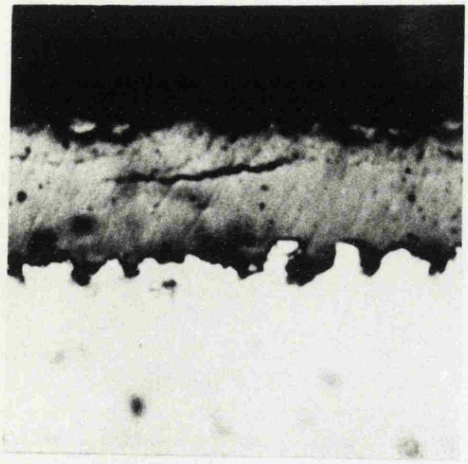

Fig. 3.20(a)

Fig. 3.20(b)

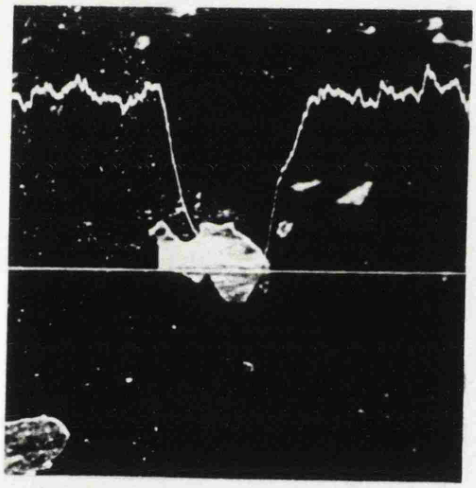

Fig. 3.21

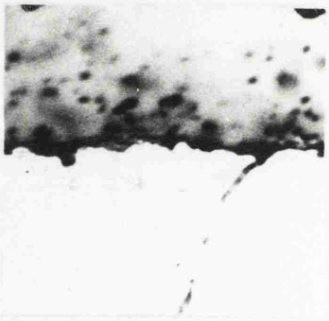

Fig. 3.22

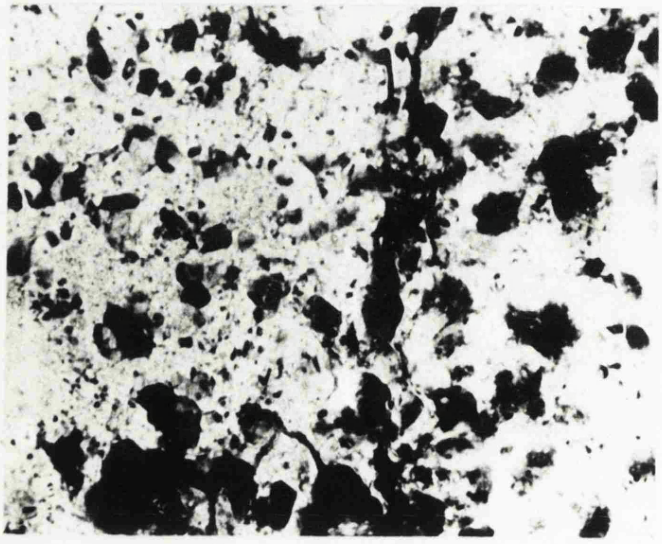

Fig. 3.23

(It should be noted however that small patches of duplex oxide formed during the transition stage never showed this effect.)

Specimens of Fe-9% Cr alloy of thickness 0.5mm, 1.0mm and 2.1mm were prepared simultaneously to ensure that the prepared surfaces were closely similar and oxidised together in the metallographic furnace at 600°C for 120 hours. The visual appearance of the oxidised specimens was generally similar to previously studied Fe-9% Cr specimens although the scale on the thinnest specimen, 0.5mm, was covered with a network of fine cracks. All the oxide scales were much more readily detached from samples oxidised in the metallographic furnace than from specimens oxidised on the microbalance. The fragility of oxide layers made the preparation of metallographic sections difficult. Oxidised specimens were mounted by vacuum impregnation with a low viscosity polyester resin and polished using successively finer grades of abrasive. Examination under the optical microscope showed that the fragile inner layer was severely damaged. In no case was mounting resin found within the pores. Oxidised specimens cooled slowly in the metallographic furnace always had a large lamella void at the oxide-metal interface filled with a very loose powdery oxide, whereas those oxidised in the microbalance rig (where specimens are cooled rapidly from the oxidation temperature) rarely showed this feature; this explains the very ready detachment of scales on the former group of specimens.

Measurements were made of the distance from the oxide-oxide interface to the first lamellar void and of the distance between successive lamellar voids on a number of areas of the specimens. These results, together with data obtained on other alloys are summarised in Table 3.2.

Although the number of lamellae was constant for any one specimen, the interlamellar spacing varied from point to point as indicated in Table 3.2. It should be noted that no lamellar voids were observed on the Fe-20% Cr alloy within the duration of the experiment. On the thinnest specimen (0.5mm) lamellar voids were very fine and the oxide so badly damaged by the specimen preparation procedure that only an upper limit to the interlamellar spacings could be specified. The distance between the first formed lamella and the oxide-oxide interface generally increased with increasing chromium content and the interlamellar spacings varied in an approximately linear manner with specimen thickness. Attempts to prepare fracture sections for examination in the SEM were unsuccessful since the fragile scales always detached from the metal on impact. Particles extracted from the surfaces exposed by cleaving the scale along a lamella void were similar to the rod-like particles discussed in Section 3.3.2 and they were analysed on an AE1 EMMA4 instrument and shown to have a composition similar to the mean composition of the inner oxide layer.

TABLE 3.2 - Effect of specimen thickness and chromium content on lamellar void spacings in the inner oxide

Cr in alloy (wt %)	Specimen thickness (mm)	A[1] (m)	B[2] (m)
5	1.0	3 (± 1)	3
9	1.0	6 (± 2)	3
9	2.1	12 (± 3)	6
9	0.5	6 (± 2)	2
12	1.0	10 (± 3)	3
15	1.0	13 (± 4)	3
20	1.0	20	-

[1] Distance from oxide-oxide interface to first visible lamellar void.

[2] Distance between successive lamellar voids.

3.7 The early growth of oxide films on Fe-Cr alloys including alloy single crystals

In the preceding sections the formation of thin rhombohedral oxide films on etched polycrystalline materials has been described. These films form during the primary oxidation stage and are gradually replaced during the transitional oxidation period by regions of thicker spinel oxide. The duration of the primary period is very irreproduceable, even for simultaneously prepared specimens oxidised concurrently, indicating that the formation of the initial film depends on factors which are not easily controlled. These factors may include the nature of the residual gas atmosphere in which the specimen is brought up to temperature, chemical and structural inhomogenities in the surface regions of the specimen and chemical and structural changes occurring at temperature. To provide more information on the initial oxide growth processes, experiments were carried out on electropolished alloy single crystals cut to expose (100), (110) and (111) surfaces, containing 15 wt % Cr and 70 wt % Cr, as well as on electropolished Fe-20% Cr polycrystalline alloys at 600°C. The morphology and texture of the oxide films is described together with the growth sequence of the different phases which can form.

3.7.1 Fe-15% Cr alloy single crystals

After 10 minutes oxidation at 600°C, the

bright electropolished surface had become dull, although still retaining some metallic lustre. The (100) face gave strongly arced reflection electron diffraction patterns, see Fig. 3.24a and 3.24b taken with the beam along [100] and [110] directions respectively in the substrate metal. These patterns show that a single-crystal layer of cubic oxide oriented with a cube face parallel to the metal surface has formed with the [110] direction in the oxide parallel to the [100] direction in the metal. It is difficult to distinguish between spinel oxide, M_3O_4, (cubic a = 8.396Å) and γ-M_2O_3 (tetragonal, a = 8.33Å, c/a = 3.0). However, the presence of a 200 diffraction in Fig. 3.24a, together with 510 and 710 diffractions seen in Fig. 3.24b, is firm evidence that the tetragonal phase is present, while the closely-spaced pairs of diffractions, such as 333 (M_3O_4) and 339 (γ-M_2O_3) circled in the pattern, show that spinel oxide has also formed. No evidence of rhombohedral oxide, α-M_2O_3, was found. These data were confirmed by transmission electron diffraction studies on oxide films removed from the metal. Electron probe microanalysis of the stripped layer showed that it contained chromium and iron, with a Cr:Fe ratio of 2.0 $\pm$ 0.5. The value was obtained using a beam voltage of 25kV and comparing K-spectra X-ray counts with those from pure metal standards; no corrections for absorption and fluorescence were made since it was assumed that such effects would be small in the standards and negligible in the thin film. It was noticeable that the film tended to curl convex to the metal substrate, due to

a stress gradient within the layer.

After 30 minutes oxidation, similar electron diffraction patterns of oriented γ-M_2O_3 and M_3O_4 were obtained from the (100) face of the metal. Oxide crystallites were now well developed, Fig. 3.25, appearing as truncated octahedra formed by (111) planes and the (100) plane parallel to the substrate. This layer when stripped was too thick for transmission studies in the 100kV electron microscope but some detail was observed at 50kV using the STEM facility of the JXA 50A electron probe microanalyser. Using a beam of 10keV electrons to excite K-radiation and pure metal standards, a Cr:Fe ratio of 1.2 $\pm$ 0.05 was measured from the side of the film originally adjacent to the metal and a ratio of 1.1 $\pm$ 0.05 from the gas-oxide interface. In order to improve the sensitivity of the technique to differences in surface composition, lower probe energies were then employed to reduce the electron penetration. Using 5keV electrons and recording Cr Lα and Fe Lα lines, Cr:Fe ratios of 1.5 $\pm$ 0.1 and 1.0 $\pm$ 0.1 were obtained from the respective sides of the oxide layer. These data demonstrate that the oxide adjacent to the metal was significantly richer in chromium than the gas-oxide interface.

Reflection electron diffraction of (110) and (111) faces oxidised for times up to 1 hour showed the presence of M_3O_4 with indications of γ-M_2O_3. The patterns were essentially one-degree-oriented with the (100) plane in

the oxide lying parallel to the substrate surface; regions of two-degree-oriented oxide, with [110] in the oxide parallel to [100] in the metal, were found on the (110) metal surface.

3.7.2 Fe-70% Cr alloy single crystals

A similar series of oxidation experiments carried out on this crystal showed, in all cases, the formation of a finely polycrystalline film of rhombohedral oxide, Fig. 3.26, irrespective of substrate orientation. The oxide layers were very much thinner than those produced on the Fe-15% chromium single crystals after comparable oxidation times. After 30 minutes oxidation only a pale straw-coloured oxide film was produced which was highly reflecting. The colour intensified somewhat with further oxidation but even after 2 hours the colour was only a pale green-straw. The thin films could not be removed from the substrate without severe fragmentation, even with the application of a thick carbon support layer and microanalysis was therefore carried out with the oxide attached to the metal. Three measured intensity ratios are plotted in Fig. 3.27 as a function of the incident electron energy. The first, curve A, shows the ratio of Fe Lα X-ray emission from oxidised and unoxidised alloy and it can be seen that, as the probe voltage is reduced, the ratio decreases to zero at 3.7keV. Curve B shows the ratio of Cr Lα X-ray emission from oxidised and unoxidised alloy. The complex shape of curve B may be related to X-ray peak

shape effects. Curve C shows the ratio of Cr Lα X-ray emission from a pure Cr_2O_3 sample and the unoxidised metal. The important feature of curves B and C is that at the electron energy where the Fe Lα emission ratio is zero, the Cr Lα ratios are the same within experimental scatter. The results indicate that the thin surface oxide is essentially Cr_2O_3.

3.7.3. Polycrystalline specimens

The surface of the electropolished iron-20% chromium alloy oxidised for 10 minutes exhibited marked differences in the rates of oxidation of different grains, as evidenced by the range of interference colours observed; preferential oxidation of grain boundaries was also noted, Fig. 3.28. Reflection electron diffraction patterns showed only spinel oxide, the sharpness of the diffractions indicating that the pattern was produced by grain-boundary oxide projecting into the path of the electron beam. Transmission studies on stripped films enabled three types of oxide growth to be distinguished. Some areas consisted of a thin film of finely polycrystalline ($<$100A) rhombohedral oxide; a number of larger crystals of α-M_2O_3 together with traces of γ-M_2O_3 were found, as well as regions of spinel oxide. Longer oxidation caused the oxide nucleated at grain boundaries to spread across the entire surface.

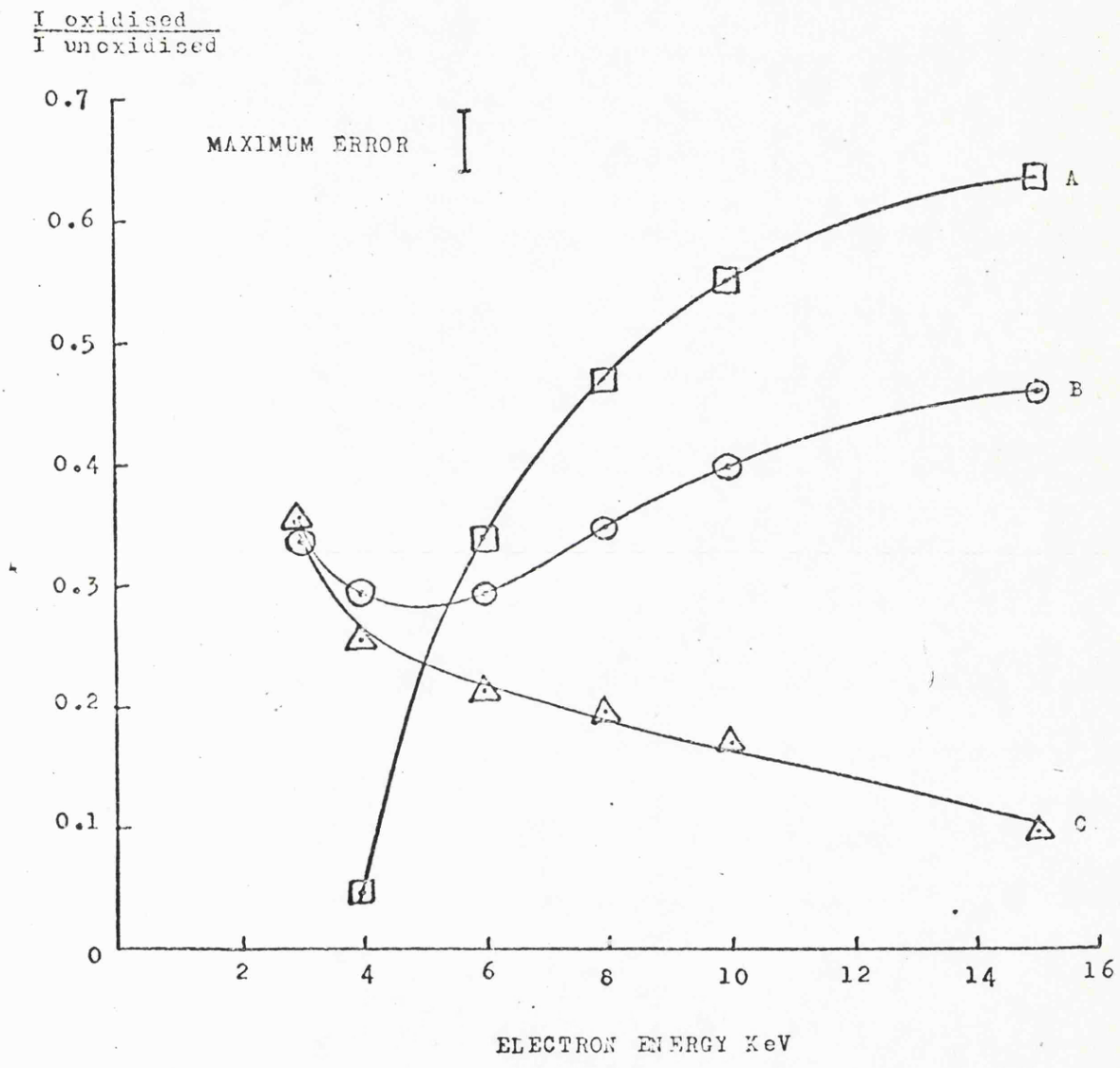

Fig.3.27 Oxidised alloy as Fig.3.26. Electron probe microanalysis measurements as a function of electron energy with beam normal to the surface. Curve A shows the ratio of Fe L and curve B the ratio of Cr L from oxidised and unoxidised alloys; the ratio of Cr L from pure Cr_2O_3 and unoxidised alloy is indicated by curve C. Note that at just below 4 keV the X-ray emission from the oxidised alloy is essentially the same as that from pure Cr_2O_3.

Fig.3.24 Fe-15% Cr alloy single crystal oxidised at 400°C. Reflection electron diffraction patterns of (100) face.
(a) Beam along $\langle 100 \rangle$ metal showing presence of single crystal cubic oxide. Note doubling of spots due to M_3O_4 and γ-M_2O_3 eg. 333 (M_3O_4) and 339 (γ-M_2O_3) circled.
(b) Beam along $\langle 110 \rangle$ metal. Note presence of diffractions of type h10 (h odd) eg. 510 (circled).

Fig.3.25 Oxidised alloy as Fig.3.24 showing growth habit of oxide crystallites; arrow denotes $\langle 100 \rangle$ in metal. Scanning electron micrograph X 50000.

Fig.3.26 Fe-70% Cr alloy single crystal oxidised at 600°C for 10 minutes. Reflection electron diffraction pattern showing presence of finely polycrystalline α-M_2O_3.

Fig.3.28 Electropolished polycrystalline Fe-20% Cr alloy oxidised at 600°C. Scanning electron micrograph showing preferential growth of spinel at grain boundaries.

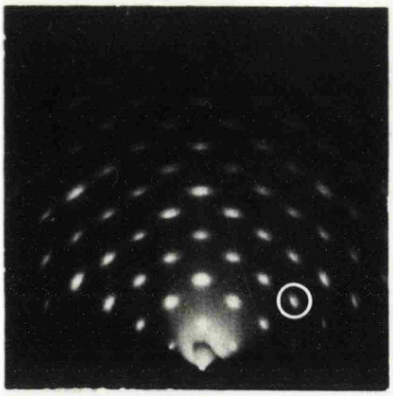

Fig. 3.24(a)

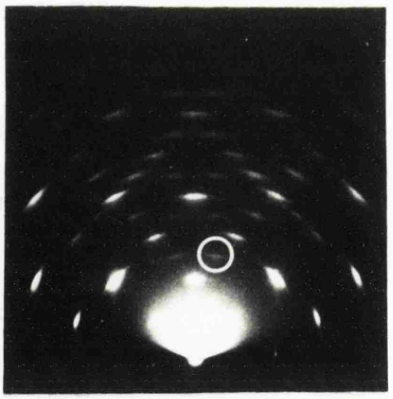

Fig. 3.24(b)

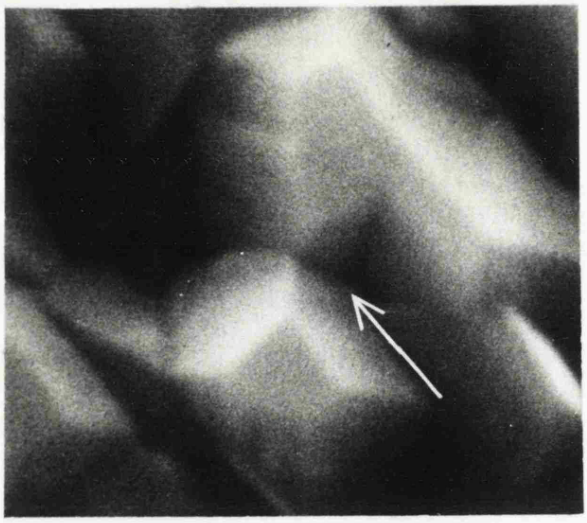

Fig. 3.25

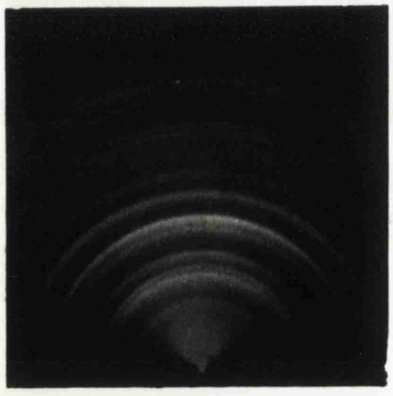

Fig. 3.26

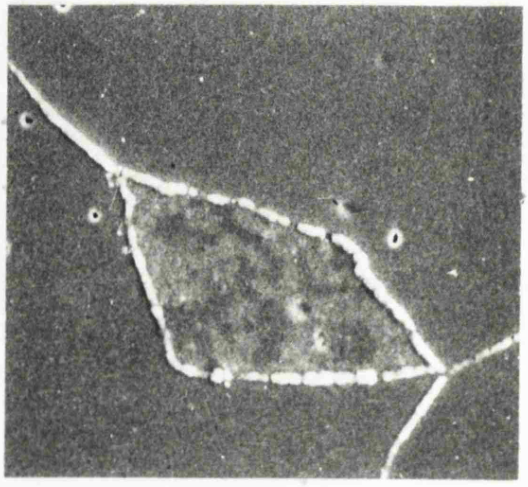

Fig. 3.28

The oxidation behaviour of the electropolished iron-15% chromium polycrystalline alloy was similar to electropolished iron-20% chromium alloy.

CHAPTER 4

DISCUSSION

4.1 General

In the previous section it was shown that analysis of the kinetic data from a range of polycrystalline alloys containing 5, 9, 12, 15 and 20% Cr oxidised at 400, 500 and 600°C in CO_2 - 1% CO based gas indicated that their oxidation behaviour could be separated into three stages; these have been termed the primary, transitional and secondary stages. The primary stage is associated with a relatively slow oxidation rate producing oxide films typically $\sim$1000 A thickness. During transitional oxidation the reaction rate increased at first and then decreased until eventually parabolic growth kinetics were observed. This parabolic or secondary stage was associated with the growth of thicker films ($> 1\mu m$) consisting of two layers. The duration of the primary stage was dependent markedly on the oxidation temperature and alloy composition. In the secondary stage of oxidation the parabolic rate constants were found to be dependent on temperature and substantially independent of alloy composition. It was apparent that some samples had not fully entered secondary oxidation within the duration of the experiments (up to 150 hours). Since all experiments showed essentially the three stages of oxidation it is convenient to present the discussion in terms of the fundamental processes involved in each stage as outlined below.

The following section of the discussion, § 4.2, is concerned with the mass transport processes occurring during the secondary stage. It is shown that the duplex nature of the oxide and the relative thicknesses of each of the layers may be accounted for by diffusion processes controlled by the outward migration of cations through the oxide scale. In Section 4.3 the element distributions in the duplex scale are discussed. A model is then proposed which explains these segregation effects by considering possible diffusion paths through the oxide lattice and relating the mobility of a cation to the difference in stabilisation energies for octahedral and tetrahedral sites as estimated from crystal field theory. The proposed model is extended to other related systems and is compared with observations of other workers. The outward movement of metal ions creates vacancies in the metal and in Section 4.4 the condensation of these vacancies to form voids is discussed. Based on the observation that voids form as lamellae parallel to the metal surface, it is proposed that vacancy condensation occurs at the metal-oxide interface by a cyclic process and that the interlamellar separation may be related to interfacial energy factors. Evidence is also presented which indicates that the inner oxide layer grows by gas-phase transport of oxidant (via pores in the oxide) to the metal surface.

The structure and growth characteristics of thin oxide films formed in the initial (primary) stage of oxidation are dealt with in Section 4.5. It is shown that this stage

is associated with the presence of a relatively protective oxide on the metal which is structurally different from the spinel produced in the faster parabolic oxidation stage and that its formation depends upon a number of factors which include alloy composition, metal orientation and surface treatment. Complementary results obtained from oxidised single crystals of iron-chromium alloy enable the crystal structures and orientation relationships of the thin oxide films to be characterised. The structure and growth sequences of thin oxide films found on both single crystals and polycrystalline materials is then explained using values of the chromium solubility of the various phases estimated using crystal field theory together with considerations of interfacial and strain energy factors.

The final section of the discussion (§ 4.6) is concerned with the region of transition from primary to secondary oxidation. It is shown that this may be related to the nucleation of spinel oxide at sites usually close to grain boundaries or at asperities on the surface and its growth laterally across the entire surface, from which point in time parabolic kinetics are observed. A model for the growth of spinel nuclei is developed and shown to account for the observed shape of the kinetic curve. In particular it is suggested that the small and systematic discontinuities detected in the kinetic curves are associated with localised breakdown of the initial protective oxide.

4.2 Mass Transport Processes Occurring During the Formation of Thick Oxide Scales

Experimental observations have shown (Fig. 3.7a) that the thick oxide scales formed on all alloys during the secondary oxidation stage are similar. In particular the ratio of the thicknesses of the inner and outer oxide layers tends to a value of $\simeq 1$ as the oxidation proceeds (Fig. 3.6). It is noteworthy that the interface between these two layers coincides with the original metal surface (Fig. 3.12). This structure suggests that the outer layer is formed by migration of metal atoms (or ions) outwards while the inner layer is produced by the inward diffusion of an oxygen containing species. The outward movement of cations through the oxide layer is consistent with the unconstrained growth morphology observed at the outer oxide surface, Fig. 3.5. Composition measurements indicate that chromium is concentrated in the inner scale layer (see § 4.3) while the outer layer is essentially pure Fe_3O_4. The oxidation rate is virtually independent of the chromium content of the material which implies that diffusion of cations through the outer layer is the rate determining process. As a consequence of this outward movement of cations, space is created below the original metal interface which is filled with inner oxide. This mechanism is in accord with the observed thickness ratio as the following analysis shows.

If the total weight of metal oxidised is W, then the volume of the vacated space below the original metal surface

due to the outward diffusion of metal may be written as W/ρ_m and the weight of inner oxide which fills that space as $W\rho_o/\rho_m$, where ρ_m and ρ_o are the densities of the metal and oxide respectively. Putting f equal to the weight fraction of metal in the oxide, the weight of metal in the inner oxide will be $W f \rho_o/\rho_m$ and in the outer oxide $W(1 - f \rho_o/\rho_m)$. Thus the volume of the outer oxide is $W (1 - f \rho_o/\rho_m) / \rho_o f$ and hence the ratio of the thicknesses of the inner to the outer oxides, R, may be written $R = f \rho_o/(\rho_m - f \rho_o)$. Taking $\rho_m = 7.8 \times 10^3$ kg m^{-3}, $\rho_o = 5.2 \times 10^3$ kg m^{-3} and f = 0.72 for spinels of general formular $Fe (Fe_{2-x}, Cr_x)O_4$ the thickness ratio R is 0.93. This is close to the experimentally determined value ($\sim$ 1) and thus lends some support to the transport mechanism proposed above.

From kinetic data the activation energy for the oxidation was found to be 130 kJ mol^{-1} (Fig. 3.4) (31 k cal mol^{-1}). Published data (Himmel, Mehl and Birchenall, 1953) for the activation energy of lattice self diffusion of cations in Fe_3O_4 $\sim$ 55 k cal mol^{-1} (230 kJ mol^{-1}) is somewhat higher than the 130 kJ mol^{-1} determined from the oxidation process. It may be deduced therefore that appreciable grain-boundary diffusion of cations occurs at these low oxidation temperatures (the activation energy for grain-boundary diffusion is approximately one half the lattice diffusion value, i.e. $\sim$ 120 kJ mol^{-1}).

The growth of the inner layer of oxide in the space

created by the outward moving cations requires transport of an oxygen-containing species across the outer layer. The possibility that oxygen anion diffusion is responsible is unlikely in view of published data (Castle and Surman, 1969) which shows that anion diffusion in Fe_3O_4 is too slow to account for the rapid build up of inner oxide. Evidence will be discussed later which supports a mechanism based on the diffusion of gaseous oxidant through the scale.

4.3 Segregation Effects in Oxide Scales

It was demonstrated in section 3.2, that when duplex scales were formed on iron-chromium alloys, chromium is essentially absent from the outer layer giving an outer oxide, Fe_3O_4, and an inner oxide consisting of an iron-chromium spinel (Fig. 3.17). The effect of alloy composition was to change the composition of the inner layer such that the ratio of the weight fraction of chromium in the inner scale to the weight fraction of chromium in the metal was always 1.5. Similar observations of element partitioning in oxide scales on alloys abound in the literature. Pfeil (1929) showed that most of the transition elements with the exception of manganese, were concentrated within the inner layer of oxide formed on alloy steels in air at 1000°C. The findings have since been substantiated and extended by a large number of workers. For example, Brenner (1955) found molybdenum concentrated in the inner scale on iron-molybdenum alloys oxidised at 1000°C. Moreau (1953) reported a similar effect on iron-chromium

alloys and Rahmel (1962) found that vanadium, chromium, silicon and molybdenum were confined to the inner oxide scale of the respective binary iron alloys oxidised at 1000°C in oxygen. Similar partitioning behaviour has been observed on more complex iron alloys, both ferritic and austenitic, and also in a variety of oxidising environments. In work comparable with the present study, Antill, Peakall and Warburton (1968) noted duplex scales on steels oxidised in CO_2 gas in which the inner oxide contained chromium ard molybdenum while iron and manganese were distributed throughout the double layer.

However, despite the large accumulation of data on segregation effects in oxide layers there appears to have been little attempt to explain this behaviour apart from Surman and Castle (1969) who invoked a vapour phase transport mechanism to account for segregation of chromium in the inner layer of oxide.

4.3.1 The Diffusion of Cations in Close Packed Oxides

Most oxide lattices may be regarded as close-packed arrangements of oxide ions containing cations in the octahedral and tetrahedral interstices. Only a fraction of these interstices are normally occupied, for example, only one quarter of the sites are occupied in an AB_2O_4 spinel, and cation diffusion through the lattice may occur via unoccupied interstices.

Azaroff (1961) and Tilley and Stone (1972) have considered

possible diffusion paths for cations in close-packed anion lattices such as M_3O_4 and the preferred route in cubic structures was shown to be via alternate, adjacent octahedral and tetrahedral positions; diffusion via similar interstices, e.g. tetrahedral-tetrahedral or octahedral to octahedral, was considered less likely due to the severe lattice distortion involved in these modes of cation transfer.

The diffusion coefficient D, of a cation in a close packed oxide may be expressed as an Arrhenius equation of the form

$$D = D_o \exp - (E_a)/RT$$

where D_o is a constant, E_a is the activation energy, R the gas constant and T the temperature. Fig. 4.1 shows a plot of the potential energy of the system during transfer from an octahedral to a tetrahedral site. It can be seen that the activation energy E_a is composed of two components E_s and E_p. E_s may be regarded as the strain energy of the system associated with the passage of the cation between the trigonal arrangement of anions separating the two types of interstice, while E_p is the energy difference between a cation placed in a tetrahedral field and in an octahedral field. E_p is shown in Fig. 4.1 as an octahedral site preference. The strain energy E_s is primarily a function of the repulsive interaction between ions as their electron orbitals interpenetrate and thus depends on the classical ionic radius. However, for the first-row transition metals

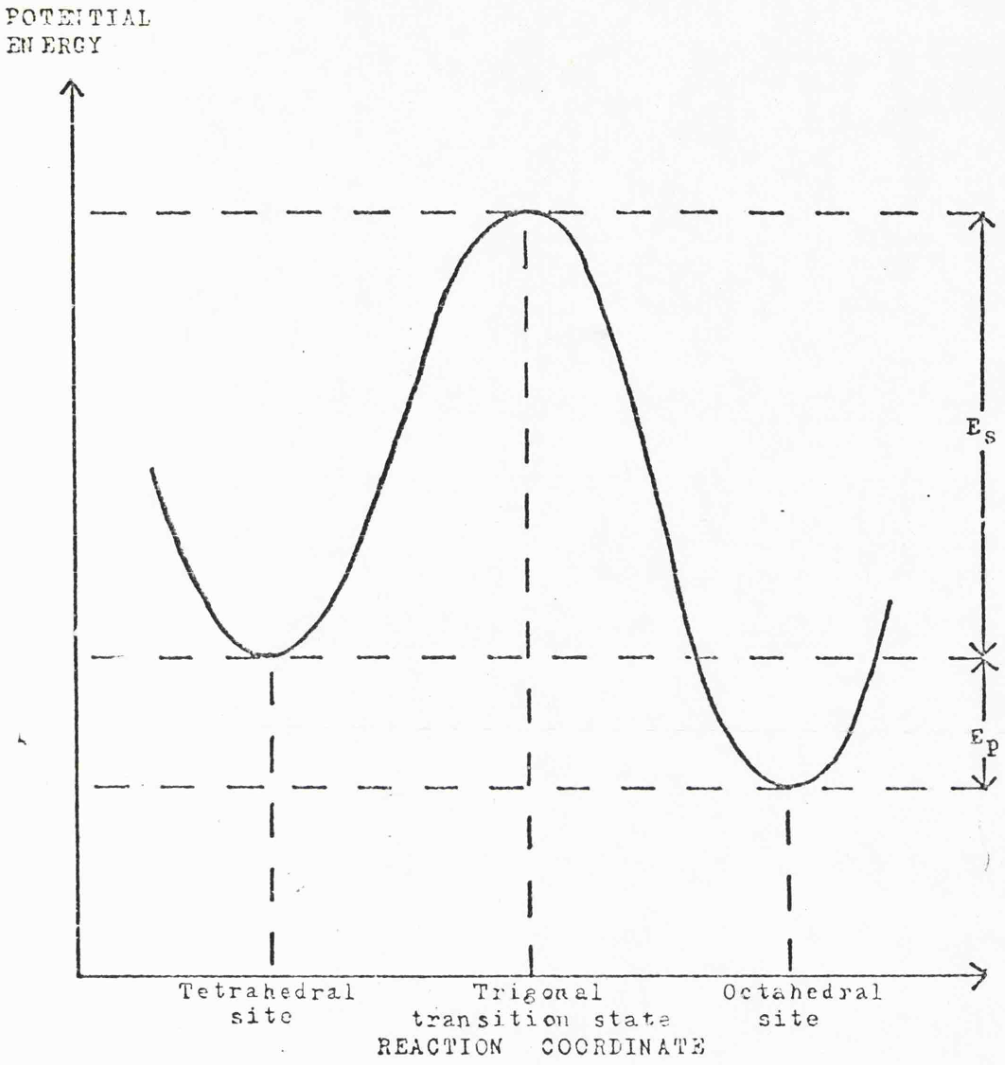

Fig.4.1 Diagram showing energy change during cation transfer from a tetrahedral site to an octahedral site in a close packed oxide.

ions of similar charge have very similar sizes, see Table 4.1. Thus the value of E_s would be expected to be approximately constant for ions of a given charge. The value of E_p for the transition metal ions is the difference in the energy of a cation in sites of four and sixfold coordination. This difference may be related to the difference in the crystal field stabilisation energy for a cation in each site respectively and is termed the crystal field preference energy (CFPE). Values, calculated from spectroscopic data by Dunitz and Orgel (1957), are given in Table 4.1.

In order of increasing crystal field preference energy, the series may thus be written:

for trivalent ions Fe^{3+}, Ti^{3+}, V^{3+}, Mn^{3+}, Cr^{3+}

for divalent ions Mn^{2+}, Fe^{2+}, Co^{2+}, Cu^{2+}, Ni^{2+}.

This order of increasing crystal field preference energies should correspond to the order of decreasing cation mobility through close-packed oxide lattices.

4.3.2 Evaluation of the Proposed Model

Since lattice diffusion controls the rate of oxidation of many pure metals (Kubaschewski and Hopkins, 1967) the parabolic rate constant may be written

$$\log k = \log k_o - E_s/2303\ RT \quad -E_p/2303\ RT$$

where k is the parabolic rate constant. In Fig. 4.2 log k is plotted against E_p for the first row transition metals. The oxides of the metals used here have close-packed cubic

TABLE 4.1 - Crystal field preference energies (CFPE) and ionic radii for transition metal ions

Ion	Number of d electrons	CFPE[1] kJ mol^{-1}	Ionic[2] radius Å
Ti^{3+}	1	29	0.76
V^{3+}	2	54	0.74
Cr^{3+}	3	158	0.69
Mn^{3+}	4	96	0.66
Mn^{2+}	5	0	0.80
Fe^{3+}	5	0	0.64
Fe^{2+}	6	17	0.76
Co^{2+}	7	31	0.74
Ni^{2+}	8	86	0.72
Cn^{2+}	9	64	-

[1] Values from Dunitz and Orgel (1957).

[2] Values from Wells (1962).

anion lattices except Cr_2O_3 where the anions are situated on a hexagonal sublattice. Azaroff (1961) has shown that in the hexagonal structure adjacent octahedral interstices parallel to the c-axis form possible diffusion paths. However, two thirds of these positions in Cr_2O_3 will be already occupied by cations and either the diffusing cation will have to by-pass the occupied site by way of a tetrahedral interstice or the occupying cation must be displaced to a tetrahedral position to create an octahedral vacancy. These two processes are energetically equivalent and in both cases the rate of transfer of the cation is determined by the difference in energy when placed in an octahedral or tetrahedral position as in cubic close-packed structures. High temperature oxidation data ($T > 1000K$) have been used in Fig. 4.2 wherever possible since at lower temperatures ($T < 800°K$) grain-boundary diffusion may be important. Titanium and copper are omitted from Fig. 4.2 since the former oxidises by inward diffusion of oxygen via anion defects (Kubaschewski and Hopkins, 1967) and neither titanium nor copper form oxides with close-packed anion lattices.

In the case of vanadium, volatility of the pentoxide precludes quantitative measurements of oxidation rates at high temperatures and, consequently, low temperature results were used. The points in Fig. 4.2 lie close to straight lines of slope $^1/_{2.303}$ RT which indicates, to a first approximation, that the variation of E_s through the series is small compared with variations in E_p. It should also be noted that the magnitude of the strain energy term E_s,

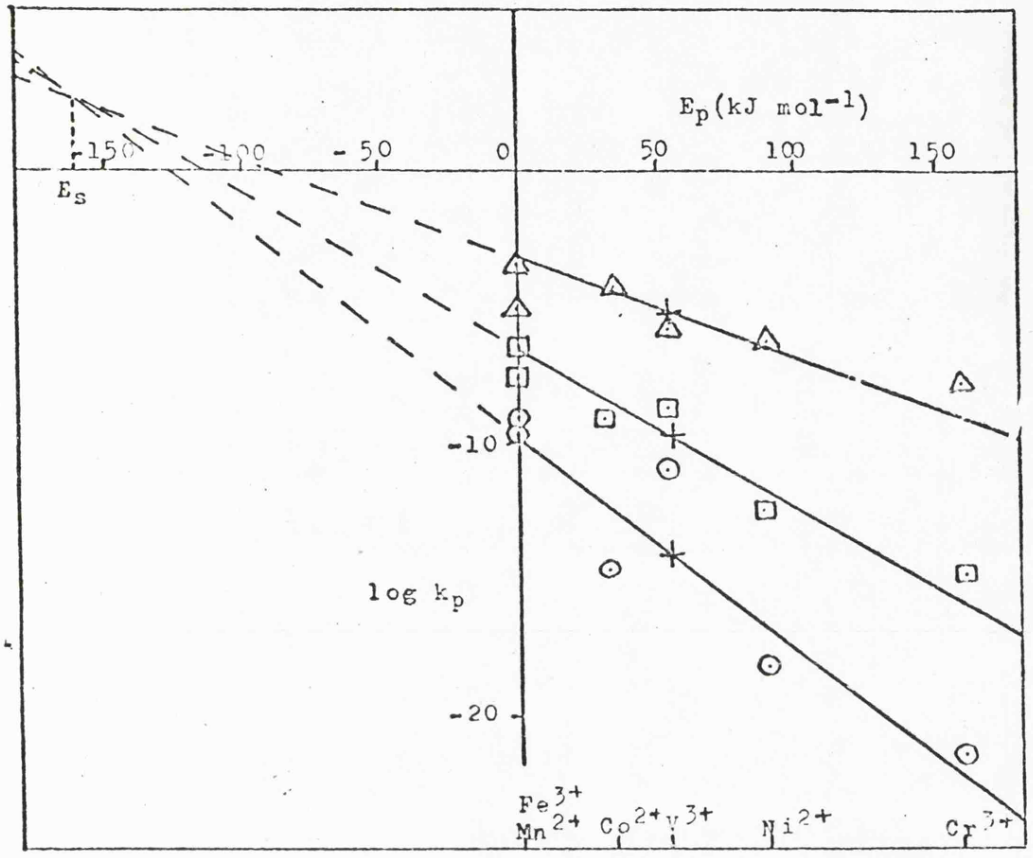

Fig.4.2 Plot of log k vs Ep for Fe, Mn, Co, Ni, Cr at 668 K, ⊙, 910 K, ⊡ , and 1429 K, △ . The lines are of slope 1/2.303 RT passing through the centroid, +.

estimated from the intersection of the three lines as 159 kJ mol^{-1}, is of the same order of magnitude as some of the octahedral site preference energies, E_p, given in Table 4.1.

The observed scatter of points about the straight line may be attributed to a number of factors. For example, since trivalent ions are smaller than divalent ions, they may pass more easily between the trigonal arrangement of anions which separate one type of interstice from the other and result in a smaller value of E_s. Trivalent cations will be more stable in the transition state than divalent ions of the same ionic radius since attractive coulombic interactions between the trivalent cation and the trigonally disposed anions are greater than for a divalent ion. These effects are most clearly seen from the positions of Fe^{3+} and Mn^{2+} in Fig. 4.2 where for $E_p = 0$, E_s is smaller for the trivalent ion. In the case of rocksalt structures e.g. FeO, CoO and NiO, all the available octahedral sites are filled and vacancies may have to be present for appreciable diffusion to occur, adding an extra term to the activation energy, E_A, for these elements. For vanadium the activation energy may well be lower than that predicted due to a significant contribution from grain-boundary diffusion to the low-temperature oxidation rate in this case.

The correlation thus established between parabolic oxidation rate and crystal field preference energy for a

number of first row transition elements leads to the following conclusions: (i) oxidation of these elements is controlled by lattice diffusion of cations through the oxide via octahedral and tetrahedral sites and (ii) rate of diffusion of cations is determined principally by the crystal field preference energy which may be similar in magnitude to the strain energy term arising from ion-ion interactions in the transition stage.

4.3.3 Application of the Model to Segregation of Elements in Oxide Scales on Alloys

The virtual absence of chromium from the outer oxide on ion-chromium alloys oxidised at 600°C is in accord with the above hypothesis that the Cr^{3+} ion will diffuse with difficulty through spinel oxides. Since all the chromium was retained by the inner oxide the concentration of chromium in this layer may be calculated as follows. It was shown in Section 4.2 that the weight of inner oxide produced by oxidation of a weight W of metal was $W \rho_o/\rho_m$. If the weight fraction of chromium in the metal is f_1 then the weight of chromium in the inner layer (assuming none diffuses into the outer layer) will be Wf_1. Thus the weight fraction of chromium f_2 in this layer is given by

$$f_2 = \frac{W f_1}{W \rho_o/\rho_m} = f_1 \frac{\rho_m}{\rho_o}$$

substituting values for p_m and p_o (see § 4.2) gives $f_2 = 1.5 f_1$ in close agreement with the experimentally determined

values for all the alloys when parabolic kinetics are followed.

This treatment of partitioning of transition metal alloyants in oxide scales is very general and can account for many of the observations in the literature. Various workers e.g. Antill et al (1968) and Pfeil (1929), have shown that manganese (the only other common element forming a stable d^5 wn, Mn^{2+}, with $E_p = 0$) is present in both layers. Analysis of Pfeil's results indicate that the mobility of the common transition elements in iron oxide decreases in the order Fe : Mn : V : Ni : Cr, which corresponds closely with the predictions of the above model. The partitioning reported by Pfeil was less marked than in the present study, i.e. the concentration gradient at the interface was less steep, but the much higher temperatures employed in Pfeil's work ($>$ 1000°C) would result in more interdiffusion of the cations. Indeed the element distribution in these high temperature scales may be treated simply as diffusion into a semi-infinite medium (the outer oxide scale) and the concentration profile would be given by an equation of the form:

$$C(x, t) = \frac{C}{2}\left(1 + \operatorname{erf} \frac{x}{2\sqrt{Dt}}\right)$$

where x is the distance measured relative to the original metal surface and C is the inner scale composition remote from the boundary (= 1.5 f_1; see above).

Surman and Castle (1969) have considered segregation

using an alternative approach. They suggest that in steam and possibly carbon dioxide, the formation of volatile compounds is responsible for the growth of the outer layer. For example iron is known to form a volatile hydroxide while no such compound has yet been characterised for chromium and thus segregation of chromium in the inner oxide formed on iron-chromium alloys may be explained. However, such considerations are unlikely to account for the segregation effects observed on the wide variety of transition metal systems for which published data are available.

Although the cation diffusion model was developed primarily to account for partitioning in oxides formed on ferrous alloys it can be seen to be generally applicable to transition metal alloy systems. For example the higher concentration of nickel in the inner layer of a duplex oxide scale on cobalt-nickel and manganese-nickel alloys (Kubaschewski and Hopkins, 1967) is clearly in accord with the proposed model.

4.4 Vacancy Condensation and Void Formation in Duplex Oxide Scales

It has been shown, § 4.3, that the duplex nature of the oxide and the relative thicknesses of each of the layers may be accounted for by diffusion processes which are controlled by the outward migration of cations through the scale. Evidence is presented showing that the outer

layer, Fe_3O_4, consists of columnar crystals which contain voids, the void fraction decreasing with distance from the oxide-oxide interface. Voids were also found in the inner layer and were usually arranged in lamellar distributions parallel to the oxide-metal interface. Prolonged oxidation caused a succession of lamellar voids to develop at regular spacings. It was also found that distances between successive lamellar voids were independent of alloy composition, although the distance from the oxide-oxide interface to the first visible lamellar void increased with chromium content. It is proposed that these void structures may be explained using a model which considers the generation of vacancies during the oxidation process and their subsequent condensation to form the aforesaid voids.

It is worth noting that, although considerable information is now available on the formation and behaviour of vacancies in materials subjected to irradiation, quenching or mechanical treatment, the part played by vacancies in oxidation reactions has received relatively little attention. The frequent occurrence of void dispersions in oxide scales have been attributed, as long ago as 1952 (Dunnington, Beck and Fontana, 1952), to the precipitation of vacancies formed during the oxidation process. However direct experimental verification of the hypothesis was not provided until much more recently when studies on the growth of dislocation loops in metal foils oxidised in the electron microscope were reported (Hales, Dobson and

Smallman, 1968). No quantitative description of the vacancy concentrations produced by the oxidation reaction was, however, forthcoming from this work. In the present work a value for the vacancy fraction is estimated from the lamellar void spacings. A value for the energy to precipitate the first vacancy is also calculated and compared with the value deduced from surface energy changes accompanying lamellar void formation.

It may be shown that the vacancies injected into the metal as the outer oxide is formed will be fairly mobile. Direct information on the diffusion rates for vacancies in iron-chromium alloys at 600°C is not available but a high mobility may be inferred using comparative data on vacancy migration energies, E_m. Using values given by Smallman (1970), E_m for iron, copper and nickel are 0.76 eV, 1.1 eV and 1.5 eV respectively. The vacancy jump frequency, ω, may be written $\omega = Z\nu \exp^{-E_m/kT}$, where Z is the co-ordination number and ν is the atomic vibration frequency. Hence for iron at 600°C, $\omega = 3.2 \times 10^9$ sec^{-1}. This value is of the same magnitude as jump frequencies for copper at 1000°C (4.1×10^9 sec^{-1}) and nickel at 1100°C (3.4×10^8 sec^{-1}), at which temperatures vacancies are known to be mobile in these metals (Appleby and Tylecote, 1970, Hales and Hill, 1972). Thus it would be expected that diffusion of vacancies would readily occur in the lattice of the iron-chromium alloy at the oxidation temperature and that the diffusion rate would be further enhanced by a grain-boundary contribution at this temperature.

Initially these vacancies will be retained in solution until their concentration exceeds a critical level when they condense into voids at suitable precipitation sites. The appearance of voids aligned parallel to the metal-oxide interface indicates that this is the preferred site for oxidised iron-chromium alloys. In other metal-oxide systems voids are sometimes found at grain boundaries, e.g. copper (Appleby and Tylecote, 1970) and nickel (Hales and Hill, 1972). There is evidence that the metal can retain a high concentration of vacancies, since samples slowly cooled in the oxidation furnace were usually found to contain a void at the metal oxide interface whereas rapidly cooled specimens did not. The likelihood of stress contributing to void formation may be discounted because rapid cooling would favour the formation of an interfacial void as the mode of stress relief.

It follows that, after vacancy condensation has occurred, the vacancy excess in the metal would have to increase to the critical fraction before further vacancy rejection can take place. This would necessitate further oxide formation, by which time the metal-oxide interface would have advanced a discrete distance into the metal. Thus the periodic character of lamellar voids may be explained.

4.4.1 Growth of Inner Layer of Duplex Scale

The presence of voids in the inner layer indicates that growth of inner oxide may not take up completely

the space created by vacancy condensation. Such a situation can arise when the rate of growth of the inner layer becomes less than the rate of vacancy injection into the metal. As the oxide scale thickens the rate of growth of the inner layer becomes dependent upon the rate of supply of gaseous oxidant through pores and channels in the oxide scale. It is apparent that penetration of gaseous oxidant occurs readily in the early stages of oxidation, since the distance between the oxide-oxide interface (the original metal surface) and the first-formed lamellar void is usually greater than interlamellar void spacings, Table 3.2. In the later stages of oxidation, pores and channels in the outer layer become blocked by growth of oxide within them, as evidenced by the location and shape of voids close to the oxide-oxide interface in that layer, Fig. 3.18. In accord with this view, the occurrence of oxide crystals of filamentary habit in lamellar voids within the inner oxide is indicative of a growth process limited by gas-phase diffusion. Lamellar voids are not observed in the 20% chromium alloy, which suggests that the growth rate of the inner oxide is not significantly reduced in this case. The effect may be attributed to the high affinity of chromium for oxygen, which enables the 20% chromium alloy to oxidise more readily than lower-chromium alloys in low partial pressures of oxidant. This explanation would also account for the effect of chromium content of the metal on the location of the first-formed lamellar voids, Table 3.2.

The presence of voids in the inner oxide scale does

not significantly interfere with the rate of outward movement of cations since the parabolic rate constant is independent of the void structure in scales, Table 3.1. This may be attributed to the presence of the filamentary crystals which bridge voids and provide a diffusion path for cations. The high surface to volume ratio ($> 4 \times 10^5$) of the filamentary crystals suggests that surface diffusion may be the mode of transport of cations (Tagati, 1957). This view is supported by the high level of chromium found in these crystals, i.e. lattice diffusion of chromium is difficult in spinel oxides (§ 4.3) implying that an alternative mode of transport is involved.

4.4.2 Vacancy Condensation Model

The critical fraction of vacancies in the metal required for condensation to take place at the metal-oxide interface may be estimated from the interlamellar void spacing. Consider a piece of metal sheet, thickness t_1 and area A, covered with a layer of oxide containing lamellar voids of spacing t_2. Since oxidation occurs on both surfaces, the vacancy fraction injected into the metal is given by $2t_2A/t_1A = 2t_2/t_1$, ($t_2 \ll t_1$), assuming no plastic deformation occurs at the oxidation temperature.

The use of typical experimental values from the present study of $t_1 = 10^{-3}$ m and $t_2 = 3 \times 10^{-6}$ m, Table 2, gives a vacancy fraction of 6×10^{-3}. This value is much greater than the equilibrium vacancy fraction of $\sim 10^{-12}$ calculated using the quoted value for energy of vacancy

formation of 2.13 eV for iron (Smallman, 1970). The excess vacancy fraction is higher than values reported on materials quenched from temperatures close to the melting point ($\sim 10^{-4}$), but is of the same order of magnitude as excess vacancy concentrations produced by irradiation ($\sim 10^{-3}$; Cooper, Koehler and Marx, 1955). Quantitative data on vacancy concentrations caused by oxidation treatment are not readily available, although a value $\sim 10^{-2}$ can be inferred from a study on Fe-Cr-Al-Y alloys. (Tien and Rand, 1972).

The minimum vacancy concentration, C, for vacancy precipitation to occur in the manner proposed can be expressed as $C = C_E . \exp E_v/kT$, where C_E is the equilibrium vacancy concentration and E_v is the maximum energy required to induce a vacancy to condense at the interface. Using the above values for C and C_E and taking T = 873 K and k = 1.38 x 10^{-23} JK^{-1} gives E_v = 2.7 x 10^{-19} J.

An alternative approach to this problem is to consider the creation of a new internal surface by separation of the oxide-metal interface. The surface free energy change per unit area, ΔF_s, may then be written $\Delta F_s = (\gamma_m + \gamma_o - \gamma_{mo})$, where γ_m, γ_o, γ_{mo} are the specific surface free energies for metal-vapour, oxide-vapour and metal-oxide interfaces respectively. The cross-sectional area of a vacancy is given approximately by d^2, where d is the atomic spacing (= 2.5 x 10^{-10} m), and hence the average energy to induce each vacancy to condense at the interface is $E_v \sim (\gamma_m + \gamma_o - \gamma_{mo})d^2$

Taking $\gamma_m = 1.4\ Jm^{-2}$ (Jones, 1971), and reasonable estimates for $\gamma_{mo} \approx 0.4\ Jm^{-2}$ (Turpin and Elliot, 1966) and $\gamma_o \approx 1.0\ Jm^{-2}$ (Kelly, 1966) gives $(\gamma_m + \gamma_o - \gamma_{mo}) \approx 2\ Jm^{-2}$, and $E_v \approx 1.3 \times 10^{-19}$ J. This is the average energy per vacancy to form an extended two-dimensional void. Despite the approximations involved in both calculations, the values of E_v estimated by the two methods are in satisfactory agreement. In principle E_v calculated from the vacancy condensation model is expected to be higher, since more energy would be required to precipitate the first vacancy than to enlarge the cluster by subsequent vacancy absorption.

According to the model, with thicker specimens more vacancies would have to be produced to reach the critical level, and therefore a correspondingly thicker oxide film would have to be formed on the metal surface. Indeed if the above assumptions remain valid, a direct relationship between specimen thickness and interlamellar spacing would be expected. This conclusion is qualitatively supported by the changes in interlamellar spacings observed in the three specimens of iron-9% chromium alloy of different thicknesses, Table 3.2. It also follows that at intersecting surfaces a higher local vacancy flux would be injected into the metal than at a planar surface, leading to a greater incidence of voids at specimen corners as observed by other workers (Mrowec,1967).

4.4.3 The Role of Voids in Determining the Course of the Oxidation Reaction

From the information accumulated on the structure and properties of oxide scales it would be expected that the presence of voids in the layer may affect the oxidation reaction in one or more of the following ways.

(I) The ready detachment of some oxide layers is frequently reported in the literature and it is clear from the present work that when voids are present within the scale they may act as regions of mechanical weakness. Hence in practical applications of such alloys where detachment of oxide from metal may occur as a result of stresses imposed, for example by thermal cycling or impact, a consequent reduction of the protective character of the scales would occur.

(II) Evidence has also been presented showing that voids enable gaseous oxidant to reach the metal and react to form the inner layer. Thus voids have an important role in determining the microscopic transport properties of the scales. In particular, restricted rate of permeation of gas through the finely porous scale would result in the gas adjacent to the metal surface becoming increasingly richer in CO as a consequence of the reaction

$$xM + CO_2 \rightleftharpoons M_xO + CO.$$

It should be noted that this oxidation reaction proceeds with no volume change. The gas adjacent to the metal thus becomes increasingly carburising and as a result carbon

from the gas would be deposited either as free carbon or as carbide. This reaction may be represented

$$2\,CO \rightleftharpoons (C) + CO_2$$

where (C) represents free or combined carbon. In this reaction there is a net consumption of the gaseous phase and the resultant pressure gradient developed across the scale would increase the flux of gas reaching the metal and would correspondingly increase the rate of growth of the inner oxide.

(III) It is also envisaged that the presence of voids in an oxide may impede the lattice diffusion of cations and reduce the rate of growth of the outer oxide layer. The importance of this will, of course, depend on the nature of the void distribution, and the possible contribution of surface diffusion to cation migration cannot always be ignored. Indeed experimental data presented in this work suggests that surface diffusion may be important where the surface to volume ratio is high as in the development of filamentary microcrystals of oxide across voids (§ 4.4.1).

It is evident from the above considerations that, in general, porosity in scales is undesirable and that prevention of void formation is of importance in the design of high temperature alloys. Since vacancy condensation is believed to be intimately associated with void formation the addition of elements to the alloy which stabilise vacancies in solution as vacancy-solute complexes may be beneficial, a view shared by other workers (Tien and Pettit, 1972).

Alternative approaches to controlling porosity could involve the incorporation of a fine dispension of second phase particles, with a low energy of adhesion to the alloy, to act as vacancy sinks. The addition of solutes which increase the grain-boundary energy (and thus reduce the interfacial adhesion) may also be effective by inducing vacancy condensation at these sites rather than at the metal-oxide interface where it is shown to cause scale detachment.

In other studies on commercial iron-chromium alloys the formation of extensive lamellar void structures similar to those observed in the present study, is rare. It is conceivable that commercial alloys contain traces of elements which act to suppress vacancy condensation in one of the ways suggested above while the much "purer" alloys used in the present study do not. The metallurgical condition of the alloys would also, undoubtedly, have an influence and dislocations may provide sinks for the vacancies.

It would be of great interest to study a series of alloys with controlled additions of selected elements and to observe any subsequent changes in void structure. In this connection it is relevant to note the work carried out on void production during irradiation damage. Smidt and Sprague (1973) in particular have shown that the addition of solute atoms of appreciably larger diameter than the solvent atoms suppresses the formation of radiation-induced

voids in metals by acting as vacancy traps.

4.5 The Early Growth of Oxide on Fe-Cr Alloys

It has been shown that the oxidation of alloys containing greater than 12% chromium often starts slowly. This stage is associated with the growth of a thin rhombohedral oxide. The stability of this initial oxide film varies considerably depending on the alloy composition, orientation and surface treatment. This initial highly protective stage has been observed by a number of workers on iron-chromium alloys. (E.g. Yearian, Randell and Longo, 1956; Wood and Whittle, 1967).

Three oxides may form on iron-chromium alloys in the initial stages of oxidation by CO_2 at 600°C, α-M_2O_3, γ-M_2O_3 and M_3O_4, each phase containing varying amounts of iron and chromium.

In this section, the crystal structures and orientation relationships of thin oxide films formed on iron-chromium alloys are first discussed. This is followed by an explanation for the different oxide phases found in the present study. In the treatment initial oxide growth is first discussed followed by consideration of subsequent oxide growth; crystal field theory, interfacial and strain energy effects are invoked to account for observed oxide growth sequences.

4.5.1 Oxide Structures and Orientation Relationships

Studies on single crystals of iron-15% chromium alloy have shown that cubic oxides (γ -M_2O_3 and M_3O_4) grow such that cube faces of oxide and metal are parallel. The epitaxial cubic oxide formed on the (100) metal face has [110] in the oxide parallel to [100] in the metal, Fig. 3.24. The separation of cations along these directions is 2.96Å and 2.87Å for oxide and metal respectively, corresponding to a mismatch of 3%; the spacing between the close-packed rows in the oxide (5.92Å) is twice (within 3%) that in the metal. Such close correspondence between cation arrangements in the two lattices favours the high degree of epitaxy observed. The same orientation relationship was found by Howes (1967) on iron-28% chromium alloy. The manner in which these oxide films curled upon removal from the metal indicated they were subject to a compressive stress at the metal-oxide interface, which would be expected from the difference in cation spacings in oxide (2.96Å) and metal (2.87Å).

The observed orientation relationships between the spinel (S) and rhombohedral (R) lattices may be written: $(0001)_R // (111)_S$; $[10\bar{1}0]_R // [110]_S$. Thus the close-packed planes of anions are parallel, as was also deduced by Howes (1967). The present work, however, indicates that close-packed rows of anions are parallel in these oxides. The closest separation of anions in the (0001) plane is 2.86Å and in the (111) plane is 2.96Å, giving a mismatch of 4%,

considerably less than the 18% mismatch which follows from the alternative interpretation by Howes.

When the rhombohedral and spinel oxides were thin, the metastable phase, γ-M_2O_3 may be observed. In thicker layers little γ-M_2O_3 was found, either because it was too thin to be detected or because it transformed to α-M_2O_3 or M_3O_4 during the oxide thickening process. γ-M_2O_3 is structurally very similar to spinel, M_3O_4, and therefore these oxides were difficult to distinguish by diffraction methods. When γ-M_2O_3 was unambiguously identified, it was always found oriented with cube edges of the subcell parallel to the cube edge of the spinel unit cell.

4.5.2 Factors affecting Initial Metal Oxidation

The nature of the initial oxide film formed on an alloy will depend largely upon the activity of the elements in alloy and in oxide and upon the oxygen potential of the gas phase. While quantitative estimates may, in principle, be made using a thermodynamic approach, the lack of relevant data together with the non-equilibrium situation which exists during oxidation precludes rigorous calculation. However, for iron-chromium alloys oxidised at 600°C in CO_2-1% CO gas, the high affinity of chromium for oxygen suggests the formation of an initial oxide film richer in chromium than the metal. This is in accord with present observations where, for example, an almost pure chromium oxide was found on the iron-70% chromium single crystal.

The maximum amount of chromium which can be dissolved in the oxide film will be related to crystal structure and may be estimated using crystal field theory as follows. The phases α-M_2O_3, γ-M_2O_3 and M_3O_4 may be regarded as close-packed arrangements of anions containing cations in octahedral and tetrahedral interstices. A unit cell of spinel has 16 of the 32 octahedral sites and 8 of the 64 tetrahedral sites occupied by cations. Now Dunitz and Orgel (1957) have shown that Cr^{3+} has a strong preference, Fe^{2+} a weak preference and Fe^{3+} no preference for octahedral sites and hence a maximum of 16 Cr^{3+} ions may be accommodated in the spinel lattice, giving $(Fe_3^{2+})_t$ $(Cr_6^{3+})_o$ O_{12} with a chromium-iron (wt) ratio of 1.87. γ-Fe_2O_3 may be regarded as a defective spinel with one ninth of the cations removed from octahedral sites, i.e. $(Fe_3^{3+})_t$ $(Fe^{3+}_5, \square)_o$ O_{12}, where $\square$ represents a cation vacancy. Information concerning the solubility of Cr^{3+} in γ-M_2O_3 is not available but it may be deduced that a maximum of 16 Cr^{3+} ions can be accommodated in octahedral sites by replacement of Fe^{3+} and transfer of the cation vacancies to tetrahedral sites, giving $(Fe_2^{3+}, \square)_t$ $(Cr_6^{3+})_o$ O_{12} with a chromium-iron ratio of 2.79. In the α-M_2O_3 structure the cations occupy only octahedral sites and hence a complete range of mixed iron-chromium oxides from α-Fe_2O_3 to α-Cr_2O_3 is possible. It should be noted, however, that in CO_2-1% CO gas at 600°C progressive substitution of chromium by iron will eventually render α-M_2O_3 unstable with respect to spinel.

Thus solubility limits are predicted for chromium in γ-M_2O_3 and M_3O_4 from crystal field considerations, and chromium-rich α-M_2O_3 (Cr:Fe $>$ 2.79) is expected to form on high chromium alloys. Oxides on lower chromium alloys would be expected to contain more iron and formation of γ-M_2O_3 or M_3O_4 phases is possible. γ-M_2O_3 is not usually a stable phase but it may be stabilised in the presence of an interface. This is seen to occur in oxidation of the iron-15% chromium single crystal where epitaxial growth of γ-M_2O_3 indicates a strong stabilising influence from the metal-oxide interface. The degree of stabilisation is dependent upon atom arrangements at the interface, being favoured by a high atomic population and close matching of the atom spacings in the interfacial plane. For example, on many grains of iron-20% chromium alloy electropolished prior to oxidation, α-M_2O_3 formed from the commencement of oxidation suggesting that the substrate orientation did not stabilise γ-M_2O_3, while on other grains γ-M_2O_3 was produced. Etching the polycrystalline metal tended to expose more low index crystal planes of (100) type and, consequently, a higher proportion of γ-M_2O_3 was found on etched iron-20% chromium alloy.

The total free energy of formation of an oxide phase on a metal, ΔG, may be expressed as the sum of the volume free energy, ΔG_V, the interfacial free energy, ΔG_I, and the strain energy, ΔG_S : $\Delta G = \Delta G_V + \Delta G_I + \Delta G_S$ —①. As the oxide film thickens, ΔG_V and ΔG_S will increase in magnitude while ΔG_I will remain substantially constant.

Hence the influence of ΔG_I will be significant in the early stages of oxidation but will progressively decrease as the reaction proceeds. Its importance during initial oxidation of metal to α-M_2O_3 or γ-M_2O_3 may be estimated by rewriting equation 1 as $\Delta G^1 = \Delta G_V{}^1 + \Delta G_I{}^1 + \Delta G_S{}^1$, where the terms now represent the difference between the free energies of formation of γ-M_2O_3 on metal and of α-M_2O_3 on metal. It will be assumed that $\Delta G_S{}^1$ is small compared with other terms when the oxide is thin. $\Delta G_V{}^1$ is simply the free energy change for the γ-M_2O_3 to α-M_2O_3 transformation and, since the corresponding entropy change will be small, $\Delta G_V{}^1$ will approximately equal the enthalpy change, given as 47.5 ± 2.3 cal g^{-1} ($2 \pm 0.1 \times 10^5$ J kg^{-1}) for the γ-Fe_2O_3 to α-Fe_2O_3 transformation (Lodding and Hammell, 1960). The interfacial energy for coherent growth of γ-M_2O_3 observed on metal will be much smaller than that associated with the observed incoherent growth of finely polycrystalline α-M_2O_3 and a value of $1 Jm^{-2}$ will, therefore, be assumed for the difference in interfacial energies for the metal-oxide systems. Equating $\Delta G_V{}^1$ to $\Delta G_I{}^1$ shows that the difference in interfacial energy is comparable to the difference in volume free energy for an oxide thickness of $\sim 10\text{Å}$. This estimate indicates the order of magnitude of the interfacial effect in these thin films. The strain energy in an incoherent film of α-M_2O_3 will be very much less than the strain energy in a coherent film of γ-M_2O_3 so that $\Delta G_S{}^1$ is approximately equal to ΔG_S for γ-M_2O_3. The estimated strain energy in a film

of γ-M_2O_3 10Å thick with a metal-oxide mismatch of 3% (see § 4.5.1) is approximately one tenth of ΔG_V^1 and ΔG_I^1, justifying the omission of ΔG_S^1 from the above calculation.

4.5.3 Factors affecting Subsequent Oxide Growth

While solid state diffusion processes are not important in the initial oxidation stage, as the oxide thickens they become increasingly significant in determining the subsequent course of the reaction. In iron-chromium oxides cation diffusion predominates (Holmes and Mortimer, 1973) and Azaroff (1961) has shown that, for spinels, the most probable diffusion path is via alternate, adjacent octahedral and tetrahedral interstices. The ease of migration of a cation via the Azaroff mechanism is determined principally by the octahedral site preference energies of constituent cations of the oxide; thus Cr^{3+} moves with difficulty while Fe^{3+} moves readily through the spinel lattice. A similar effect is predicted for γ-M_2O_3 since it may be regarded as a defective spinel (see § 4.5.2). For α-M_2O_3, Azaroff has shown that octahedral interstices parallel to the c-axis provide possible diffusion paths. Two-thirds of these positions will be already occupied by cations and, either the diffusing cation will have to bypass the occupied site by way of a tetrahedral interstice, or the occupying cation must be displaced to a tetrahedral position to create an octahedral vacancy. In both cases the rate of movement of the cation through α-M_2O_3 is determined by

the octahedral preference energy as in cubic close-packed oxide structures.

Such considerations have been invoked to explain segregation of transition elements which often occurs in oxide scales on alloys (§ 4.3). In the present context for α-M_2O_3, γ-M_2O_3 and M_3O_4 phases, the different mobilities of Cr^{3+}, Fe^{3+} and Fe^{2+} would result in a progressive enrichment of iron at the oxide-gas interface as the oxide film thickens. As a consequence, transitions from one oxide to another become possible during the course of oxidation. Structural evidence from the present study shows that the transitions γ-M_2O_3 to α-M_2O_3 and γ-M_2O_3 to M_3O_4 occur, indicating that in these cases γ-M_2O_3 becomes destabilised as oxidation proceeds, i.e. the stabilising influence of the interface becomes decreasingly significant. The importance of interfacial effects has also been demonstrated experimentally in the solid state oxidation of Fe_3O_4 to γ-Fe_2O_3. It was shown (Egger and Feitknecht, 1962) that the reaction may proceed by one of two possible paths, the choice being determined by the particle size of the material. Small particles ($< 3000\text{Å}$) oxidised firstly to γ-Fe_2O_3 followed by a transition to α-Fe_2O_3, while larger particles ($> 5500\text{Å}$) oxidised directly to α-Fe_2O_3. Hence a high surface area to volume ratio promoted the formation of γ-Fe_2O_3.

4.5.4 Oxide Growth Sequences

The principles outlined in this paper can

account for the oxide growths observed in the present work, including the complex oxidation products formed on the electropolished iron-20% chromium alloy. The oxide layers found on individual grains on this alloy can be explained by one of three proposed growth sequences, (a) formation of α-M_2O_3, (b) initial formation of γ-M_2O_3 which undergoes a transition to M_3O_4 and (c) initial formation of γ-M_2O_3 which undergoes a transition to α-M_2O_3:

(a) The formation of a single oxide phase consisting of finely polycrystalline α-M_2O_3 occurs on those grain orientations which present a high index plane to the oxidising gas. The degree of interfacial stabilisation is insufficient to support the formation of metastable γ-M_2O_3, and thermodynamically stable α-M_2O_3 is produced from the start of oxidation. Mismatch between the metal and α-M_2O_3 is evidenced by the finely polycrystalline texture of the oxide phase. This type of film is fairly protective and is also found on iron-70% chromium single crystal.

(b) Formation of metastable γ-M_2O_3 at the commencement of oxidation occurs on metal grain orientations which exert a strong stabilising influence on the oxide film. The film grows epitaxially as thin crystals on the metal and contains some stress due to mismatch at the interface. As the film thickens the stabilising influence of the interface decreases. Experimental results suggest that this occurs when the chromium-iron ratio in the outer oxide has fallen sufficiently (< 1.87) to permit formation of M_3O_4. This type

of oxide growth is much thicker than the α-M_2O_3 film formed on other grains of the same alloy, case (a), and is also found on the iron-15% chromium single crystals. The increased cation diffusion through γ-M_2O_3/M_3O_4 films is believed to be due to the higher proportion of relatively mobile Fe cations in these films compared with the chromium-rich α-M_2O_3 films (see § 4.5.3).

(c) The oxide growth sequence γ-M_2O_3 to α-M_2O_3 may be regarded as a case intermediate between (a) and (b), where the influence of substrate orientation is sufficient for γ-M_2O_3 to form initially but is less than in (b). Thus an earlier transition to a thermodynamically stable phase occurs, in this case to rhombohedral oxide as evidenced by the coexistence of large single-crystal films of α-M_2O_3 oriented epitaxially with γ-M_2O_3. γ-M_2O_3 can grow epitaxially on the metal because of the small metal atom mismatch at the oxide-metal interface and the α-M_2O_3 may then grow epitaxially on γ-M_2O_3 via the closely matching anion layers. Only a very thin layer of γ-M_2O_3 on the metal appears to be required for promoting oriented α-M_2O_3 growth and its absence causes α-M_2O_3 to grow in a finely polycrystalline form as in (a).

Thus, the choice of oxide growth sequence between case (b) and case (c) depends upon chromium concentration at the oxide-gas interface when continued formation of γ-M_2O_3 becomes energetically unfavourable (see § 4.5.2), a high chromium content in the γ-M_2O_3 phase favouring the

transition to α-M_2O_3 rather than to M_3O_4 with its limited chromium solubility.

4.6 Oxidation Kinetics in the Early Stages

It has been demonstrated in § 3.1 that the early stages of the oxidation reaction yields segmented oxidation curves (Fig. 3.3). The discontinuities are seen to occur at roughly equal weight-gain intervals for example at 1.5×10^{-2} kg m^{-2} at 600°C. The corresponding vacancy fraction injected into the metal for these weight-gain increments may be calculated, assuming that the vacancy concentration returns to its equilibrium value after each discontinuity, as

$$C_v = \frac{W}{\rho_m} \times \frac{f}{t}$$

where W = 2 x weight-gain/unit area (the factor 2 arises because two metal surfaces must be considered), ρ_m is the density of the metal, f is the ratio of the weight of iron and oxygen in the oxide film and t is the thickness of the metal. At 600°C, $W = 3 \times 10^{-2}$ kg m^{-2} and for iron-chromium alloys $\rho_m \sim 7.9 \times 10^3$ kg m^3. For a spinel-type oxide f = 2.6. Substituting these data together with a value 1 mm. for the specimen thickness gives a vacancy fraction of 9.9×10^{-3}. It should be noted that this value corresponds closely to the vacancy fraction required to induce the formation of lamellar void distributions in thicker oxide scales formed on these alloys at this temperature. ($\sim 6 \times 10^{-3}$, see § 4.4.2.)

A second important feature of the early stages of oxidation is the development of islands of spinel oxide on the thin film of protective rhombohedral oxide (Fig. 3.12). This observation together with the discontinuities in the oxidation rate curve suggest that breakdown of the thin rhombohedral oxide occurs when the free energy accompanying vacancy supersaturation is sufficient to exceed the work of adhesion of the oxide-metal interface. A void is then nucleated beneath the oxide layer and the oxide above the void becomes mechanically unstable and collapses under the external pressure of gas (Howes, 1968) to allow direct access of gaseous oxidant to the surface of the alloy. Since the surface of the alloy is now depleted in chromium as a result of the formation of chromium-rich rhombohedral oxide, spinel oxide is formed. This interpretation is consistent with the observed morphology of oxide growth which shows thin, strongly adherent oxide forming a continuous phase with isolated islands of spinel growing on some grains.

It may be proposed that the nucleation of voids beneath the rhombohedral oxide becomes more difficult in the later stages of oxidation as the number of areas of low interfacial free energy become fewer (the interfacial free energy is a function of the crystal orientation of the substrate and the surface morphology) and thus void nucleation beneath the spinel oxide islands become increasingly favoured. This change in the type of preferred site for nucleation of voids is also encouraged by the high flux of

vacancies created in these areas by the fast growing spinel oxide. Thus in the later stages very few new spinel nuclei are formed but those already present grow larger and larger until coalescence of spinel oxide patches occurs.

Consider now the growth of an isolated island of spinel, Fig. 4.3. At position 1 the reaction is limited by diffusion through the oxide film and hence would be expected to thicken parabolically according to a law of the form

$$W = k'_p \sqrt{t}$$

where W is the weight gain, k'_p is the parabolic rate constant and t is the time.

At position 2, however, the oxidation reaction proceeds rapidly since it is not limited by solid state diffusion processes, the high flux of vacancies in these regions contributing to the breakdown of the adjacent rhombohedral oxide. Hence lateral growth of the island would be expected to be linear. If the islands are assumed to be circular the radius would vary with time according to a law of the form

$$r = k_r t$$

where r is the radius and k_r is a linear rate constant. This form of lateral growth kinetics is in accord with the observations of other workers (Boggs, 1961; Beck, Heine, Caule and Pryor, 1967).

If the surface contains n islands of spinel per unit

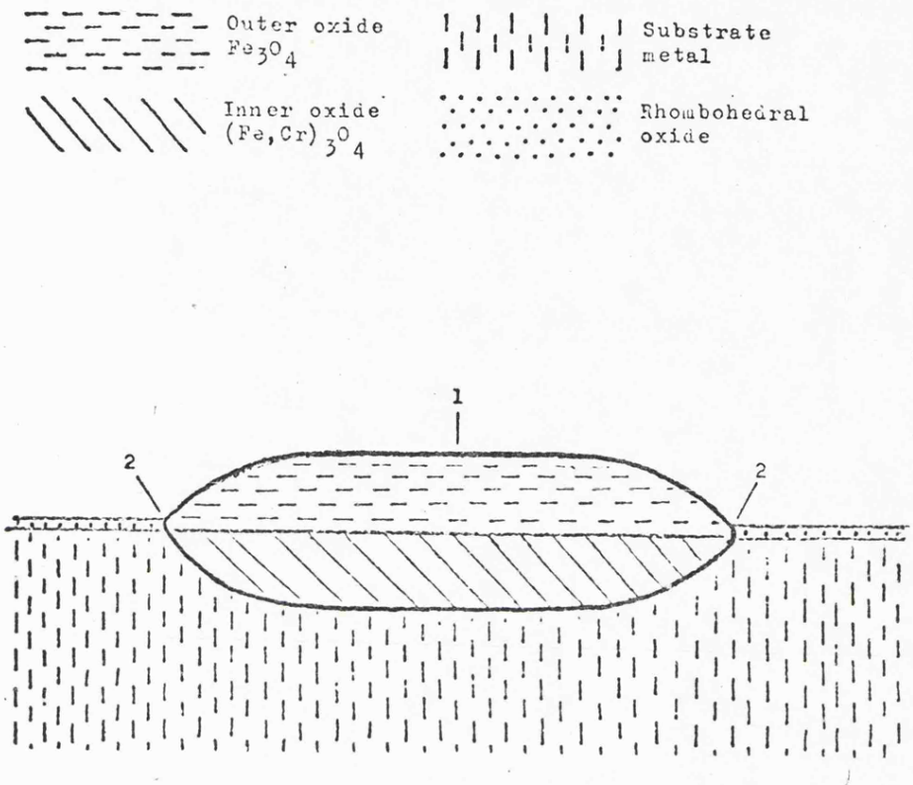

Fig.4.3 Schedmatic diagram of an island of spinel oxide.

area the fraction of the surface covered with oxide while the patches are small and do not impinge on one another is given by

$$A_s = n\pi r^2$$

$$r \rightarrow 0$$

$$= n\pi (k_r\ t)^2$$

where A_s is the fraction of the surface area covered with spinel. By statistical arguments, Evans (1960) has shown that as r increases the fraction of the total area covered is given by

$$A_s = 1 - \exp\left[-n\pi (k_r\ t)^2\right]$$

which reduces to the above equation when $t \rightarrow 0$. Hence the fraction not covered with spinel, i.e. covered with rhombohedral oxide, is given by

$$A_r = \exp\left[-n\pi (k_r\ t)^2\right]$$

Thus the total weight gain per unit area of the specimen is given by

$$W = k_p' \sqrt{t}\ \left\{1 - \exp\left[-n\pi (k_r\ t)^2\right]\right\} + f(t) \cdot \exp\left[-n\pi (k_r\ t)^2\right]$$

f(t) is the function representing the rate of growth of the thin rhombohedral film and can be ignored except at small t since it is very much smaller than $k_p\sqrt{t}$ under these conditions. The experimental weight gain curve for an iron-15% chromium alloy, Fig. 4.4, was analysed using this model and a good fit was obtained (except at short oxidation times) giving the following result

$$W = 5.5 \times 10^{-3} \sqrt{t}\ \left[1 - \exp - (5.6 \times 10^{-3}\ t^2)\right] \quad \ldots\ldots\ 4.1$$

where W = weight gain in kg m^{-2} and t is in hours.

At low values of weight gain the influence of the

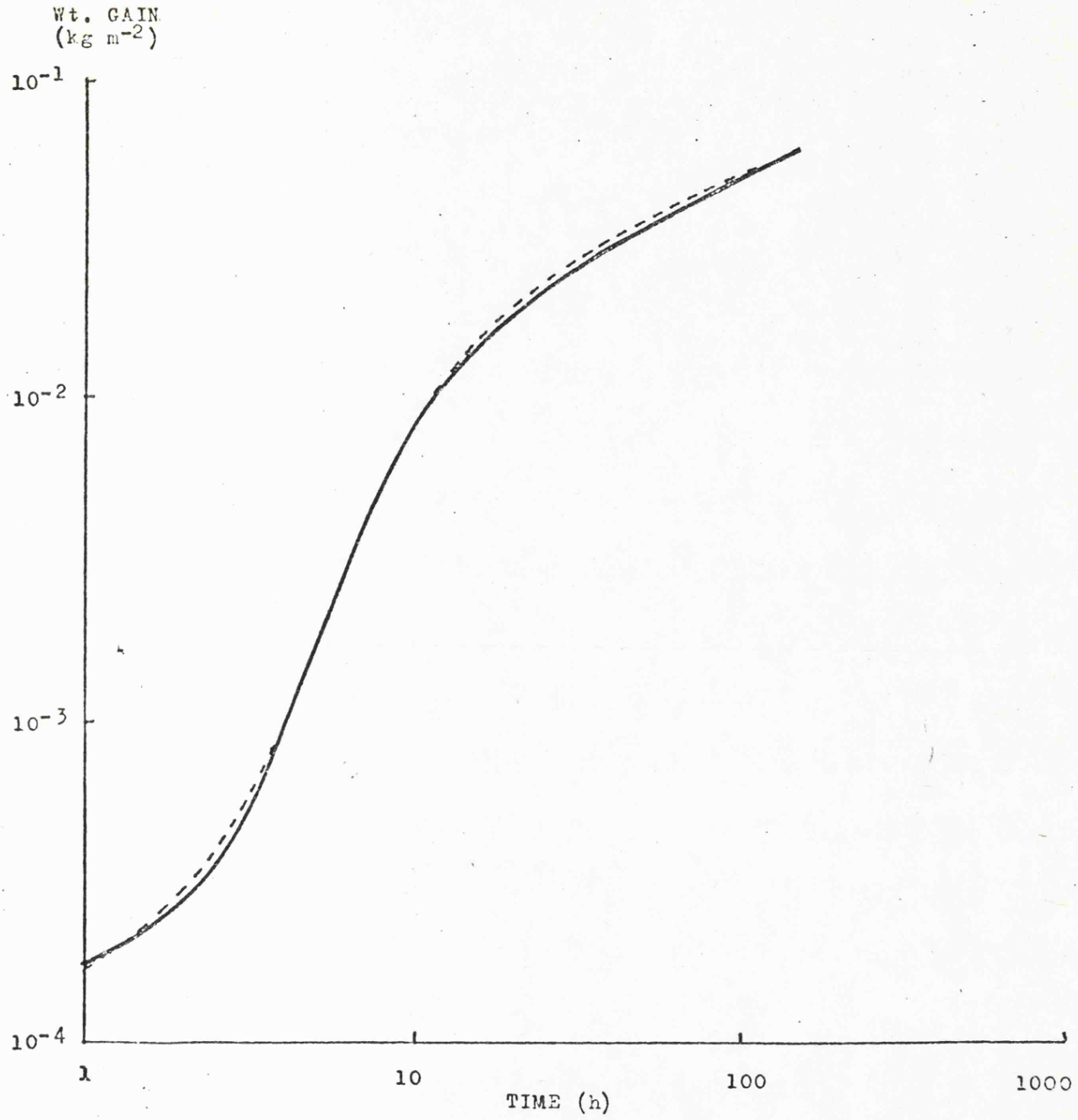

Fig.4.4 Oxidation of Fe-15% Cr alloy at 600°C in CO_2-based gas. Solid curve shows experimental data. Broken curve is derived from equation 4.1.

initial rhombohedral film is apparent and the difference between the calculated curve and the experimental curve is approximately constant in this region. This difference is $\sim 1.3 \times 10^{-4}$ kg m^{-2} corresponding to a rhombohedral oxide film of thickness $\sim$ 800A, a value consistent with the observed electron transparency of this oxide. Thus the whole oxidation curve may be expressed by the equation

$$W = 5.5 \times 10^{-3} \sqrt{t} \left[1 - \exp - (5.6 \times 10^{-3} t^2)\right] + 1.3 \times 10^{-4}$$

It should be noted that this treatment correctly predicts the slope of the steeply rising part of the oxidation curve to be 2.5 as follows:

$$W = k_p' \sqrt{t} \left[1 - \exp - n\pi (k_r t)^2\right]$$

$$W \sim k_p' \sqrt{t} \left[n\pi (k_r t)^2\right]$$

$t \longrightarrow 0$

i.e. $W \propto t^{2.5}$

It is interesting to note also that the equation predicts the coverage of the surface by spinel increases slowly at first and then rises rapidly to a value corresponding to complete coverage.

Thus the growth kinetics of the initial and transitional oxidation stages may be explained on the basis of sequential breakdown of the initial oxide film, due to vacancy condensation, in the early stages of oxidation forming spinel nuclei. The number of nuclei remains constant after this initial period but the nuclei increase in size until eventually the whole surface becomes covered with the characteristic duplex oxide scale.

CHAPTER 5

CONCLUSIONS

This chapter is a brief summary of the main conclusions drawn from the study of oxidation of Fe-Cr alloys in CO_2-based gas. The formation of duplex scales is first considered followed by the treatment of initial oxidation.

The formation of a duplex oxide scale on the alloys has been explained on the basis of a rate-controlling outward movement of cation through the scale via a solid-state diffusion process together with simultaneous inward transport of oxidant to form the inner layer. A considerable weight of indirect evidence is presented which suggests that this latter process occurs via a gas-phase transport mechanism. The inward transport of oxidant to the metal-oxide interface is shown to become more difficult as the oxidation proceeds as a result of pore blocking processes occurring in the outer oxide. Thus the formation of inner oxide is slowly suppressed and eventually growth of the inner layer becomes insufficient to fill completely the space created by the outwardly moving cations. In this way the considerable voidage found in the inner scale is explained.

The observation of the regularly spaced, lamellar voids in the inner oxide is evidence that voids are formed by a cyclic process. It is then proposed that solution

of vacancies, created by outward migration of cations, occurs in the metal until a critical concentration is exceeded. Calculation of the critical vacancy fraction from the measured lamellar void spacings gives values $\sim 6 \times 10^{-3}$ at 600°C. Typical interfacial energy values are shown to be commensurate with the free energy associated with the maximum vacancy supersaturation.

The segregation of alloying elements within the duplex oxide has also been studied and explained on the basis of a cation diffusion model. An analysis of the diffusion path networks for cations in close-packed oxides suggests that in cubic oxides transport via alternate, adjacent octahedral and tetrahedral interstices is most likely while for rhombohedral oxides an alternative route via octahedral sites only is available. The relative rates of cation diffusion in these oxides is then explained by considering the potential energy variation when a cation is transferred from one site to another. It is shown that the activation energy for this process may be regarded as the sum of two terms, a strain energy term and a site preference energy term. The former term is fairly constant for transition metal cations while the latter term may be calculated using crystal field theory. The predictions of the analysis accord well with the present work as well as previous data published by other workers.

The initial oxidation has also been investigated and it has been shown that the composition and character of the

metal surface are important in determining the type of oxide formed on particular metal grains. New information on the nature of metal-oxide orientation relationship is presented which suggests that metastable γ-M_2O_3 may be the first oxide to form and as a result of the decreasing influence of the oxide-metal interface this oxide subsequently transforms to either rhombohedral oxide, α-M_2O_3 or to cubic spinel, M_3O_4, as the oxide film thickness. Using crystal field theory it is shown that the structure of the transformation product depends on the $^{Fe}/_{Cr}$ ratio of the oxide film at the time of transformation. From an analysis of the kinetics of the initial oxidation it is also suggested that the breakdown of the thin, protective, rhombohedral films formed in the initial stages is associated with vacancy condensation at the metal-oxide interface leading to spinel nucleation. On this basis discontinuities observed in the kinetics of oxidation are accounted for. The subsequent oxidation kinetics are explained by simultaneous lateral and vertical growth of spinel nuclei. The onset of parabolic kinetics is associated with coalescence of the spinel covered areas to form the characteristic duplex scale.

REFERENCES

ADAM, A.M., SILVA, M.A., and SPIERS, V.M., 1960, Nature, 186, 147.

ANDERSEN, C.A., 1967, Brit. J. Appl. Phys., 18, 1033.

ANDREWS, K.W., KEOWN, D.J., and DYSON, S.R., 1971, Electron Diffraction Patterns, Hilger, London.

APPLEBY, W.K., and TYLECOTE, R.G., 1970, Corros. Sci., 10, 325.

ASKILL, J., 1971, Tracer Diffusion Studies, Plenum Press, New York.

AZAROFF, L.V., and BEURGER, M.J., 1958, The Power Method in X-ray Crystallography, McGraw Hill, New York.

AZAROFF, L.V., 1961, J. Appl. Phys., 32, 1638.

BARDOLLE, J., 1954, Rev. Métall., 51, 833.

BECK, A.F., HEINE, M.A., CAULE, E.J., and PRYOR, M.J., 1967, Corros. Sci., 7, 1.

BENARD, J., 1960, Acta Met., 8, 272.

BISHOP, H.E., 1968, Brit. J. Appl. Phys. (J. Phys. D), 1, 673.

BOGGS, W.E., 1961, J. Electrochem. Soc., 108, 124.

BOGGS, W.E., and KACHICH, R.H., 1969, J. Electrochem. Soc., 116, 424.

BOKROS, J.C., and WALLACE, W.P., 1960, Corrosion, 16, 117.

BOOKER, G.R., 1970, in Modern Diffraction and Imaging Techniques in Material Science, eds: S. Amelincx, R. Gevers, G. Ramant, and J. Van Landuyt, North Holland, Amsterdam, 553-611.

BORIE, B., SPARKS, C.J., and CATHCART, J.V., 1962, Acta. Met., 10, 691.

BRABERS, M.J., and BIRCHENALL, C.E., 1958, Corrosion, 14, 179t.

BRENNER, S.S., 1955, J. Electrochem. Soc., 102, 8.

CAPLAN, D., and COHEN, M., 1952, Trans. A.I.M.E. J. of Metals, 4, 1057.

CAPLAN, D., and COHEN, M., 1959, Corrosion, 15, 141.

CAPLAN, D., GRAHAM, M.J., and COHEN, M., 1972, J. Electrochem. Soc., 119, 1205.

CASTLE, J.E., and SURMAN, P., 1969, J. Phys. Chem., 73, 632.

COOK, C.J., and DUNCUMB, P., 1969, 5th International Congress on X-ray Optics and Microanalysis, Tubingen, Spinger Verlag, 245.

COOPER, H.G., KOEHLER, J.S., and MARX, J.W., 1955, Phys. Rev., 97, 599.

CULLITY, B.D., 1956, Elements of X-ray Diffraction, Addison-Wesley, New York.

DOUGLASS, D.L., 1969, Oxidation of Metals, 1, 127.

DRAVNIEKS, A., and McDONALD, H.J., 1948, J. Electrochem. Soc., 94, 139.

DUNNINGTON, B.W., BECK, F.H., and FONTANA, M.G., 1952, Corrosion, 8, 2.

EGGER, K., and FEITKNECHT, W., 1962, Helv. Chim. Acta., 45, 2042.

EVANS, U.R., 1947, Corrosion, 4, 149.

EVANS, U.R., 1960, The Corrosion and Oxidation of Metals, Arnold, London.

FOOTNER, P.K., HOLMES, D.R., and MORTIMER, D., 1967, Nature, 216, 54.

FRANCIS, J.M., and WHITLOW, W.H., 1966, J. Iron Steel Inst., 204, 355.

FUJII, C.T., and MEUSSNER, R.A., 1960, Naval Research Laboratory, Washington, U.S.A., Report No. NRL-5506.

FUJII, C.T., and MEUSSNER, R.A., 1967, J. Electrochem. Soc., 114, 435.

GENSCH, C., and HAUFFE, K., 1951, Z. Phys. Chem., 196, 427.

GREENWOOD, N.N., and HOWE, A.T., 1972, Reactivity of Solids, Chapman and Hall, London.

GULBRANSEN, E.A., PHELPS, R.T., and HICKMAN, J.W., 1946, Ind. Eng. Chem. (Anal. Ed.), 18, 640.

GULBRANSEN, E.A. and COPAN, T.P., 1959, Disc. Faraday. Soc., 28, 229.

GULBRANSEN, E.A., and COPAN, T.P., 1960, Nature, 186, 959.

GULBRANSEN, E.A., 1965, Corrosion, 21, 76.

HALES, R., and HILL, A.C., 1972, Corros. Sci., 12, 843.

HALES, R., HILL, A.C., and WILD, R.K., 1973, Corros. Sci., 13, 325.

HALES, R., DOBSON, P.S., and SMALLMAN, R.E., 1968, Metal. Sci. J., 2, 224.

HAUFFE, K., and GENSCH, C., 1950, Z. Phys. Chem. 195, 116.

HEARLE, J.W.S., SPARROW, J.T., and CROSS, P.M., 1972, The Use of the Scanning Electron Microscope, Pergamon Press, Oxford.

HILTY, D.C., FORGENG, W.D., and FOLKMAN, R.L., 1955, Trans. A.I.M.E., 203, 253.

HIRSCH, P.B., HOWIE, A., NICHOLSON, R.B., PASHLEY, D.W., and WHELAN, M.J., 1965, Electron Microscopy of Thin Crystals, Butterworths, London.

HOAR, T.P., 1959, Modern Aspects of Electrochemistry, No.11, Ed: J.O.M. Bockris, Butterworths, London, 279.

HOLMES, D.R., and MORTIMER, D., 1973, Corrosion Conf., Bath University.

HOWES, V.R., 1967, Corros. Sci., 7, 735.

HOWES, V.R., 1968, Corros. Sci., 8, 221.

HUSSEY, R.J., MITCHELL, D.F., CAPLAN, D., and COHEN, M., 1972, J. Mat. Sci., 7, 1125.

ISHERWOOD, B.J., and QUINN, T.E.J., 1967, Brit. J. Appl. Phys., 18, 717.

JANNSON, S.A., 1964, Proc. 3rd European Conference on Electron Microscopy, Prague, p.73.

JERSON, W.B., ANTILL, J.E., and WARBURTON, J.B., 1965, British Corrosion Journal, 1, 15.

JONES, H., 1971, Metal Sci. J., 5, 15.

KAY, D., 1965, Techniques for Electron Microscopy, Blackwell, London.

KELLY, A., 1966, Strong Solids, Oxford University Press.

KIMOTO and HASHIMOTO, 1966, The Electron Microprobe, Eds: McKinley, Heinrich and Wittry, Wiley, New York, p.480.

KOFSTAD, P., 1966, High Temperature Oxidation of Metals, Wiley, New York.

KUBASCHEWSKI, O., and HOPKINS, B.E., 1962, Oxidation of Metals and Alloys, Butterworths.

LAUBENGAYER, A.W., and McCUNE, H.W., 1952, J. Amer. Chem. Soc., 74, 2362.

LAWLESS, K.R., and GWATHMEY, A.T., 1956, Acta. Met., 4, 153.

LAWLESS, K.R., 1974, Rep. Prog. Phys., 37, 231.

LODDING, W., and HAMMELL, L., 1960, Anal. Chem., 32, 657.

MALDY, J., 1965, Rev. Met. Mem. Sci., 62, 439.

MARTIN, P.M., and POOLE, D.M., 1971, Metallurgical Transactions.

MARTIUS, U.M., 1955, Canad. J. Phys., 33, 466.

McCOY, H.E., 1965, Corrosion, 21, 84.

MEADOWCROFT, D.B., and HICKS, F.G., 1972, Conference on Electrical, Magnetic, and Optical Properties of Ceramics, British Ceramic Soc., London, p.33.

MEHL, R.F., and McCANDLESS, E.I., 1937, Trans. Am. Inst. Min. metall. Engrs., 125, 531.

MOREAU, J., 1953, Comptes Rendus, 236, 85.

MOREAU, J., and BENARD, J., 1956, J. Chim. Phys., 787.

MROWEC, S., 1967, Corros. Sci., 7, 563.

PFEIL, L.B., 1929, J. Iron Steel Inst., 119, 501.

REED, S.J.B., and LONG, J.V.P., 1963, X-ray Optics and Microanalysis, Eds: H.E. Pattee, V.E. Cosslett and A. Engstrom, Vol.3, p.317. Academic Press, New York.

ROBBINS, M.G., WERTHEIM, G.K., SHERWOOD, R.C., and BUCHANAN, D.N.E., 1971, J. Phys. Chem. Solids, 32, 717.

RAHMEL, A., 1962, Z. Electrochem., 66, 363.

RICHARDSON, F.D., and JEFFES, J.H.E., 1948, J. Iron Steel Inst., 160, 261.

RICHARDSON, F.D., and JEFFES, J.H.E., 1949, J. Iron Steel Inst., 163, 397.

ROLLS, R., 1973, Reviews of High Temperature Materials, 1, 397.

SEYBOLT, A.U., 1960, J. Electrochem. Soc., 107, 147.

SHEWMON, P.G., 1963, Diffusion in Solids, McGraw-Hill, New York.

SMALLMAN, R.E., 1970, Modern Physical Metallurgy, Butterworths.

SMIDT and SPRAGE, 1973, Scripta Met., 7, 495.

STODDART, C.T.H., and HONDROS, E.D., 1972, Nature, 237, 90.

STRINGER, J., 1970, Corros. Sci., 10, 513.

STRINGER, J., 1972, Werkstoffe und Korrosion, 9, 747.

SURMAN, P.L., and CASTLE, J.E., 1969, Corros. Sci., 9, 771.

SURMAN, P.L., 1973, Private Communication.

TIEN, J.K., and RAND, F.S., 1972, Scripta Metall., 6, 55.

TIEN, J.K., and PETTIT, F.S., 1972, Metallurgical Transactions, 3, 1587.

TILLEY, J.D., and STONE, F.S., 1972, in 7th International Symposium on the Reactivity of Solids, Eds: Anderson, Roberts and Stone, Bristol.

TRETJAKOW, Von J.D., and SCHMALZRIED, H., 1965, Berichte der Bunsen-Gesellschaft fur Physikalische Chemie, 69, 396.

TURPIN, M.L., and ELLIOT, J.F., 1966, J. Iron Steel Inst., 204, 217.

VERNON, W.H.J., WORMWELL, F., and NURSE, T.J., 1944, J. Iron Steel Inst., 150, 81.

WAGNER, C., 1933, Z. Phys. Chem., 21, 25.

WAGNER, C., 1936, Z. Phys. Chem., 32, 447.

WAGNER, C., and GRUNWALD, K., 1938, Z. Phys. Chem., 40, 455.

WELLS, A.F., 1962, Structural Inorganic Chemistry, Oxford University Press.

WHITLOW, W.H., 1973, Ph.D. Thesis, University of Bath.

WOOD, G.C., 1962, Corrosion Sci., 2, 173.

WOOD, G.C., 1971, Oxidation of Metals and Alloys, A.S.M., p.201.

WOOD, G.C., and WHITTLE, D.P., 1964, Corros. Sci., 4.

WOOD, G.C., and WHITTLE, D.P., 1967, Corros. Sci., 7, 763.

WOOD, G.C., RICHARDSON, J.A., HOBBY, M.G., and BOUSTEAD, J., 1969, Corros. Sci., 9, 659.

WRETBLAD, Von P.E., 1930, Zeitschrift fur Anorganische und Allegemeine Chemie, 189, 320.

YEARIAN, H.J., KORTRIGHT, J.M., and LANGENHEIM, R.H., 1954, J. Chem. Phys., 22, 1196.

YEARIAN, H.J., RANDELL, E.C., and LONGO, T.A., 1956, Corrosion, 12, 515t.

YEARIAN, H.J., DERBYSHIRE, W.D., and RADAVICH, J.F., 1957, Corrosion, 13, 597t.

YEARIAN, H.J., BOREN, H.E., and WARR, R.E., 1965, Corrosion, 12, 561t.

YOUNG, F.W., CATHCART, J.V., and GWATHMEY, A.L., 1956, Acta. Met. 4, 145.

ZIEBOLD, T.O., and OGILVIE, R.E., 1964, Anal. Chem., 36, 322.

APPENDIX I

4. THE REDUCTION OF NOISE IN MICROBALANCES DUE TO THERMAL CONVECTION

M. G. C. Cox, B. McEnaney and V. D. Scott
School of Materials Science, Bath University, Bath, England

ABSTRACT

The sensitivity of microbalances used to study solid–gas reactions at high temperatures and at pressures greater than about 200 Torr is often limited by high noise levels due to thermal convection in the hot zone. Since such noise levels are associated with density gradients in the gas, they are made worse by the use of dense gases, high pressures and steep temperature gradients in the hot zone. These effects are illustrated by reference to a gravimetric study, using a Sartorius microbalance, of the oxidation of Fe–Cr alloys at 400–600°C in carbon dioxide based gas at atmospheric pressure. In this chapter, upward flow of gas at a rate of ~ 8 cm min^{-1} over samples suspended in a cylindrical silica hang-down tube resulted in unacceptable noise levels of ~ 150 μg. A simple theoretical analysis of convection in a closed cylindrical tube is presented which accounts both for this behaviour and for related noise effects reported by other workers which are due to a number of other variables. In agreement with the analysis it was shown that injection of helium into the furnace tube above the specimen significantly reduced the noise level. As an alternative approach based on the analysis, several designs of baffle within the furnace tube are considered. These considerations lead to a choice of baffle which is shown to reduce noise levels to ~ 0.5 μg. It is also shown that non-turbulent convection currents in the tare tube may cause a zero drift with changes in ambient temperature. This effect is minimized by ensuring thermal equilibrium between the tare tube and the balance case.

INTRODUCTION

The sensitivity of microbalances used to study solid–gas reactions at high temperatures and at pressures greater than about 200 Torr is often limited by high noise levels associated with thermal convection in the hot zone. This effect has been encountered in work in this laboratory on oxidation of Fe–Cr alloys in carbon dioxide based gas at atmospheric pressure and 400–600°C. This chapter comprises a microgravimetric study of the kinetics of oxidation using a Sartorius microbalance, Model 4104, and structural examination of the oxidation products using a variety of optical and electron-optical techniques.

A preliminary part of the microgravimetric work using a plain, silica furnace tube assembly (Fig. 1) showed that the balance was essentially noise-free at room temperature but that the noise level increased rapidly with temperature reaching an unacceptably high level (~ 150 μg) in the operating temperature range (400–600°C). Variations in flowrate of the gas had little effect on the noise level over the range

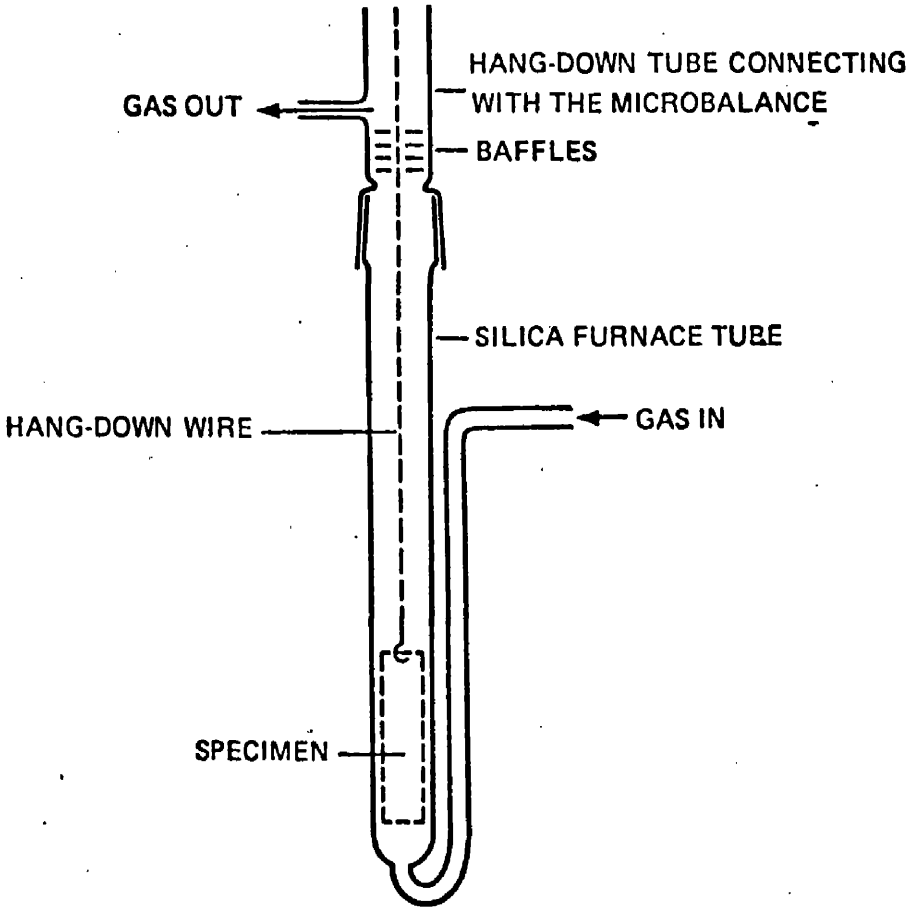

Fig. 1. Preliminary design of furnace tube.

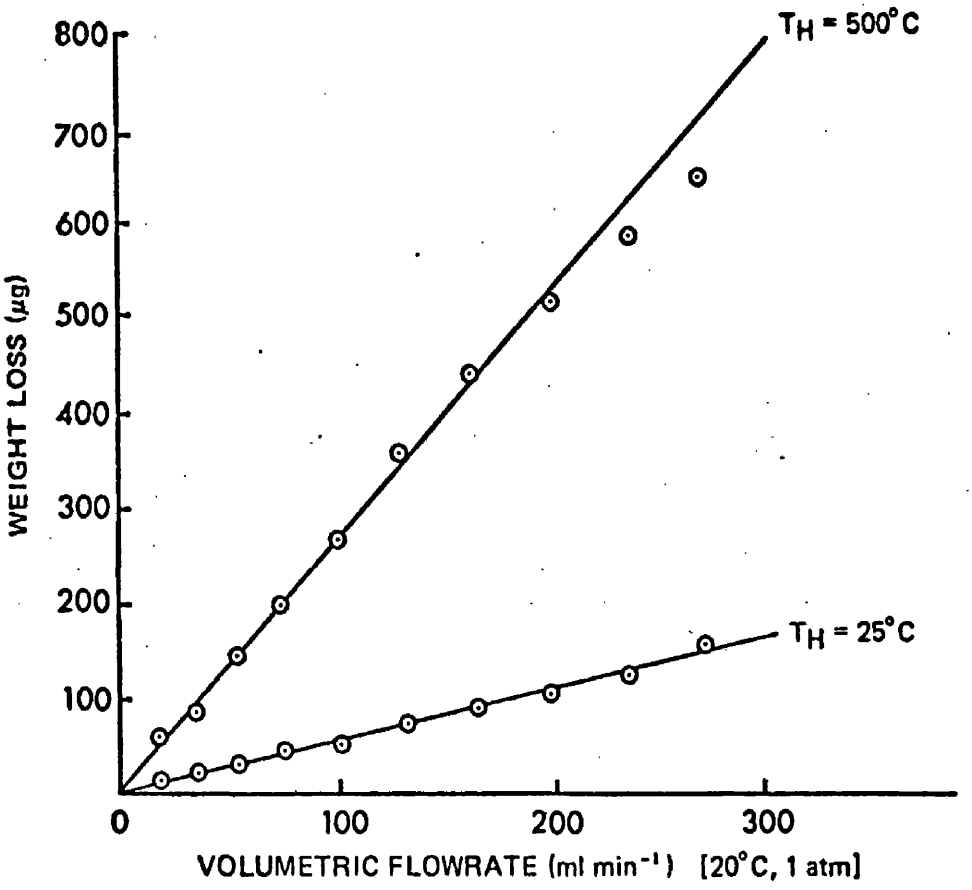

Fig. 2. The effect of volumetric flowrate of CO_2 – 1% CO gas at atmospheric pressure on the apparent weight of a silica coupon (50 x 10 x 1 mm^3).

0–250 ml (STP) min^{-1} but caused a marked change in the zero position, the specimen becoming apparently lighter with increasing flowrate (Fig. 2); this effect has been noted previously.[1] Removal of the metal specimen from the furnace while leaving the hang-down wire in position resulted in a decrease in noise level to a very low value (~ 0.5 μg). It was thus apparent that the noise was caused by momentum transfer from turbulent gas to the specimen.

Convection currents in a column of gas subjected to a temperature gradient result from density differences between gas in the hot and cold zones, such movements being opposed by frictional forces in the gas. In principle, it is possible to analyse the movement of gas by the use of the equations developed in the study of convective heat transfer. However, this approach would also require the determination of the momentum transfer from the gas to the suspended specimen in order to determine the resultant noise in microbalances and the rigorous solution of the problem is likely to be complex. An attempt at a solution of this problem has been made by Schürman *et al.*[2] for non-turbulent convection currents in a microbalance case. Equations were derived for the forces acting on the balance due to shear effects and kinetic effects of gas flow. Fair agreement was obtained between predicted and experimental dependence of these terms on the heat input to the balance case, but the equations did not predict the experimental variation with pressure of the forces acting upon the balance. In this chapter, an approach to the problem of turbulent convection in furnace tubes is developed, which at best can be regarded as semi-quantitative. However, it illuminates the contribution that various parameters make to noise level in microbalances due to convection and can be used to interpret the results of a number of workers in this field.

THEORETICAL CONSIDERATIONS

Consider a gas contained in a vertical, cylindrical tube of radius r, and subjected to a temperature gradient between an upper cold zone at temperature T_c and a lower hot zone at temperature T_h. The driving force for convection is simply the unstable density gradient between the hot and cold zones. The pressure difference γ between the two zones is given by

$$\gamma = gL(\rho_c - \rho_h) \tag{1}$$

where g is the acceleration due to gravity, L is the distance between the hot and cold zones and ρ_h and ρ_c are the density in the hot and cold zones respectively. If the flow in the tube is streamline then this driving force is opposed by friction in the gas, i.e. the viscous resistance of the tube λ. For unidirectional streamline flow in a cylindrical tube of radius r and length L the viscous resistance is given by the Poiseuille equation

$$\lambda = 8\eta L/r^2 \tag{2}$$

where η is the viscosity of the fluid. The effect of multidirectional streamline flow imposed by the geometry of the furnace tube (Fig. 1) is to modify the value of the constant by a small amount. In general the linear flowrate σ will be given by an equation

of the form $\sigma = \gamma/\lambda$ which for a plain cylindrical tube becomes

$$\sigma = \frac{gr^2(\rho_c - \rho_h)}{8\eta} \tag{3}$$

The dynamics of such a system are determined by the Reynolds number N_R which is given by

$$N_R = 2\rho\sigma r/\eta \tag{4}$$

For values of N_R below a critical value, usually of the order of 10^3, flow will be streamline while values of N_R in excess of the critical value result in turbulent flow.

Putting $\rho = \rho_m$ the mean density of the gas, and substituting for σ in Eqn. (4) gives

$$N_R = \frac{gr^3\rho_m(\rho_c - \rho_h)}{4\eta^2} \tag{5}$$

For an ideal gas, $\rho = PM/RT$ where P is the pressure of gas of molecular weight M at the temperature T and R is the gas constant, hence

$$N_R = \frac{gr^3}{4}\left(\frac{PM}{R\eta}\right)^2 [1/T_m(1/T_c - 1/T_h)] \tag{6}$$

A value of the minimum pressure for onset of turbulence may be obtained for Eqn. (6) by putting a critical value of N_R (e.g. $N_R = 10^3$) and the following values of the other parameters appropriate to the present study: $g = 0.981$ m s^{-2}; $r = 10$ mm; $M = 44$ g mol^{-1} for carbon dioxide; $R = 8.4$ J K^{-1} mol^{-1}; $\eta = 1.9 \times 10^{-5}$ N m^{-2} s for carbon dioxide at 500 K; and $T_c = 300$ K and $T_h = 700$ K. This yields a value of $P = 37$ kN m^{-2} ≙ 280 Torr.

The critical value of N_R in furnace tubes used with microbalances will not be identical to that for a plain cylindrical tube but it is reasonable to suppose that it is of the same order of magnitude. In support of this view the onset of noise in microbalances is generally observed at a pressure of the order of 100–400 Torr, in broad agreement with the value calculated from Eqn. (6).

As previously mentioned the calculation *a priori* of the noise level produced in a microbalance from convective, turbulent gas flow over a suspended specimen is likely to prove a formidable task, and consequently, the following semi-empirical correlation is presented. If the Reynolds number of the system is not much above the critical value, then the intensity of turbulence and hence the noise level χ will be some function of N_R. Robens[3] has shown that for various gases noise levels in microbalances are a linear function of pressure. Comparing this result with Eqn. (6) where $N_R \propto P^2$ suggests that for turbulent flow the relation between χ and N_R is of the form $\chi = k(N_R)^{1/2}$ or,

$$\chi = \frac{kg^{1/2}r^{3/2}}{2}\left(\frac{P}{R}\right)\left(\frac{M}{\eta}\right)[1/T_m(1/T_c - 1/T_h)]^{1/2} \tag{7}$$

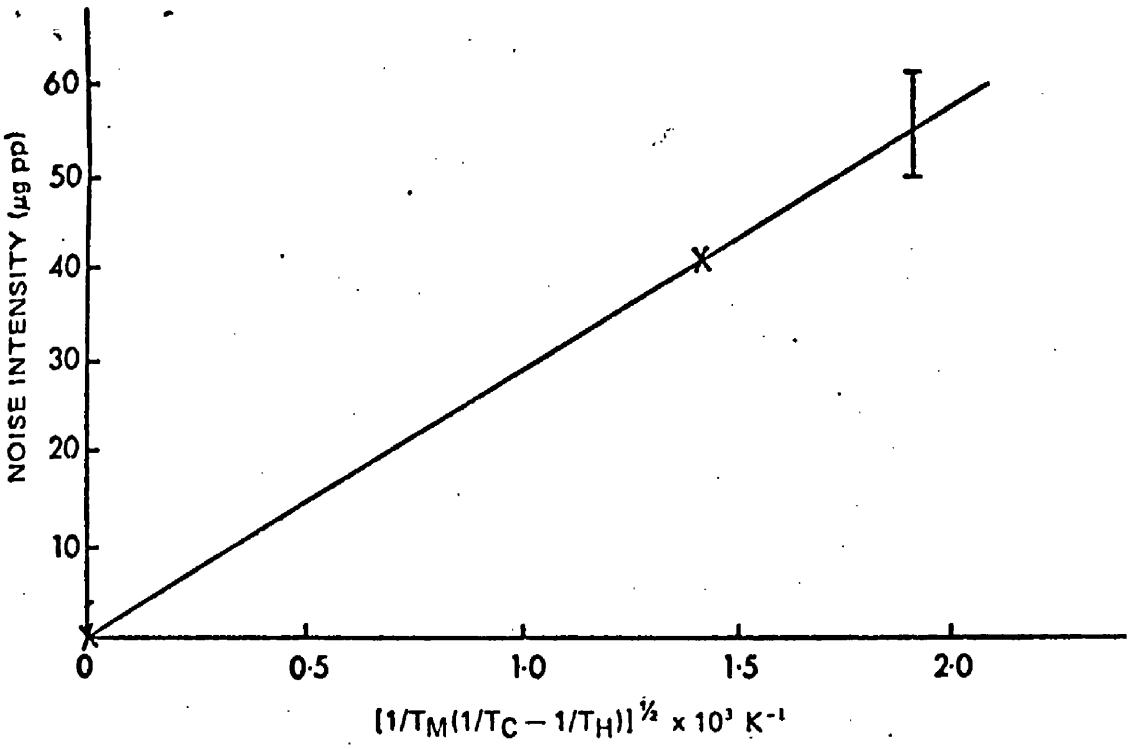

Fig. 3. The effect of temperature on noise intensity plotted according to Eqn. (7). Data from ref. 4.

This equation may be tested by comparing the predicted temperature dependence of noise level with that observed by Cahn and Schulz.[4] Figure 3 is a plot of noise intensity versus $[1/T_m(1/T_c - 1/T_h)]^{1/2}$ from the data of Cahn and Schulz and the approximate straight line obtained lends some support to the validity of Eqn. (7).

Equation (7) also illustrates the relative importance of various parameters on the production of noise in microbalances due to thermal convection. (i) The effects of variation of P and T on χ have been discussed. (ii) Equation (7) predicts that $\chi \propto r^{3/2}$ and although this relationship has not been tested, it is known that noise levels due to convection increase sensitively with increase in the radius of the hang-down tube. (iii) Equation (7) also predicts a direct relationship between χ and M/η, a molecular parameter of the gas. Values of this function for various gases are given in Table 1. It can be seen that, for example, hydrogen and helium would be expected to have relatively little effect on noise levels compared with argon and carbon dioxide, in agreement with observations made by us and other workers. It should be noted that although from kinetic theory $\eta \propto T^{1/2}$, the effect on χ of the variation of η with T over the range 300–800 K may be neglected compared with the effect on χ of the function $[1/T_m(1/T_c - 1/T_h)]^{1/2}$.

PRACTICAL CONSIDERATIONS

Since noise due to thermal convection arises from an unstable density gradient, reduction of such noise requires stabilization of the column of gas. Two methods were considered: introduction of light inert gas at the top of the tube, and incorporation of an effective baffle to prevent turbulent movement of gas.

If downward diffusion of a light gas against an upward flow of a dense gas results in inversion of the density gradient then a stable system will result. Accordingly, a

Table 1. Values of the function M/η for various gases.

Gas	M (g mol^{-1})	η at 0°C (10^{-6} N m^{-2} s)	M/η (10^{-6} g mol^{-1} N^{-1} s^{-1} m^2)
H_2	2.02	8.4	0.24
He	4.00	18.8	0.21
CH_4	16.00	10.3	1.55
NH_3	17.00	9.15	1.86
Ne	20.2	29.9	0.68
N_2	28.00	16.6	1.69
O_2	32.00	19.2	1.67
Ar	39.9	21.0	1.90
CO_2	44.00	13.8	3.19

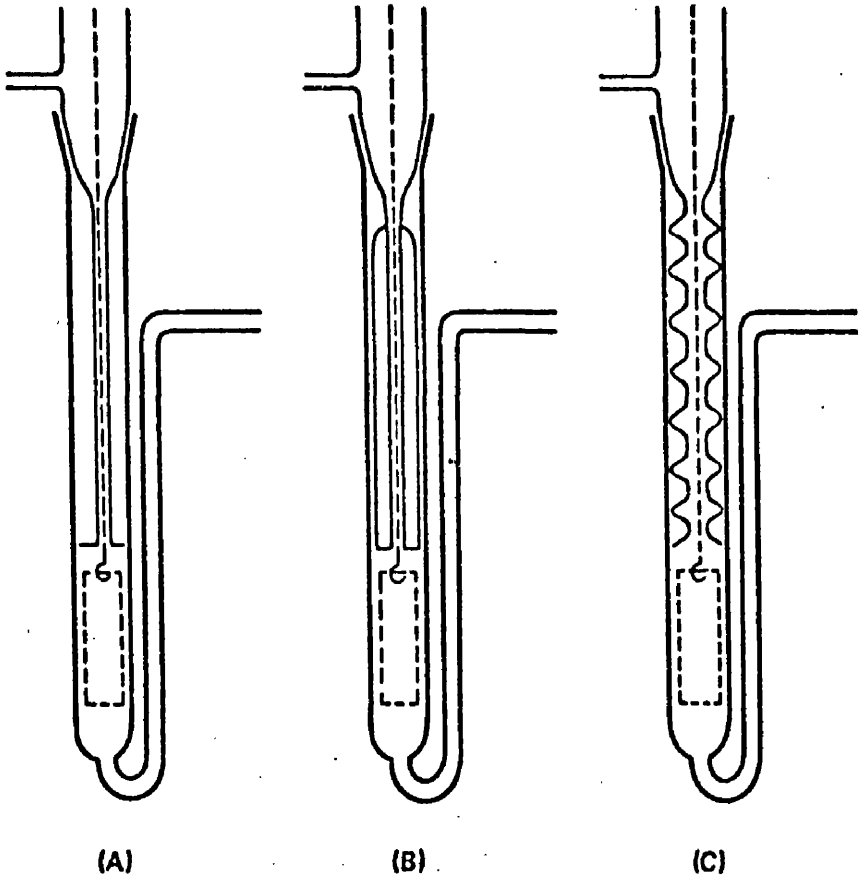

Fig. 4. Modifications to the furnace tube to reduce thermal convection.

stream of helium gas was introduced into the balance case in counter current to the upward flow of carbon dioxide; this modification reduced the noise level to less than 1 μg. Although this method was effective, it was unsuitable in the present work since the partial pressures of reactant and product gases in the hot zone were unknown.

As an alternative three designs of baffle were considered (Fig. 4). In the first [Fig. 4(a)] a close-fitting, single baffle plate was placed immediately above the specimen to minimize convective mixing of hot and cold gas. The tube around the hang-down wire was narrow in order to reduce convection in this area and to increase the upward velocity of hot gas, thus minimizing back-diffusion of cold gas. The disadvantages of this design are (i) the baffle must be accurately constructed and carefully

located to be effective and to prevent mechanical fouling of the suspension; (ii) convection currents above and below the baffle plate arising from conductive and radiative heat-transfer across the baffle plate are a possibility. The second design [Fig. 4(b)] incorporating a vacuum-jacketed hang-down tube overcomes the latter limitation but difficulties of manufacture and location are increased.

It was apparent that the only relevant parameter of Eqn. (7) which could be easily varied was $(1/T_c - 1/T_h)$ which could be reduced by reducing the effective separation between the hot and cold zones. (The radius of the tube in the hot zone, 10 mm minimum, was fixed by the size of the steel specimens). The third design [Fig. 4(c)] which was adopted exploited this principle and consisted of a series of close-fitting, convoluted baffles which effectively separated the gas into a series of small compartments, the small temperature difference between the top and bottom of a compartment reducing $(1/T_c - 1/T_h)$ to a low value. The noise level with this arrangement was less than 0.5 μg for a specimen of steel at 600 ($\pm$ 3)°C in flowing carbon dioxide at atmospheric pressure, the balance case being at 25°C.

After incorporation of the baffle, it was noted that small changes in ambient temperature produced large changes in the apparent weight of the specimen. This effect was attributed to non-turbulent gas movements between the tare tube and the balance head, of the sort considered by Schürman *et al.*[2] The effect was eliminated by installation of a vacuum-jacketed tare tube which ensured thermal equilibrium between the tube and the balance head.

ACKNOWLEDGEMENT

The authors thank C.E.G.B. for supporting this work and for permission to publish this paper.

REFERENCES

1 B. McEnaney and S. M. Rowan, *Chem. Ind.* 2032 (1965).

2 J. W. Schürman, C. H. Massen and J. A. Poulis in *Progress in Vacuum Microbalance Techniques*, Vol. 1 (Ed. Th. Gast and E. Robens), Heyden & Son, London, 1972, p. 181.

3 E. Robens in *Vacuum Microbalance Techniques*, Vol. 8 (Ed. A. W. Czanderna), Plenum Press, New York, 1971, p. 73.

4 L. Cahn and H. Schultz, *Anal. Chem.* 35, 1729 (1963).